Evidence for Relaxation of ^{129}Xe By Paramagnetic Impurities on RbH Surfaces

Scott Thomas Rohrbaugh
Reston, VA

B.Sc., University of Virginia, 2000
M.A., University of Virginia, 2006

A Dissertation presented to the Graduate Faculty of the
University of Virginia in Candidacy for the Degree of
Doctor of Philosophy

Department of Physics

University of Virginia
January, 2008

Abstract

Data are presented on the wall-induced spin-relaxaton rates of ^{129}Xe in glass cells in which the interior walls are coated with rubidium hydride (RbH). The relaxation rates have been measured as a function of both magnetic field and temperature. The relaxation rates have been measured at fields ranging from 0.01 - 1.00 Tesla, and are found to decrease significantly with increasing magnetic field. These magnetic decoupling curves are qualitatively similar for cells coated with both rubidium hydride as well as rubidium deuteride. The characteristic widths of the decoupling curves show only mild variation with temperature over the range of 223 K - 323 K. The observed behavior of the relaxation is consistent with that expected due to paramagnetic sites, although the correlation times of the interactions are surprisingly long, on the order of 10-30 picoseconds.

Acknowledgements

First off, I'd like to thank my advisor, Gordon Cates, for the guidance, inspiration, music, and all the talks about everything ranging from "Why I Should Join A Rock Band When I'm Done With Grad School" to "Why Space Stations Are Really Cool" (this dissertation fits in somewhere in the middle). Thanks for backing me all the way through. I'm proud to be your first UVA student. Secondly, thanks to Jaideep Singh for explaining physics to me, for challenging me, and distracting me so often. Also thanks for the t-shirts. Invaluable to the development of the hardware and samples for this project were the formidable technical talents of James Wang and Al Tobias. Thanks also to the rest of Cates Group (Ryan Snyder, Vladimir Nelyubin, Karen Mooney, and Peter Dolph) for contributions of advice both technical and personal, baked goods, and for taking care of the fish when I've been gone and agreeing to take the fish now that I'm leaving. You're very generous.

Thanks to Dr. Art Brill and Dr. Don Crabb for the frequent loan of equipment, elbow grease and expertise. I hope I returned everything in working order.

Personal thanks go to Joe Kraenzle, Katie Little, Katherine Monahan, Joan Cornachio, Adam Leitch, Amanda Hare, Brynn Harris, Jeanine Skorinko, Chris Galdun, Katherine van Deusen, Lil' Bursh, George Becker, John Baxton, and Micah Hart. Thanks to Jen McGuire and Mr. White. Thanks to Paul Tanner, Slade Culp, Nadia Fomin, and Josh Pierce. You're all pretty spectacular friends. Also, thanks to the UVA Psychology Department for all the parties and dates.

Thanks to the Academical Village People for the music, the srat gigs, and for teaching the meaning of (amongst many others) the word “gilly.” Thanks to ¡Viva La New Mexico! I’m so glad I was on your team!

Thanks to Mom, Dad, and Nikki for feeding me, entertaining me, encouraging me, and keeping me from quitting grad school when I was so determined to do just that. Thanks to Larry, Linda, and Jeff for supporting them while they were supporting me. There’s no way I could have made it through this without you all. I love you.

Finally, thanks to anyone who I should have mentioned but forgot to. A double-secret “my bad” to anyone offended that I did mention them.

Contents

List of Figures

List of Tables

For Lil Sis.

Chapter 1

Introduction

Ever since Proctor and Yu [1] extracted a nuclear magnetic resonance (NMR) signal from xenon-129, followed by work done by Streever, Hunt and Carr [2, 3], the use of ^{129}Xe for scientific studies has been widespread and diverse. A more recent and particularly novel application of ^{129}Xe came when it was used as the source of signal in Magnetic Resonance Imaging (MRI) studies of the lungs [4].

This novel application was only possible because of the large nuclear spin polarizations that can be achieved using the technique of spin-exchange optical pumping using lasers [5, 6]. The initial MRI studies using ^{129}Xe were shortly followed by similar studies using ^{3}He [7]. Since laser polarized ^{3}He was already in use as a polarized nuclear target [8], the technology of polarizing ^{3}He was more developed than was the case for ^{129}Xe. Thus, many of the early MRI studies using laser-polarized noble gases were performed using ^{3}He [9]. Xenon has the advantage, however, that it readily dissolves into blood [10, 11] and tissues, making studies of non-void spaces (i.e. the brain [12], kidney, etc. [13, 14]) possible. Additionally, ^{129}Xe possesses a large chemical shift [15], enabling sensitive analyses of chemical environments. Polarized ^{129}Xe has also enabled sensitive studies of surface physics [16] and phase transitions [17].

MRI using laser-polarized noble gases has extended the utility of MRI as an imagine modality. NMR in medical applications is a means of identifying the internal structure of the body by locating and mapping proton concentrations. Predictably, these protons are found mostly in hydrogen atoms, constituent to the water molecules that, taken as a whole, make up 75% of the human body by weight. The polarization

of body protons, predicted by the Boltzmann thermal polarization equation [18]:

$$P_{Thermal} = \tanh\left(\frac{\mu_P B}{k_B T}\right) \tag{1.1}$$

is very low - on the order of $10^{-5}\%$ (μ_P is the proton magnetic moment, B is the ambient magnetic field in units of Teslas, K is Boltzmann's constant of $1.38 \cdot 10^{23}$ J K^{-1} and T is absolute temperature in units of Kelvin). In in-vivo proton MRI, the limitation of extremely low sample polarization is offset by the staggering numbers of spins involved - on the order of 10^{27} protons in the typical human body.

Unfortunately, volumes that possess no protons (such as the void space of the lungs) cannot be imaged using standard MRI techniques, for obvious reasons. These restrictions can be overcome by the introduction of a non-endemic contrast agent. In a development that grew largely out of both atomic physics and later work on polarized nuclear targets, ^{3}He and ^{129}Xe polarized by optical pumping techniques were shown to be valuable as an imaging agent when introduced into biological environments.

Historically, MRI using laser-polarized noble gases has focused on ^{3}He because of the logistical ease of its polarization and the high polarization levels achievable. It is inert in the biological environment, but its insolubility in blood restricts its usage to void-space measurements (chiefly the lungs). Polarized ^{129}Xe presents the same qualitative attributes as ^{3}He [19–21], with the additional potential for use in dissolved-phase measurements, stemming from its solubility in blood [11]. An additional geopolitical benefit of ^{129}Xe versus ^{3}He is its availability - the bulk of the ^{3}He

used in both nuclear and medical applications has its origin in tritium decay from Cold War era nuclear warhead manufacture, and is consequently limited. Natural deposits on earth are virtually nonexistent. Lunar regolith is suspected to contain ^{3}He at the 0.01 ppm level [22], but such deposits are currently inaccessible to humanity.

In view of the benefits of ^{129}Xe relative to ^{3}He for medical imaging, it is unfortunate that there are a pair of conditions that significantly discourage its use. The gyromagnetic ratio of ^{129}Xe is approximately 4 times smaller than ^{3}He [1] and signals induced in detection coils are correspondingly smaller. In fact, for a fixed magnetic field, the signal is smaller than that of ^{3}He by the square of the ratio of the gyromagnetic ratios, one factor due to the smaller magnetic moment ($\mu_{^{129}Xe} = 0.277\mu_N$, while $\mu_{^3He} = -2.1274\mu_N$ [23]), and one factor due to the smaller Larmor frequency ($\gamma_{^{129}Xe} = 11.78$ MHz/T, while $\gamma_{^{129}Xe} = 32.43$ MHz/T [23]). Also owing to its strong depolarization of polarized Rb vapor, ^{129}Xe polarization levels are typically much lower than ^{3}He levels. In view of the nonrenewable nature of polarized noble-gas polarization, maximizing the initial polarization is extremely important. Given the potential usefulness to be derived from increasing ^{129}Xe polarization, a foray into understanding *why* high polarization levels are difficult to achieve is useful and potentially profitable.

The equilibrium polarization P_{gas} of a quantity of noble gas undergoing spin exchange with a polarized alkali metal vapor of polarization P_A is given by:

$$P_{Gas} = P_A \frac{\Gamma_{SE}}{\Gamma_{SE} + \Gamma_{SD}}, \tag{1.2}$$

where Γ_{SE} is the spin-exchange rate and Γ_{SD} is the spin-relaxation rate due to interactions other than the spin exchange. Eq. 1.2 suggests two approaches for maximizing the polarization in the sample: increasing the spin-exchange rate Γ_{SE}, and minimizing the spin-relaxation rate Γ_{SD}. In our group, increasing factors associated with the spin exchange rate to ^{129}Xe has been a pursuit of fervent interest, and has involved the use of laser line-narrowing techniques (to be discussed in Appendix A), multiple-pass pumping, rubidium carburation [24], and hybrid Spin-Exchange Optical Pumping [25]. Minimization of the spin-relaxation rate has also been of historical interest to our group, with efforts focusing on the use of surface coatings on the inner walls of gas containers and homogenized magnetic field environments as means of reducing the rate. The reduction of the spin-relaxation rate is doubly beneficial from the standpoint of utilization of the gas - in addition to increasing gas polarization, lowering relaxation rate means that the gas can be stored and used for longer periods of time.

At this point in the history of polarized gas research the mechanisms of gas-phase relaxation are reasonably well understood [5, 26–29] and, in the case of ^{129}Xe relaxation, have far less of an impact on the overall relaxation of a polarized sample than does relaxation due to collisions with the inside surfaces of the gas container. With surface relaxation being such a dominant effect, much research has been conducted on the nature and mechanisms of that relaxation, addressing silicone-coated cells [30,31], paraffin surfaces [32], and plain pyrex and quartz glass [31]. The research documented here is an attempt to understand the mechanism of spin-relaxation of optically polar-

ized xenon-129 on rubidium-hydride surfaces. RbH surfaces are easily formed through the reaction of in situ molecular hydrogen with rubidium which is already present in sample cells as a necessary ingredient in the polarization process. An ionic crystal, surfaces of RbH are also expected to be more easily understood than the varied and amorphous structure of glass and give more easily reproducible results [31]. Hideo Mabuchi [33], in his Princeton undergraduate senior thesis, made an attempt to identify the source of the observed surface relaxation in cells coated with rubidium hydride by measuring relaxation rates of polarized xenon as a function of both temperature and Larmor frequency. In that study, Mabuchi suggested that xenon relaxation could be due to interaction with paramagnetic sites, or spin-exchange with surface hydrogen atoms. His confidence in the paramagnetic interpretation was buoyed by a notable lack of observable hydrogen NMR signal (possible, though by no means expected, if spin-exchange was taking place), and the fact that the model typically used to detail atomic adsorption predicted surface interaction times far shorter than those that would be required for any real nuclear-associated spin-relaxation (tens of picoseconds vs. tens of nanoseconds).

In an attempt to explore the nature of xenon relaxation on rubidium hydride surfaces, our group commissioned and executed an experimental program involving the creation of tailor-made samples, the construction of a suite of test hardware, and the accumulation of over 1000 individual relaxation rate measurements. The samples consisted of 2 cm or 1" diameter hollow glass spheres filled with xenon, rubidium, nitrogen and various amounts of hydrogen or deuterium. Samples were polarized

in a spin-exchange optical pumping setup designed and constructed in-house that included high-power diode laser arrays (and later spectrally-narrowed diode lasers) and a home-built forced-hot-air optical-pumping oven. The decay of this polarization was measured at magnetic fields up to roughly 1 Tesla in a custom-made, lab-designed multi-frequency superheterodyning quadrature NMR spectrometer. Relaxation rate measurements took place over a year's time, at magnetic fields from 0.0824 T up to slightly over 1 T and temperatures from 200 K up to 323 K.

The work presented here illustrates the span of several years of intensive device construction and data acquisition and analysis. The hardware and testing protocols developed here will be of use to the polarized gas group here at UVA, and it is hoped that the data will be of unambiguous value to the field of polarized gas imaging and spectroscopy.

Chapter 2

Relaxation Theory

2.0.1 The Density Matrix

Many authors (Driehuys [34], Slichter [35], Sauer [36], Abragam [37], etc.) have found it useful to invoke the density matrix in analyses of relaxation in spin-1/2 systems. As characterized by Fano [38], the density matrix "... represents a minimum set of input data which serves to calculate the mean value of any operator Q for a system prepared according to given specifications." It serves as a means of statistically characterizing a group of quantum mechanical systems that have been identically prepared, and enables the prediction of the behavior of that group in response to an external influence if the Hamiltonian is known. Fano makes the following statements: The vector representation of the spin orientation of a state is given by

$$P_i = \langle \sigma_i \rangle = Tr\{\rho\sigma_i\}, \tag{2.1}$$

where σ is Pauli spin matrix for a given dimension. In the case of a two-state system, ρ is then given by:

$$\rho = \frac{1}{2}\begin{bmatrix} 1+P_z & P_x - iP_y \\ P_x + iP_y & 1-P_z \end{bmatrix}. \tag{2.2}$$

The extension to the expectation value of the operator Q on the system is then:

$$\langle Q \rangle = Tr\{\rho Q\}, \tag{2.3}$$

such that if Q is the angular momentum operator K_z,

$$\langle K_z \rangle = Tr\{\rho K_z\}. \tag{2.4}$$

Slichter [35] approaches an understanding of the relaxation rate by calculating the probability per unit time of transitions from state k to state m in a two-state system. For simplicity's sake, he begins with state m completely depopulated, and gives the probability per unit time of a transition to be equal to $\frac{d\langle\rho\rangle}{dt}$. The motion of ρ under the influence of a Hamiltonian consisting of a large time-independent interaction $\mathcal{H}_0$ and a small time-dependent interaction $\mathcal{H}_1(t)$ is given by:

$$\frac{d\rho}{dt} = \frac{i}{\hbar}\left[\rho, \mathcal{H}_0 + \mathcal{H}_1(t)\right]. \tag{2.5}$$

It is also very useful to consider the problem using the interaction picture where we define the quantities [35, 37]:

$$\rho^\star(t) = e^{i\mathcal{H}_0 t/\hbar}\rho(t)e^{-i\mathcal{H}_0 t/\hbar} \tag{2.6}$$

and

$$\mathcal{H}_1^\star(t) = e^{i\mathcal{H}_0 t/\hbar}\mathcal{H}_1(t)e^{-i\mathcal{H}_0 t/\hbar}. \tag{2.7}$$

Incorporating eqn. 2.6 and eqn. 2.7 into eqn. 2.5 results in:

$$\frac{d\rho^\star}{dt} = \frac{i}{\hbar}\left[\rho^\star, \mathcal{H}_1^\star(t)\right]. \tag{2.8}$$

Following further arguments made by Slichter, the equation of motion for $\rho^\star(t)$ can be found by solving the integral equation:

$$\rho^\star(t) = \rho^\star(0) + \frac{i}{\hbar}\int_0^t [\rho^\star(t'), \mathcal{H}_1^\star(t')]\, dt'. \tag{2.9}$$

An approximate solution of eqn. 2.9 can be found by replacing $\rho^\star(t')$ in the integral with $\rho^\star(0)$, and following an iterative procedure resulting in the following expression which is good to second order:

$$\begin{aligned} \rho^\star(t) &= \rho^\star(0) + \frac{i}{\hbar}\int_0^{t'} \left[\rho^\star(0) + \frac{i}{\hbar}\int_0^t [\rho^\star(0), \mathcal{H}_1^\star(t'')]\, dt'', \mathcal{H}_1^\star(t')\right] dt' \\ &= \rho^\star(0) + \frac{i}{\hbar}\int_0^t [\rho^\star(0), \mathcal{H}_1^\star(t')]\, dt' + (\frac{i}{\hbar})^2 \int_0^t \int_0^{t'} [[\rho^\star(0), \mathcal{H}_1^\star(t'')], \mathcal{H}_1^\star(t')]\, dt' dt'' \end{aligned} \tag{2.10}$$

Taking the derivative of eqn. 2.10, we arrive at

$$\frac{d\rho^\star(t)}{dt} = \frac{i}{\hbar}[\rho^\star(0), \mathcal{H}_1^\star(t)] + (\frac{i}{\hbar})^2 \int_0^t [[\rho^\star(0), \mathcal{H}_1^\star(t')], \mathcal{H}_1^\star(t)]\, dt'. \tag{2.11}$$

The perturbing hamiltonian $\mathcal{H}_1^\star(t)$ is taken to be random and $\rho^\star(0)$ and $\mathcal{H}_1^\star(t)$ are assumed to be uncorrelated. Taking an ensemble average, the random Hamiltonian $\mathcal{H}_1^\star(t)$ will average to zero ($\overline{\mathcal{H}_1^\star(t)} = 0$) and the first term on the R.H.S. of eqn. 2.10 will thus be zero [37]. For the same reason, $\rho^\star(0)$ can then be replaced with $\rho^\star(t)$ [34] [37]:

$$\overline{\frac{d\rho^\star}{dt}}(t) = -\frac{1}{\hbar^2}\int_0^t \overline{[[\rho^\star(t), \mathcal{H}_1^\star(t')], \mathcal{H}_1^\star(t)]} dt'. \tag{2.12}$$

The time variation of the expectation value of an operator Q will be given by:

$$\frac{d\langle Q\rangle^{\star}}{dt} = -Tr\left\{\frac{d\overline{\rho^{\star}}}{dt}Q\right\}. \tag{2.13}$$

Invoking the property that the trace of a product of matrices is invariant under the cyclic permutation of those matrices [28],

$$\frac{d\langle Q\rangle^{\star}}{dt} = -Tr\left\{\overline{\rho^{\star}}\frac{1}{\hbar^2}\int_0^t \overline{[[Q,\mathcal{H}_1^{\star}(t')],\mathcal{H}_1^{\star}(t)]}dt'\right\}. \tag{2.14}$$

Because $\mathcal{H}_1^{\star}(t)$ is random and stationary, only the difference between t and t' is assumed to be significant. Consequently, defining $\tau = t - t'$ and substituting $t' = t = \tau$,

$$\begin{aligned}\frac{d\langle Q\rangle^{\star}}{dt} &= -Tr\left\{\overline{\rho^{\star}}\frac{1}{\hbar^2}\int_0^t \overline{[[Q,\mathcal{H}_1^{\star}(t-\tau)],\mathcal{H}_1^{\star}(t)]}d\tau\right\} \\ &= Tr\left\{\overline{\rho^{\star}}\frac{-1}{2\hbar^2}\int_{-t}^t \overline{(\ldots)}d\tau\right\} \\ &= -Tr\{\overline{\rho^{\star}}\mathcal{A}_Q\}.\end{aligned} \tag{2.15}$$

where A_Q is given by:

$$\mathcal{A}_Q = \frac{1}{2\hbar^2}\int_{-t}^t \overline{[[Q,\mathcal{H}_1^{\star}(t')],\mathcal{H}_1^{\star}(t)]}dt'. \tag{2.16}$$

The perturbing Hamiltonian can itself be broken into constituent parts, each the

product of a spatial function and an operator function [37]:

$$\mathcal{H}_1(\tau) = \sum_{p,q} A_p^{(q)} F_q(\tau), \tag{2.17}$$

where

$$A^\star(t) = \sum_p e^{i\mathcal{H}_0 t/\hbar} A^{(p,q)} e^{-i\mathcal{H}_0 t/\hbar} = \sum_p A_p^{(q)} e^{i\hbar\omega_p^{(q)} t}. \tag{2.18}$$

We note that we are able to write $A^\star(t)$ in this form because we anticipate evaluating our transition rates between spin states thar are eigenfunctions of $\mathcal{H}_0$. Inserting equations eqn. 2.17 and 2.18 into eqn. 2.35 and taking Q as K_z, we arrive at an expression for $\mathcal{A}_{K_z}$ as a function of both operator and spatial functions:

$$\mathcal{A}_{K_z} = \frac{1}{2\hbar^2} \sum_{p,q} \left[A_p^{(-q)}, [A_p^{(q)}, K_z]\right] \int_{-t}^{t} \overline{F_q(t-\tau) F_q^*(\tau) e^{i/\hbar\omega_p^{(q)}\tau}} d\tau. \tag{2.19}$$

As mentioned before eqn. 2.15, the stationary random nature of the motion leads to the the fact that only relative time is significant to its value. The effect of this stipulation leads us to recognize that the quantity $\overline{F_q(t-\tau)F_q^*(\tau)}$ inside the integral of eqn. 2.19 is very reminiscent of the autocorrelation function of the perturbation. Replacing $\overline{F_q(t-\tau)F_q^*(\tau)}$ with $G_q(\tau)$, eqn. 2.19 becomes:

$$\mathcal{A}_{K_z} = \frac{1}{2\hbar^2} \sum_{p,q} \left[A_p^{(-q)}, [A_p^{(q)}, K_z]\right] \int_{-t}^{t} G_q(\tau) e^{i/\hbar\omega_p^{(q)}\tau} d\tau. \tag{2.20}$$

Following arguments made by Bloembergen [39] and Schearer [40], $G_q(\tau)$ can be

represented as having an amplitude averaged over all angles and an exponentially-decaying time dependence. These characteristics follow the assumption by Bloembergen that the motion, though random, has a correlation time τ and that at large values of time, $G_q(\tau)$ approaches zero. Consequently,

$$G_q(\tau) = \langle F_q F_q^* \rangle_{ave} e^{-|t|/\tau}. \tag{2.21}$$

In light of the negligible contribution to the integral that will result from times much greater than τ, the integration limits in eqn. 2.20 can be extended to infinity.

The Wiener-Khintchine theorem states that the power spectrum of any well-behaved stationary process is equal to the fourier transform of its autocorrelation function. Invoking the Wiener-Khinchin Theorem, the integral in eqn. 2.20 can be seen to be the power spectrum of the spatial components of the motion (with only real parts contributing):

$$re\left(\int_{-\infty}^{\infty} G_q(\tau) e^{i/\hbar\omega_p^{(q)}\tau} d\tau\right) = J^{(q)}(\omega^{(q)}). \tag{2.22}$$

With the form of $G_q(\tau)$ given by eqn. 2.21, $J^{(q)}(\omega^{(q)})$ becomes:

$$J^{(q)}(\omega^{(q)}) = \langle F_q F_q^* \rangle_{ave} \frac{2\tau}{1 + (\omega^{(q)}\tau)^2}. \tag{2.23}$$

Combining eqn. 2.15, eqn. 2.20, eqn. 2.21 and eqn. 2.23, the rate of change of the expectation value of the longitudinal angular momentum operator can be arrived

at:

$$\frac{d\langle K_z\rangle^\star}{dt} = -Tr\left\{\overline{\rho^\star}\frac{1}{2\hbar^2}\sum_{p,q}[A_p^{(-q)},[A_p^{(q)},K_z]]\langle F_q F_q^*\rangle_{ave}\frac{2\tau}{1+(\omega^{(q)}\tau)^2}\right\}. \tag{2.24}$$

2.0.2 Dipole-Dipole Interaction in a Static Field

It is customary at this point to discuss the nature of $\mathcal{H}_1(\tau)$. The only requirements placed upon $\mathcal{H}_1(\tau)$ so far have been that it be small in comparison to $\mathcal{H}_0$, stationary and random. Its source, however, has been unspecified. Here it will be taken that the relaxation of xenon will be due to dipole-dipole interactions involving unlike spins, and as such will be characterized by the Hamiltonian [28, 41]:

$$\mathcal{H}_1 = \frac{\mu_{Ki}\cdot\mu_{Sj}}{r_{ij}^3} - \frac{3(\mu_{Ki}\cdot r_{ij})(\mu_{Sj}\cdot r_{ij})}{r_{ij}^5}, \tag{2.25}$$

where $\mu_K = \hbar\gamma_K K$ and $\mu_S = \hbar\gamma_S S$. Eqn. 2.25 is then decomposed by eqn. 2.17. The spatial functions are as follows, with $F_{-q} = F_q$ [39] [43]:

$$F_0 = \frac{(1-3\cos^2\theta_{ij})}{r_{ij}^3}, \tag{2.26}$$

$$F_1 = \frac{\sin\theta_{ij}\cos\theta_{ij}e^{i\phi_{ij}}}{r_{ij}^3}, \tag{2.27}$$

$$F_2 = \frac{\sin^2\theta_{ij}e^{2i\phi_{ij}}}{r_{ij}^3}. \tag{2.28}$$

The spectral amplitudes entering into eqn. 2.21 are calculated to be [39]:

$$\langle F_0 F_0^\star \rangle_{ave} = \frac{4}{5r_{ij}^6}, \tag{2.29}$$

$$\langle F_1 F_1^\star \rangle_{ave} = \frac{2}{15r_{ij}^6}, \tag{2.30}$$

$$\langle F_2 F_2^\star \rangle_{ave} = \frac{8}{15r_{ij}^6}. \tag{2.31}$$

Abragam [37] gives the corresponding operators $A_p^{(q)}$ and eigenfrequencies $\omega_p^{(q)}$ for this Hamiltonian:

$$A^{(0)} = \alpha \left[-\frac{2}{3} K_z S_z + \frac{1}{6}(K_+ S_- + K_- S_+) \right], \tag{2.32}$$

$$A_1^{(0)} = -\frac{2}{3}\alpha K_z S_z, \quad A_2^{(0)} = \frac{1}{6}\alpha K_+ S_-, \quad A_3^{(0)} = \frac{1}{6}\alpha K_- S_+, \tag{2.33}$$

$$\omega_1^{(0)} = 0, \quad \omega_2^{(0)} = \omega_K - \omega_S, \quad \omega_3^{(0)} = \omega_S - \omega_K, \tag{2.34}$$

$$A^{(1)} = \alpha(K_z S_+ + K_+ S_z), \tag{2.35}$$

$$A_1^{(1)} = \alpha K_z S_+, \quad A_2^{(1)} = \alpha K_+ S_z \tag{2.36}$$

$$\omega_1^{(1)} = \omega_K, \quad \omega_2^{(1)} = \omega_S \tag{2.37}$$

$$A_1^{(2)} = \frac{1}{2}\alpha K_+ S_+, \tag{2.38}$$

$$\omega_1^{(2)} = \omega_K + \omega_S. \tag{2.39}$$

$$\alpha = -\frac{3}{2}\gamma_K\gamma_S \tag{2.40}$$

With the main Hamiltonian $\mathcal{H}_0$ given by:

$$\mathcal{H}_0 = \omega_K K + \omega_S S, \tag{2.41}$$

eqn.s 2.32, 2.35 and 2.38 are transformed into the interaction picture by eqn. 2.18 to give:

$$A^{(0)\star} = \alpha\left[-\frac{2}{3}K_zS_z + \frac{1}{6}(K_+S_-e^{i(\omega_K-\omega_S)t} + K_-S_+e^{i(\omega_S-\omega_K)t})\right], \tag{2.42}$$

$$A^{(1)\star} = \alpha(K_zS_+e^{i(\omega_S)t} + K_+S_ze^{i(\omega_K)t}), \tag{2.43}$$

$$A^{(2)\star} = \frac{1}{2}\alpha K_+S_+e^{i(\omega_K+\omega_S)t}, \tag{2.44}$$

with $\omega_K = 2\pi\gamma_K B = 2\pi\gamma_{Xe}B$ and $\omega_S = 2\pi\gamma_S B$.

Incorporating eqn. 2.22 and eqn.s 2.42, 2.43 and 2.44 in eqn. 2.19, we arrive at:

$$\begin{aligned} 2\mathcal{A}_{K_z} &= \frac{\alpha^2}{36}J^{(0)}(\omega_K-\omega_S)[K_-S_+,[K_+S_-,K_z]] + h.c. \\ &+ \alpha^2 J^{(1)}(\omega_K)[K_-S_z,[K_+S_z,K_z]] + h.c. \\ &+ \frac{\alpha^2}{4}J^{(2)}(\omega_K+\omega_S)[K_-S_-,[K_+S_+,K_z]] + h.c., \end{aligned} \tag{2.45}$$

where *h.c.* stands for hermitian conjugate. We then make use of the following relation

for spin-1/2 particles [42]:

$$\langle K_x\rangle^2 = \langle K_y\rangle^2 = \langle K_z\rangle^2 = \frac{K(K+1)}{3}, \tag{2.46}$$

and compute the commutators in eqn. 2.45 following Abragam [37]. The relaxation of species K in eqn. 2.45 becomes:

$$\begin{aligned}\frac{d\langle K_z\rangle}{dt} &= tr\{\rho\mathcal{A}_{K_z}\} \qquad (2.47)\\ &= \gamma_K^2\gamma_S^2\hbar^2\left[\langle K_z\rangle S(S+1)\left\{\frac{1}{12}J^{(0)}(\omega_K-\omega_S)+\frac{3}{2}J^{(1)}(\omega_K)+\frac{3}{4}J^{(2)}(\omega_K+\omega_S)\right\}+\right.\\ &+ \left.\langle S_z\rangle K(K+1)\left\{-\frac{1}{12}J^{(0)}(\omega_K-\omega_S)+\frac{3}{4}J^{(2)}(\omega_K+\omega_S)\right\}\right].\end{aligned}$$

In the case of xenon interaction with paramagnetic surface sites, $\langle S_z\rangle$ is assumed to be sufficiently close to the equilibrium polarization that the second half of eqn. 2.47 can be neglected. In addition, the equilibrium xenon polarization $\langle K_{z0}\rangle$ is considered to be sufficiently close to zero for the experimental conditions here as to be neglected. (A more rigorous approach would replace $\langle K_z\rangle$ on the R.H.S. of eqn. 2.47 with $\langle K_z\rangle - \langle K_{z0}\rangle$ [43].) Incorporating eqn. 2.23 and the amplitudes calculated in eqn.s 2.29 - 2.31 into the first three terms of eqn. 2.47, we find:

$$\begin{aligned}\frac{d\langle K_z\rangle}{dt} &= \frac{\gamma_K^2\gamma_S^2\hbar^2 S(S+1)}{r^6}\times \qquad (2.48)\\ &\times \left[\frac{4}{5}\frac{1}{12}\frac{2\tau}{1+(\omega_K-\omega_S)^2\tau^2}+\frac{2}{15}\frac{3}{2}\frac{2\tau}{1+(\omega_K)^2\tau^2}+\frac{8}{15}\frac{3}{4}\frac{2\tau}{1+(\omega_K+\omega_S)^2\tau^2}\right].\langle K_z\rangle\end{aligned}$$

Inspecting eqn. 2.48, it can be seen that the decay rate of $\langle K_Z \rangle$ is given by:

$$\frac{1}{T_1} = \frac{1}{10T_0}\left[\frac{1}{1+(\omega_K-\omega_S)^2\tau^2} + \frac{3}{1+(\omega_K)^2\tau^2} + \frac{6}{1+(\omega_K+\omega_S)^2\tau^2}\right], \tag{2.49}$$

where $\frac{1}{T_0}$ is the zero-field rate, given by:

$$\frac{1}{T_0} = \frac{4}{3}\frac{\gamma_K^2\gamma_S^2\hbar^2 S(S+1)\tau}{r^6}. \tag{2.50}$$

(This result is very similar to eqn. 41 of Solomon [43], with regard to the relaxation of nuclei in a paramagnetic solution.) Eqn.s 2.49 and 2.50 are essentially in the form found in Abragam [37]. A modification presented by Driehuys [30] addresses the numerical reality that not all xenon atoms will be undergoing interaction with a paramagnetic or nuclear site at any given time, and the fraction thereof will be denoted by $f(T)$:

$$\frac{1}{T_0} = \frac{4}{3}\frac{f(T)\gamma_K^2\gamma_S^2\hbar^2 S(S+1)\tau}{r^6}. \tag{2.51}$$

Eqn. 2.49 (with eqn. 2.51) will form the framework for the bulk of the data analysis presented in chapter 5. It contains within it all the correlation time and magnetic field dependencies that will be tested by this experiment.

Chapter 3

Spin Exchange Optical Pumping

Traditional NMR relies upon the relatively miniscule overpopulation of one spin state relative to another spin state in a sample placed in a magnetic field. It is this overpopulation that gives a net magnetic polarization to the sample, ultimately allowing the induction of a signal in a pickup coil through Faraday's law. This miniscule overpopulation can be characterized as a *thermal* distribution, following the Boltzmann thermal polarization equation:

$$Pol._{Thermal} = \frac{N_+ - N_-}{N_+ + N_-} = \tanh\left(\frac{\mu B}{kT}\right). \tag{3.1}$$

When using polarized noble gases for various studies, there is a huge advantage if the polarization of the sample is increased over thermal levels in order to compensate for the relatively low spin density. It was shown by Franzen and Emslie [44] in 1957 that circularly polarized D1 resonance light could be employed to polarize alkali metal vapor to near-complete polarization. In 1960, Bouchiat, Carver and Varnum [45] demonstrated the transfer of polarization from polarized Rb vapor to ^{3}He gas, a process often referred to as spin-exchange optical pumping (SEOP), establishing helium polarization at roughly the ten percent level[1]. Central to the experiments discussed here, ^{129}Xe SEOP has also been demonstrated, following initial work by Grover [47], Volk, Kwon and Mark [48]. SEOP has gone on to become an enormously useful technique in such diverse areas as polarized nuclear targets, medical imaging, and fundamental symmetry violation searches [6].

[1]With the advent of high-intensity laser sources, more recent polarizations have been around 60% [46].

3.1 SEOP Physics

SEOP is a mechanism in which there is a net transfer of angular momentum from a circularly polarized laser beam to an alkali metal vapor (usually rubidium or potassium) and a subsequent transfer of polarization to the nuclei of a noble gas, through either binary or three-body van der Waals collisions. As illustrated in Fig. 3.1, the process begins when circularly polarized light (for definiteness we consider positive circularly polarized light) at the D1 resonance at 794.7 nm is absorbed by valence electrons in the $5^2S_{1/2}$ ($m_j = -1/2$) ground state of the Rb atom, which are then excited to the $5^2P_{1/2}$ ($m_j = +1/2$) state. The $m_j = +1/2$ ground state is prohibited from absorbing the circularly polarized light, as it would need to be excited to an $m_j = +3/2$ state sublevel of the $5^2P_{1/2}$ state which does not exist. In the absence of buffer gas, excited atoms may then relax back to the ground state, with a nonzero probability of ending up in the $m_j = +1/2$ state [5]. In the absence of any Rb-specific relaxation mechanisms, the end result would be that all atoms end up in the $m_j = 1/2$ state. Of course, an absence of relaxation mechanisms is not a physically reasonable condition, and in the case of SEOP of ^{129}Xe, such relaxation is a limiting factor in the alkali-vapor polarization.

Photon absorption by rubidium results in the attenuation of the incident beam as it propagates through the sample according to the relation:

$$\frac{d\Phi}{dz} = -\Phi(\vec{r}, \nu)[Rb]\sigma(\nu)[1 - P_{Rb}(z)], \tag{3.2}$$

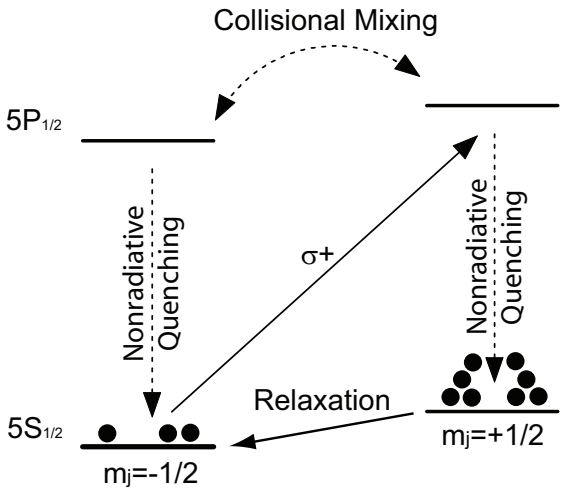

Figure 3.1: SEOP Transitions

where $\Phi(\vec{r},\nu)$ is the incident photon flux of "+" circular polarization, [Rb] is the rubidium number density, $\sigma(\nu)$ is the absorption cross section, and $P_{Rb}(z)$ is the Rb polarization as a function of optical depth. The optical pumping rate of the rubidium in the sample is:

$$\gamma_{opt}(\vec{r}) = \frac{1}{2}\int \Phi^{+}(\nu,\vec{r})\sigma(\nu)d\nu, \tag{3.3}$$

where the + indicates circularly polarized light of the "+" orientation.

The absorption cross section is broadened by interactions with high-pressure Xenon. As discussed by Romalis et al. [49], $\sigma(\nu)$ can be characterized as:

$$\sigma(\nu) = f\pi r_e c\frac{\gamma/2}{(\nu-\nu_0)^2+(\gamma/2)^2}. \tag{3.4}$$

Romalis et al. determined the broadening coefficient γ of rubidium due to collisions with xenon to be $\Gamma = 18.9 \pm .05$ GHz/amg, resulting in 132 GHz for the 7 atm cells

we typically used. The center frequency of the D1 resonance, ν_0, was 3.77×10^{14} Hz, c is the speed of light, f is the D1 oscillator strength of 1/3, and $r_e = 2.82 \times 10^{-13}$ cm, the classical electron radius. The effect of this absorption on the incident spectrum can be seen in Fig. 3.2.

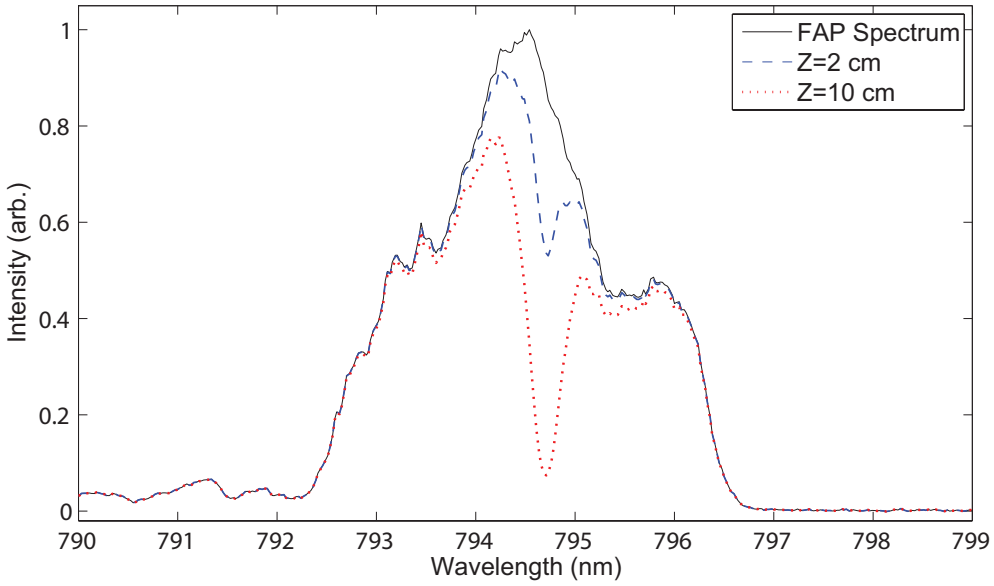

Figure 3.2: FAP Spectrum & Rubidium Absorption. The solid line shows the laser spectrum as measured by a monochromater, the dashed lines show the calculated spectrum following absorption by rubidium at two different optical depths. The modified spectra are calculated according to eqn. 3.2. The xenon density is 7 amg, and the pump temperature is 100 C.

In calculating Fig. 3.2, it is necessary to calculate $P_{Rb}(z)$ at each location of the cell. This polarization is given by the equation

$$P_{Rb}(z) = \frac{\gamma_{opt}(z)}{\gamma_{opt}(z) + \Gamma_e} \tag{3.5}$$

where γ_{opt} is given by eqn. 3.3 and Γ_e is the electronic spin-destruction rate of the

Rb [50]. We note that the factor of 1/2 in eqn. 3.3 is due to the fact that collisional mixing ensures that atoms pumped to the $5^2P_{1/2}$ state rapidly become equalized over the two m_j states. The factor of $\Gamma_e \sim 5.2 \times 10^{-15}\mathrm{cm}^3/\mathrm{s} \times [\mathrm{Xe}]$, and at the pressures exhibited in our cells, it is due primarily to binary RbXe collisions [50]. This rapid relaxation is a limiting factor on the polarization of the high pressure Xe samples studied in this work.

Polarization is transferred between rubidium valence electrons and xenon nuclei through spin-exchange collisions between the the alkali-metal vapor and the noble gas atoms. Both van der Waals molecule formation and binary collisions are possible spin-exchange mechanisms. Using the results of Cates et al. [51], this exchange rate, Γ_{SE}, is given by:

$$\Gamma_{SE} = \frac{1}{T_{1Rb}} = [\mathrm{Rb}]\left(\langle\sigma_{\mathrm{ex}}\mathrm{v}\rangle + \frac{\gamma_{\mathrm{M}}\zeta}{[\mathrm{Xe}]}\frac{1}{1+\mathrm{br}}\right), \tag{3.6}$$

where Cates et al. found $\langle\sigma_{ex}v\rangle$ to be 3.7×10^{-16} $\mathrm{cm}^3\mathrm{s}^{-1}$, $\gamma_M = 2.92 \times 10^4\mathrm{s}^{-1}$, and $\zeta \sim 0.50$. In this work, the $\frac{1}{1+br}$ term is taken to be unity. The first term in eqn. 3.6, representing spin exchange due to binary collisions, contributes $\approx 80\%$ to the computed rate. We note that the conditions under which we polarized our samples were quite similar to those used to make the measurements presented in Cates et. al. [51]. Subsequent measurements by Jau, Kuzma and Happer at high magnetic field make it quite likely that the binary rate was significantly smaller (1.75×10^{-16} $\mathrm{cm}^3\mathrm{s}^{-1}$ [52] rather than 3.7×10^{-16} $\mathrm{cm}^3\mathrm{s}^{-1}$). The discrepancy may be due to a large

contribution from van der Waals molecules or even to a rubidium-number-density related relaxation of the type described by Walker et al. [53]. (It should be noted that Jau et al. documented a decoupling effect for Rb-^{129}Xe and Cs-^{129}Xe binary spin exchange, although it is not likely that the discrepancy mentioned above is due to decoupling.

The spin-exchange rate is crucial for accurate modeling of the SEOP process: not only does it strongly impact the equilibrium value that can be reached through the SEOP (eqn. 3.8), it affects the rate of approach to that equilibrium polarization (eqn. 3.7):

$$P_{Xe}(t) = P_{Rb}\frac{\Gamma_{SE}}{\Gamma_{SE}+\Gamma_{SD}}\left(1 - e^{-(\Gamma_{SE}+\Gamma_{SD})t}\right), \tag{3.7}$$

$$P_{Xe}(t=\infty) = P_{Rb}\frac{\Gamma_{SE}}{\Gamma_{SE}+\Gamma_{SD}}. \tag{3.8}$$

For various reasons, the SEOP of xenon tends to result in smaller polarizations than is the case for helium. One reason is the rapid electronic spin relaxation of the alkali vapor by xenon due to a strong spin-rotation interaction, limiting the alkali vapor polarization. Another is strong wall-relaxation interactions, which rapidly depolarize the xenon gas. The ^{3}He polarization in nuclear target cells routinely exceeds 50 percent using approximately 50W of laser power. ^{129}Xe, on the other hand, rarely approaches the polarizations found in ^{3}He work. In preliminary studies conducted in the fall of 2003, our lab achieved polarizations of roughly 80% for dilute samples of xenon ($\approx$ 1.7% by number density), where the total amount of xenon in the sample was on the order of 5 STP cm^3. While such high polarizations are encouraging, it

must be noted that the small quantities of ^{129}Xe were not sufficient for most imaging applications. For samples of hundreds of STP ccs, the best polarizations were in the 20-30% range, and were achieved using a flowing gas system [24]. Polarization using small high-poressure xenon samples were typically at the one percent level or below.

3.2 Optical System Design

In order to perform spin-exchange optical pumping, we illuminated the cell with high-intensity, circularly polarized light at the D1 line of rubidium (795 nm). In the early days of optical pumping, this light was provided using a rubidium emission lamp with appropriate filters. With the current availability of relatively inexpensive, high-power diode-laser arrays, however, alkali metal polarizations can reach high levels even at high Rb number densities, greatly facilitating various practical applications of SEOP of ^{3}He and ^{129}Xe. This section describes how power was efficiently coupled from these high power diode laser arrays to the cell.

Logistical concerns in our lab dictated that laser power be shared between nuclear target-cell studies and this xenon work. Three high power (30W) Fiber Array Package (FAP) systems manufactured by Coherent, inc. were employed to provide this power. Three fiber lines were coupled into a laser-beam combiner to provide a single compact light source. The combiner enabled the placement of fiber outputs close enough to each other that the same optics could be used to condition and deliver light. (This is in contrast to three sets of identical, but offset, optical pathways, as was used in an

earlier version of our SEOP system).

Light was emitted from an individual combiner output at a large angle of divergence ($\approx 10^\circ$ half angle). This light needed to be brought to the target with an appropriate beam width and collimation such that the cell could optimally absorb it. As an added constraint, the beam needed to fit through optics that had a maximum working aperture of 2".

3.2.1 Gaussian Optics

In order to accurately model the propagation of light through the optics system (as a prerequisite to building it), it was necessary to consider the effects of Gaussian optics on the end result. Many lasers, including the FAP lasers used in this work, exhibit an intensity distribution that follows a roughly Gaussian distribution

$$I = I_0 e^{-2r^2/w^2}, \tag{3.9}$$

where r is the dimension perpendicular to the propagation axis, and w represents the beam width, an effective width for the beam. This width varies along the propagation vector of the beam, with the functional form:

$$w(z) = w_0\sqrt{1 + ((z - z_0)/z_R)^2}, \tag{3.10}$$

where w_0 is minimum beam radius (the beam waist), z is a position along the propagation axis, z_0 the location of the beam waist along the propagation axis, and z_R is a

measure of how rapidly the beam width increases. Eqn. 3.3 is found in the Gaussian Optics discussion of Hecht [55]. The combiner provides up to five individual beam sources, which as mentioned earlier enables the system to use only one set of optics. This fact has unintended consequences. For instance, if an image of the combiner output is formed at the location of the cell, the spatial homogeneity of the beam will be quite poor. This problem is avoided by ensuring that the fairly homogeneous distribution of angles being emitted by the combiner translates into a homogeneous spatial distribution at the cell. Furthermore, by using Gaussian optics, lenses can be chosen so that the width of the beam (appropriately convolving up to five sources in the combiner) is well matched [56]. A simulation of the resulting beam intensity variation as a function of propagation length and off-axis position is provided in figure 3.3, computed from the gaussian parameters measured from the three FAP outputs. The simulation was consistent with measured characteristics of the laser beam, with a beam radius of approximately 1 cm at the location of the cell.

3.2.2 Small Optical Pumping Oven Optics Line

The Small Optical Pumping Oven (SOPO) optics line is shown schematically in Fig. 3.4. Immediately out of the combiner head, the beams were focused by an 8.57 cm focal length lens at 9.3 cm from the combiner in order to roughly collimate the beam. The beam was subsequently passed through a periscope in order to raise the beam and direct it towards a 2" polarizing beam-splitter cube. Light transiting along the reflection path of the cube was sent through a quarter wave plate, reflected

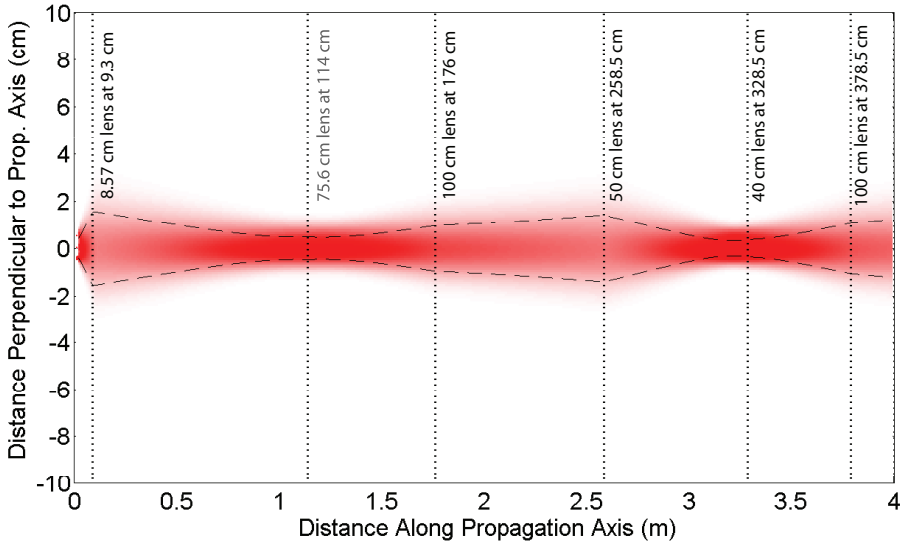

Figure 3.3: Gaussian Beam Intensity Simulation Plot. The dashed line indicates the beam width calculated from eqn. , while vertical lines indicate lens focal lengths and locations. This is the same optical setup seen in Fig. 3.4. All lenses are biconvex lenses from Thorlabs, coated with antireflective coating AR.16.

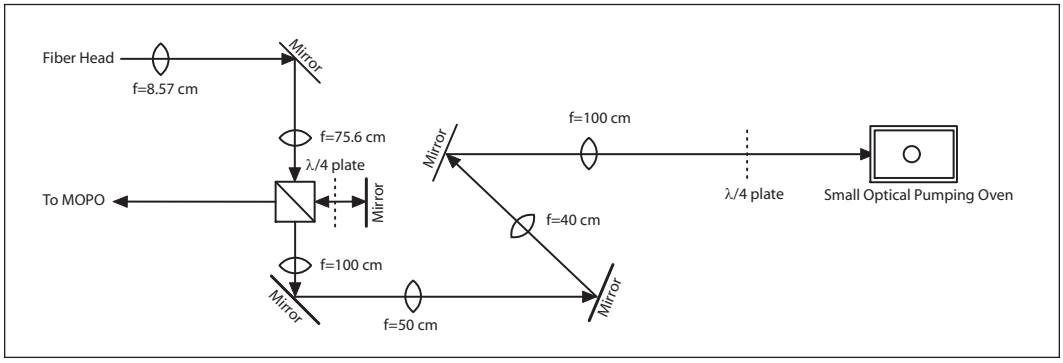

Figure 3.4: The Small Optical Pumping Oven Optics Line

normally, returned through the quarter wave plate, transmitted through the beam-splitter cube and passed on to the large main optical pumping oven. The beam passing through the transmission path of the beam-splitter cube was passed through another set of lenses and mirrors, through another quarter wave plate, and on to the Small Optical Pumping Oven, a beam path from source to target of approximately 400 cm. The beam width at the target was approximately 1", and the location along the propagation axis where the the beam had maximum homogeneity across the cell dimensions was within 2 cm along the propagation axis of the target center.

The purpose of the optics line was to convert the unpolarized, divergent cone of light emanating from the fiber head into a spatially homogeneous and reasonably well collimated beam of light with the appropriate beam width for illuminating the cell.

With approximately 20 W light (relative to the $\approx$ 50 W output power at the combiner) incident upon the cell under operation of two FAP units, roughly 2 cm diameter beam spots could be placed within a 0.5 cm center-to-center distance of each other at the location of the cell. Under these conditions, cells with 7 atm of ^{129}Xe could be polarized to a polarization of $\sim 10^{-3}$%.

While in appropriate conditions, polarizations of approximately 80% were achieved using dilute samples of xenon, polarizations of larger xenon samples appropriate for imaging studies tend to be well under 20% for the vast majority of imaging studies reported in the literature. For many polarization techniques employed, and certainly those used here at UVA in the medical school, reliable reduction in wall-relaxation rates would greatly improve performance and boost polarizations. In fact, better

control over wall relaxation could even stimulate the development of new polarization techniques.

3.3 The Polarization Procedure

In all tests, the cell polarization process began with placing the cell in the pre-heated oven at the center of the laser beam. The oven itself was at the center of a home-built Helmholtz coil which provided a magnetic holding field of $\sim$ 15 Gauss, and heating was provided through forced-air heating. Typical pump temperatures were around 100 C for xenon SEOP, lower than for studies using more dilute samples [24]. The oven and coil system were not equipped with any form of polarimetry equipment, so it was necessary to physically transport the cell from the oven to the spectrometer. With the removal of the cell from the SEOP oven, the rubidium vapor present in the cell, then unpolarized with no laser illumination, would begin acting to depolarize the xenon. It was thus of the utmost importance to remove the influence of the vapor by plating it out on the cell walls rapidly[2]. This plating-out was accomplished by immediately plunging the cell into a 500 mL beaker of chilled water. The beaker doubled as a carrying case, cooling the cell for the roughly 10 second trip to the spectrometer. It should be noted that this transit process was a compromise between the desire to minimize depolarization due to the rubidium vapor (suggesting we keep the cell submerged longer) and depolarization due to relaxation in a low ambient field

[2]In addition to enabling the retention of gas polarization long enough for it to be measured, this was also of obvious importance because it allowed the measurement of relaxation mechanisms *other* than that due to rubidium interactions.

(suggesting we deliver the cell to the spectrometer as quickly as possible). In the end, it was decided that the 10 to 20 second dip in the beaker was sufficient to plate the bulk of the rubidium vapor onto the walls, and that further equilibration to operational temperature would be accomplished in the high-field environment of the spectrometer probe. After placement in the probe, a period of roughly 30 seconds was typically allowed to pass before signal acquisition, chosen to allow that the temperature of the cell to equilibrate.

Chapter 4

Hardware, Data Acquisition, and the Determination of $\frac{1}{T_1}$

Execution of the experiment forced the design and construction of custom-built apparatus. Central to our needs was a pulse NMR spectrometer with which we could measure relaxation lifetimes of gaseous samples as short as 10 seconds. In concert with the spectrometer, a flowing gas temperature control system was implemented in order to regulate sample temperature between roughly 200 K and 350 K. Also needed was an optical line (separate from the pre-existing nuclear target polarization optics) with characteristics appropriate to the small xenon sample cells used. Samples (small pressurized cells between 2 cm and 1" in diameter) were created locally and filled on an existing gas system with appropriate contents to provide a large nuclear signal and controllable wall chemistry.

4.1 Pulse NMR Spectrometer

The Pulse NMR Spectrometer was based upon the design built by Brian Saam [57], who in turn based his design upon one built by Mark S. Conradi. The present design preserves some features from previous designs, specifically the wide range of operational frequencies and the admissibility of very short lifetime values, while discarding other features deemed not relevant to the current experiment, most specifically the field stabilizer. (Un-augmented stability of the power supply was sufficient for the studies conducted here.)

While our group at UVA has extensive experience in continuous wave (CW) techniques, it was decided early on that pulsed measurements were more appropriate to

the measurement of longitudinal relaxation times (denoted by T_1 [58]) that we believed would be very short. Adiabatic fast passage (AFP), the CW technique of historical choice, has the unfortunate practical limitation of requiring substantial amounts of time (~ 30 s) to acquire a polarization measurement. While AFP results in minimal polarization losses per measurement ($< 1\%$), it is better suited to T_1 measurements on the order of thousands of seconds or longer. Furthermore, AFP requires multiple sets of coils (addressing both sample excitation and signal reception), and would be impractical in the tight confines defined by the iron pole faces of our electromagnet.

Pulse measurements, on the other hand, were deemed to be quite suitable for the purposes of this experiment. The duration of a pulse measurement is determined by the transverse relaxation time (T_2) of the sample [58], found in this work to be typically on the order of milliseconds, allowing almost any T_1 duration to be effectively measured. Polarization losses, while substantially higher than with AFP, are quite easily controllable and straightforward to determine. When implemented appropriately, pulse measurements allow the use of a single coil for both spin tipping and observation.

4.2 Mechanics of Pulse NMR

Pulse NMR detection involves the brief application of RF energy tuned to the sample's Larmor frequency. In the laboratory frame, the field at the sample can be viewed as

the vector summation of the main holding field and the RF field:

$$\hat{H} = H_0\hat{z} + H_1\cos(\omega_0 t)\hat{x}, \tag{4.1}$$

where $\omega_0 = \gamma H_0$ [35]. Viewed from a frame rotating at angular frequency ω, however, eqn. 4.1 becomes:

$$\hat{H} = (H_0 - \omega/\gamma)\hat{z'} + 1/2H_1\cos[(\omega - \omega_0)t]\hat{x'} + 1/2H_1\cos[(\omega + \omega_0)t]\hat{x'}. \tag{4.2}$$

When $\omega = \omega_0$, the main field component disappears and the co-rotating orthogonal field appears constant (the double-frequency component is disregarded):

$$\hat{H} = 0\hat{z'} + 1/2H_1\cos(0t)\hat{x'}. \tag{4.3}$$

At resonance in the rotating frame, the spin sees a constant field of magnitude $1/2H_1$ orthogonal to the vector of its angular momentum. As a result, the spin precesses through an angle θ given by

$$\theta_{tip} = 1/2\gamma H_1 t_{pulse}, \tag{4.4}$$

where the pulse duration is given by t_{pulse}. At the conclusion of the pulse, the spin has been tipped away from the holding field by angle θ and remains at constant orientation in the rotating frame. Transforming back to the laboratory frame, however, the spin is

now oriented at an angle to the holding field and precesses around it at frequency ω_0. The component of the spin orthogonal to the holding field is then available, through Faraday's Law, to induce a signal in a suitably placed coil. This signal is known as a Free-Induction-Decay, or FID. Its amplitude is given by:

$$\text{Amplitude} \propto \mathrm{M_z} \sin(\theta_{\mathrm{tip}}) \tag{4.5}$$

where M_z is the magnetization of the sample.

The tip loss can be considered to be the difference in longitudinal polarization value before and after the pulse since the component orthogonal to the field experiences T_2 dephasing. With the immediately post-tip polarization oriented at an angle θ_{tip} to the field, it can then be seen that the loss is proportional to the difference between the projection of the magnetization onto the z axis before and after the pulse:

$$\text{Loss} = \mathrm{M_z} - \mathrm{M_z} \cos(\theta_{\mathrm{tip}}) = \mathrm{M_z}[1 - \cos(\theta_{\mathrm{tip}})] \tag{4.6}$$

4.3 The Pulse NMR System

The spectrometer was designed to be flexible and modular - changing frequency was simply a matter of changing or retuning the probe and selecting an appropriate reference frequency. It was also designed with

Control was provided by a 2 GHz processor computer running Labview 7.0 on a Windows XP operating system. The computer interfaced with a programmable

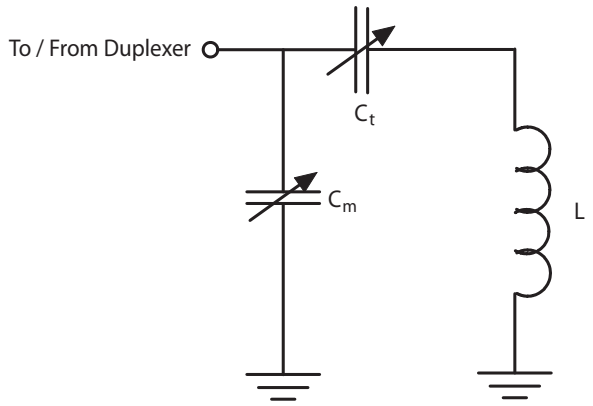

Figure 4.1: Tank Circuit Schematic

signal generator, which provided the pulse trigger signals for the switching electronics, the RF generator, and the storage oscilloscope. Amplifier Research 10 W and 25 W amplifiers boosted the RF output to the probe, and a bipolar amplifier boosted signal from the probe before entry into the spectrometer electronics.

4.3.1 The Tank Circuit

NMR probes were constructed by winding solenoids around teflon forms inside of which the polarized gas cells could be placed. A resonant circuit was then created by the introduction of a tuning capacitor in series with the coil. The resonance frequency of the circuit was set to coincide with the Larmor frequency of the sample, allowing the efficient detection of the signal.

The resonance frequency of the circuit was found as the point where capacitive reactance exactly canceled out inductive reactance, giving a minimum and purely real

impedance:

$$Z = R + i(X_C + X_L) = R + i(\omega L - \frac{1}{\omega C_T}), \tag{4.7}$$

leading to a resonance frequency

$$\omega_{res} = 2\pi f_{res} = \sqrt{\frac{1}{LC_T}}. \tag{4.8}$$

Here, L is the inductance of the coil, C_T the tuning capacitance, and R the resistance of the circuit at the operational frequency. It is important to note the difference between the DC resistance of the coil and the resistance at frequency due to "skin effects", wherein high frequency AC signals conduct within a small depth from the surface of the wire, causing resistance at high frequency to be many times higher than at DC. An attempt to bypass this limitation was pursued through the use of Litz wire, wherein the traditional single-strand wire is broken into a series of smaller diameter wires, each individually electrically insulated. The goal of such an arrangement is to force more of the wire's cross section to be within one skin depth of the surface of the wire, maximizing the available conductance cross section and minimizing the resistance.

In order to efficiently couple the signal from the tank circuit into the rest of the detection apparatus, the impedance at resonance must be matched to the input impedance of the front-end preamplifier (in these experiments, the pre-amplifier used had an input impedance of 50 Ω). In the case of tank impedance greater than 50 Ω, a matching capacitor was introduced in parallel to the tank circuit such that the

equivalent impedance was brought close to 50 Ω. This arrangement, a capacitor in parallel with a resonance tank circuit, is referred to in electrical engineering literature as a capacitance-tapped tank circuit [59].

At resonance, the magnitude of the impedance is given by

$$|Z| = \frac{\sqrt{\frac{L^2 C_t^2}{[C_m(C_t+C_m)]^2} + \frac{R^2 L C_t}{C_m(C_m+C_t)}}}{R}, \tag{4.9}$$

reducing to the following, when $R^2 \ll LC_t$:

$$|Z| = \frac{LC_t}{RC_m(C_m + C_t)}. \tag{4.10}$$

Here, L is the inductance, C_t is the tuning capacitance, C_m is the matching capacitance, and R is the resistance of the coil at the resonance frequency [59]. In order to maximize power transfer from the tank circuit to the detection circuit, attempts were made to make $|Z|$ equal to the 50 Ω Z_{in} of the pre-amplifier. The reflection coefficient for a signal encountering an impedance mismatch is given by the formula:

$$K_{reflection} = \frac{A_{in}}{A_{out}} = \frac{Z_0 - Z_L}{Z_0 + Z_L}, \tag{4.11}$$

where Z_0 is the characteristic impedance of the transmission line, and Z_L the impedance of the load. In practice, the tank's output impedance was considered "good enough" when it fell between 100 Ω and 25 Ω ($|K_{reflection}| \leq 1/3$).

A tank circuit is given its name as a consequence of its ability to store energy in

the form of electric and magnetic fields - but the real-life nature of the components used results in the introduction of resistance in the circuit which causes the energy stored in the tank to dissipate over time. A measure of the circuit's storage capacity relative to its loss rate is specified by its quality factor, or Q, given by:

$$Q = \frac{\omega L}{R}. \tag{4.12}$$

In terms of frequency response, Q is an indicator of the selectivity of the resonant circuit – higher Q translates to narrower bandwidth, and vice versa. The Q value for a circuit has implications for data acquisition: high Q circuits retain excitation energy proportionally longer than low Q circuits, resulting in increased ring-down time following a pulse, necessitating a longer dead-time in acquisition; narrower bandwidth results in greater noise suppression at frequencies other than the frequency of interest; a wide bandwidth accommodates holding field drift more readily than a narrow bandwidth. These competing effects, along with the reality of a practical limit on how large the ratio of L to R could be made (greater L required more wire, leading to more resistance), resulted in most probes having a Q of between 50 and 80. The functional benefit of the single-coil duplexing scheme is that it allows the same coil to perform both excitation and detection, meaning that the (nontrivial) tuning and impedance matching efforts need only be performed once at each frequency. Additionally, the reciprocity theorem implies that the same resonance characteristics of the coil that allow detection of very small signals will permit efficient generation of a

large H_1 tipping field, permitting short duration, broadband stimulation.

4.3.2 Spectrometer Capabilities

Multifrequency operation was central to the experiment, and was easily achieved using our design. Through a process known as "superheterodyning", nuclear signals were mixed to a fixed intermediate frequency before being mixed back down to audio frequencies for acquisition on a storage oscilloscope.

In superheterodyning, the NMR signal at frequency F_L is mixed with a variable reference frequency F_{Ref1} to a resultant frequency of $F_{IF} = F_L \pm F_{Ref1}$. F_{IF} is then mixed down with a second fixed reference frequency F_{Ref2} to audio frequency. In these experiments, $F_L = \gamma B$, ranging between $\approx$ 500 KHz and 11.5 MHz. F_{Ref2} was fixed at 10 MHz. F_{Ref1}, consequently, was set to be equal to the difference of F_L and (10 MHz $\pm F_{audio}$). Typically, F_{audio} was set to 20 KHz so as to center the output frequency between the last-stage preamplifier bandpass filter points at 10 KHz and 30 KHz. Placing a $\pm$10 KHz window around the desired final frequency placed looser constraints on field stability, preventing slow field drift from causing falsely increased relaxation rate observations. This was particularly important for measurements of very long T_1 values, as longer measurement intervals enabled larger absolute field drifts. For fields below 1.86 MHz, however, field stability was such that frequency drift rarely exceeded several hundred Hertz. At these fields, it was possible to reset the output audio frequency to 10 KHz and place the upper and lower bandpass filter points at 10 KHz.

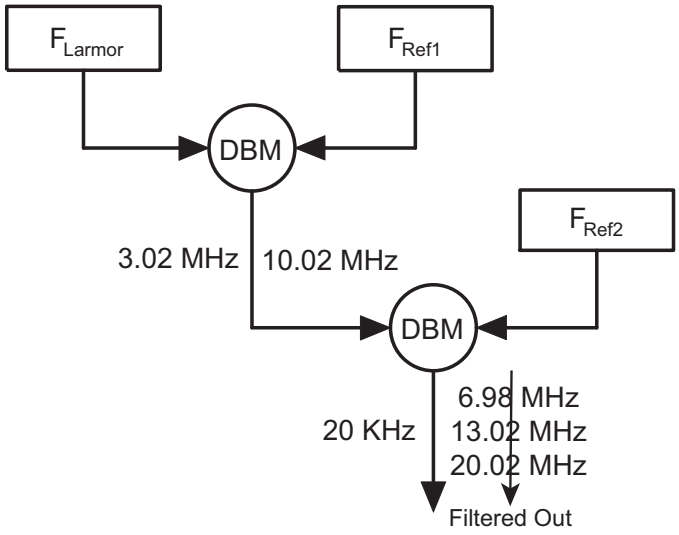

Figure 4.2: Superheterodyning Frequency Schematic

The pulse NMR spectrometer was constructed using commercially available function generators, switches, mixers and amplifiers. A data acquisition sequence was initiated via a trigger signal sent from the data acquisition (DAQ) computer to the gate signal generator. The gate signal generator output a gate signal consisting of a single TTL pulse, with the duration of the pulse set equal to the desired value of t_{pulse}. The gate signal provided the overall timing signal for the spectrometer, gating the output from the RF signal generator, activating two isolation switches, and triggering the data acquisition oscilloscope. The RF signal generator was set to output a gated burst of RF energy at the Larmor frequency of the sample (this frequency was set before operation). Next, the output from the RF signal generator was sent into an electronically controlled single-pole double-throw isolation switch. This switch, the first of two (and henceforth to be referred to as Switch #1), was

configured so that the input port was shunted to a 50 Ω terminator when the gate signal was low. With the gate signal high, Switch #1 sent the output to the RF amplifier through a pair of crossed diodes. Use of Switch #1 was intended to prevent unintended signal and noise originating in the RF signal generator from making it to the RF amplifier. The crossed diodes between Switch #1 and the RF amplifier was intended to provide a backup to the action of the switch, preventing noise above the ∼0.5 V level from passing to the RF amplifier. The RF amplifier boosted the power of the pulsed RF signal, permitting short-duration and broadband stimulation of the sample. Immediately following the output from the RF amplifier, another pair of crossed diodes attenuated noise from the RF amplifier. The high voltage of the signal was minimally impacted by the voltage drop from the diodes. Following the RF amplifier and crossed diodes, the signal was immediately coupled in parallel to the RF probe and a quarter-wave line. The quarter-wave line was simply a BNC cable cut to the length of 1/4 of the wavelength of the Larmor frequency, terminated in parallel to the remaining electronics and a pair of crossed diodes going to ground. This arrangement of the probe, quarter-wave line and crossed diodes served as a simple and effective duplexing scheme, allowing the same probe to be used for RF transmission and signal reception [60]. For large amplitude signals coming from the RF amplifier (large is defined relative to the threshold voltage of the diodes used), the first set of diodes exerts a negligible voltage drop on the signal. The set at the end of the quarter-wave line behaves as a short to ground, resulting in negligible signal propagation down the quarter-wave line. As a result, the bulk of the transmitted

RF signal couples to the probe. For signal detection, the crossed diodes serve as an effective barrier to the propagation of the small signals induced in the coil, and consequently those signals propagate away from the RF amplifier, bypass the crossed diodes at the end of the quarter-wave line, and flow directly into the second isolation switch (Switch #2). Switch #2 is configured to shunt the input signal to a 50 Ω terminator when the gate signal is high, preventing the sensitive pre-amplifier from seeing any high-voltage signal that may leak by the duplexing scheme, and directly connects to the sensitive pre-amplifier when the gate signal is low. The low-noise preamplifier manufactured by Miteq Inc. boosts the signal by a factor of roughly 80. The boosted signal output from the pre-amplifier is then sent into a double-balanced mixer, where it its mixed with the signal from a reference signal generator outputting a constant signal. The output frequency of the reference signal generator is set to be equal to 10 MHz ± the desired audio frequency ± the Larmor frequency of the sample (the choice of the audio frequency and the reference frequency is detailed in the previous paragraph discussing superheterodyning). Output from the mixer was then sent into a power splitter. The second splitter input was a 10 MHz square-wave signal from the synchronization output of the reference generator (after passing the square wave through a low-pass filter set to 10.7 MHz, all significant higher harmonics were removed). The power splitter output two signals, one 90° out of phase from the other, and each signal consisting of a component at F_{audio} and a component at 20 MHz + F_{audio}. These signals, labeled the "I" and "Q" channel, were each then passed through a SR560 pre-amplifier with bandpass filter points set as discussed in

the previous paragraph detailing superheterodyning. The outputs from the last-stage pre-amplifiers were then sent to separate channels on a digital oscilloscope with storage capability. Signal acquisition by the scope was triggered by the falling edge of the gate generator signal. Following acquisition by the scope, the two channels were sent to the DAQ computer via GPIB and retained for post-processing.

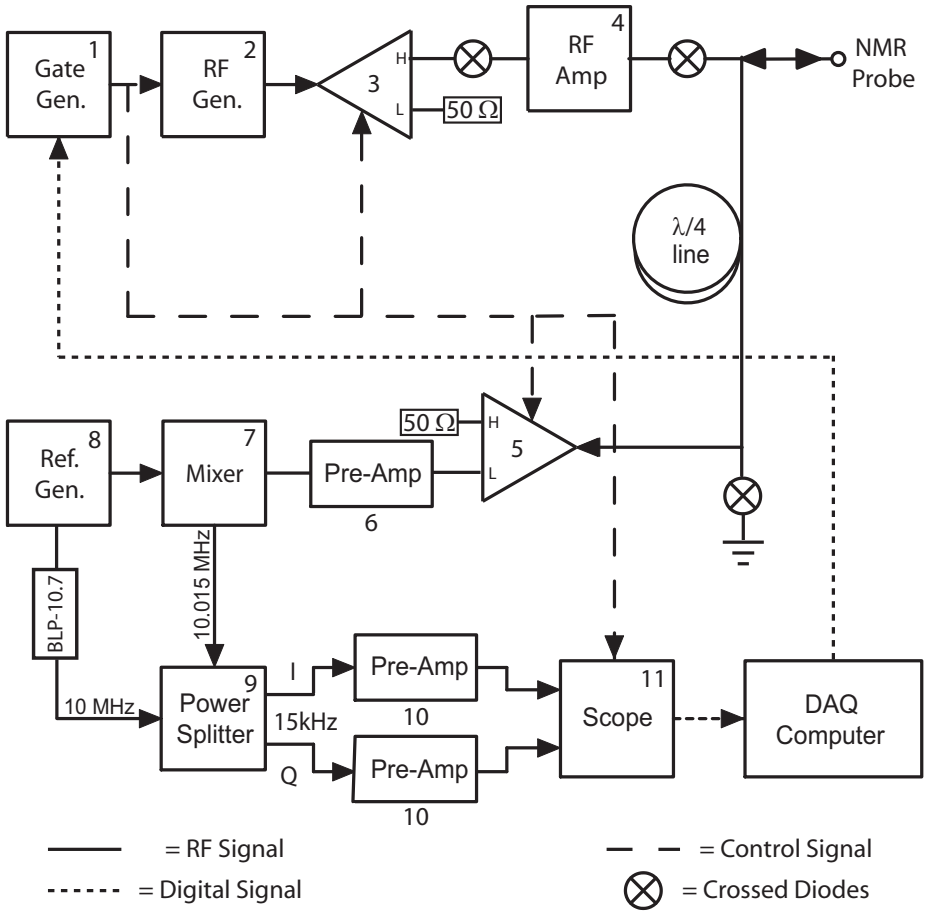

Figure 4.3: Pulse NMR Spectrometer Schematic. The part numbers for each component are as follows: **1**, Gate Signal Generator, Agilent 33220A Function Generator; **2**, RF Signal Generator, Agilent 33250A Function Generator; **3**, Isolation Switch #1, Mini-Circuits ZYSWA-2-50DR Switch; **4**, RF Amplifier, Amplifier Research 25A100 Power Amplifier; **5**, Isolation Switch #2, Mini-Circuits ZYSWA-2-50DR Coaxial Switch; **6**, Low-Noise Preamplifier, Miteq AU-1583-9405-BNC; **7**, Double-Balanced Mixer, Mini-Circuits ZAD-8 Frequency Mixer; **8**, Reference Signal Generator, PTS-310 Frequency Synthesizer; **9**, Quadrature Power Splitter, Mini-Circuits ZMFIQ-10D; **10**, Filtering Pre-Amplifier, Stanford Research Systems SR560; **11**, Digital Storage Oscilloscope, Tektronix TDS3032B.

4.4 The Magnet

To provide the magnetic field we employed a Harvey-Wells 1.4 T water-cooled electromagnet that was serendipitously discovered in departmental surplus, tracing its history back to the doctoral work performed by Açar Isin[1] under the guidance of Dr. Robert Coleman. In operational-envelope investigation tests, the magnet was confirmed to be capable of creating a field of 1.35 T at the center of the pole gap. When powered by a 65 A Walker Scientific HS-1365 power supply and used for relaxation rate measurement experiments, the magnet was capable of providing magnetic fields up to and above 1 T.

4.4.1 Field Shimming

In its unmodified state, the magnetic field exhibited approximately 750 ppm homogeneity over a 1" volume at the center of the pole gap. Quite unsuitable for NMR signal acquisition, the inhomogeneity of the field necessitated shimming of the field to the point where T_2 values were on the order of hundreds of microseconds or longer.

Shimming was accomplished by constructing two pairs of shim coils with configurations appropriate to the order and dimension of the field correction: a pair of antihelmholtz coils, 6" in diameter, were employed to cancel first order gradients in $\hat{z}$, while a smaller pair 2" in diameter were nested inside the linear correction coils. The smaller quadratic correction coils were energized in a parallel fashion, and as is

[1]Dr. Isin is presently a Visiting Professor of Physics at UVA.

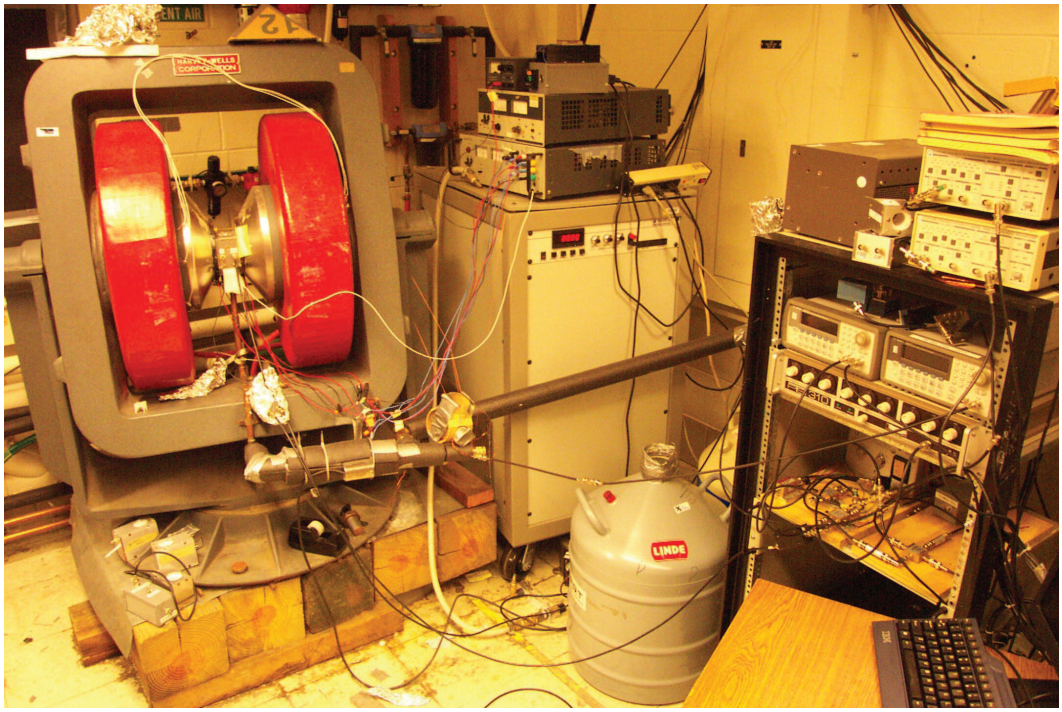

Figure 4.4: The pulse NMR spectrometer setup. On the left is the Harvey-Wells electromagnet, at the center is the Walker HS-1365 power supply, and at the right is the spectrometer-electronics rack and DAQ computer. On the ground near the center of the photograph and partially obscured behind the electronics rack are the liquid nitrogen dewars that served as the chilled gas source.

obvious from their name, canceled out second order gradients in $\hat{z}$.

No attempt was made to cancel out gradients in the $\hat{x}$ and $\hat{y}$ directions - to do so would have required correspondingly additional coils, and as a result constrained access to the center of the bore. Perhaps more significantly, correction in these dimensions would have required hardware in the form of additional power supplies which were not readily available. Fortunately, T_2 values could routinely be extended to several milliseconds by use of the $\hat{z}$ coils and careful placement of the probe and sample at the center of the bore. Transverse relaxation times for 3.5 MHz water signals in 2 cm cells could be extended to ≈ 10 ms through careful shimming and probe placement.

4.5 Temperature Control Apparatus

A heating and chilling system was implemented to vary the temperature of the cell while it was inside the NMR probe. To implement this, a $\frac{1}{2}$" O.D. copper line was run from just below the probe (the probe was open on the underside, to allow for through-coil flow) to a HotWatt^{TM} 200 W low air-resistance electric heater affixed to the flux-return yoke of the electromagnet, and onward to a junction of a forced air inlet and a cold gas inlet.

Heater control was in the form of an Omega PID controller keyed to an RTD mounted to the outlet of the gas line, before the gas flow entrance to the coil. It was imperative to ensure that the RTD was not located *inside* the probe coil, as RF pickup from the RTD would irrecoverably corrupt FID signal acquisition.

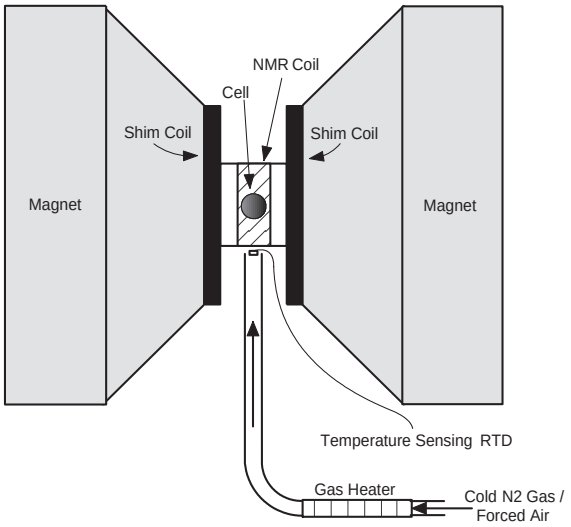

Figure 4.5: A simplified schematic of the NMR apparatus temperature control hardware. The sample cell was placed in the probe at the center of the magnet's open bore. Cold nitrogen gas or forced air was passed over the gas heater for fine control of the sample temperature. The RTD just beneath the probe measured the gas temperature just before the gas entered the probe and provided feedback for control.

4.5.1 Forced Air Heating

For heating the cells, air was drawn from the Physics Building's main compressed air line at a rate of 4 standard cubic feet per minute (SCFM) and heated to the desired temperature. Temperatures from 25° C to 50° C were achieved, and temperature stability was approximately 0.2° C.

4.5.2 Cryogenic Cooling

For temperatures below 25° C, the air line was shut and a 1" O.D. foam-insulated copper pipe was connected between the heater line junction and the chilled gas source. The chilled gas source was a 1" O.D. copper pipe with a 50 W HotWatt^{TM} cartridge heater mounted on its end. The heater was submerged in a 25L liquid nitrogen

dewar. Connecting the heater to a variac-modulated AC power source allowed the liquid nitrogen to be boiled off. The cold nitrogen gas passed through holes in the side of the 1" pipe and flowed through the transfer line to the heater, where fine control of the temperature was effected by the RTD/PID/heater combination. Temperatures from room temperature to as low as -80° C could be reached with this combination, with stabilities from 0.3° C in the range of 0° C to −50° C, and roughly 1°C below.

The chilled-gas source heater was typically run at 90% of AC line voltage. The run time of the liquid nitrogen dewar could be extended by throttling back the boiloff rate, but the consequently lower flow rate would permit unacceptable temperature gradients across the cell. For data acquisition, the cells were run with the boiloff throttle at the aforementioned 90% and temperature control was primarily through the flow heater.

A study of temperature gradients was undertaken prior to low-temperature relaxation rate data acquisition. To roughly measure average cell temperature and temperature gradients, 3 RTDs were affixed to an unpressurized 1" diameter glass cell in evenly-spaced intervals around and along the cell. At the lowest temperature measured in the gradient study, -50° C, the average temperature was -47° C ± 3.7° C. At this set temperature, the source heater voltage was set at 90% of line voltage. Higher set temperatures were paired with lower source heater voltages, and resulting gradients were understandably higher due to the lower flow. It was decided that for below-room-temperature work, the source heater voltage would be set at 90% or higher in order to minimize undesired gradients.

4.6 Free Induction Decay Analysis

The FID itself is an exponentially-decaying signal precessing at the Larmor frequency of the chemical species in the field of question. With A_0 describing the initial amplitude of the signal, ω_0 giving the Larmor frequency (in rad/s) and T_2 describing the dephasing time of the FID, time-domain data can be modeled as:

$$FID(t) = A_0 \cdot Re(e^{i\omega_0 t} e^{-t/T_2}). \tag{4.13}$$

For the bulk of this study, the Larmor frequency was well into the MHz range. From the standpoint of probe fabrication, this was a rather convenient range (given typical probe geometry and available electronic components, 1-12MHz hardware was easy to contruct). From a data acquisition standpoint, however, this was a challenge - in order to resolve the envelope of the natural FID, it was necessary to set the sampling frequency so low that the oscillation was unresolved. This was why we chose to mix the signal down to audio frequencies of 10 to 20 KHz.

Mixing follows the mathematical equalities detailing the product of two frequencies:

$$\cos(\omega_1 * t) * \cos(\omega_2 * t) = \cos[(\omega_1 + \omega_2) * t] + \cos[(\omega_1 - \omega_2) * t] \tag{4.14}$$

and

$$\cos(\omega_1 * t) * \sin(\omega_2 * t) = \sin[(\omega_1 + \omega_2) * t] + \sin[(\omega_1 - \omega_2) * t]. \tag{4.15}$$

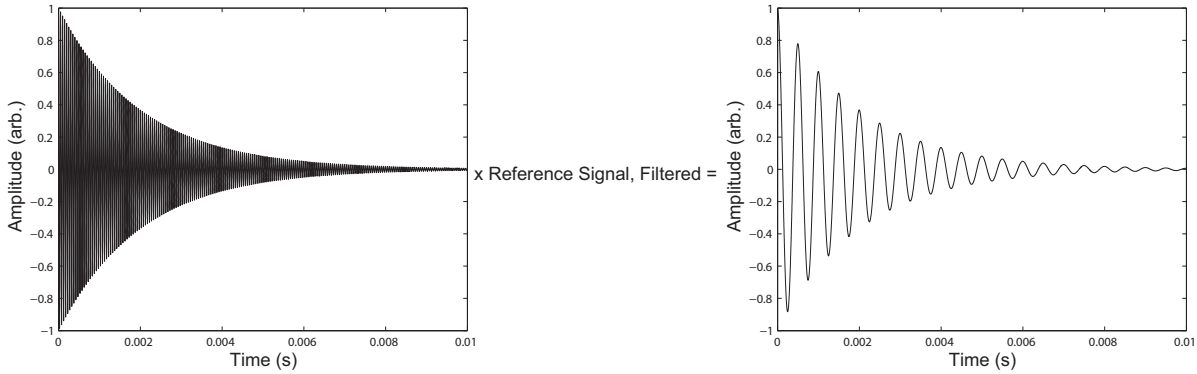

Figure 4.6: Mixing the FID frequency downward preserves the FID envelope features. On the left is a non-mixed-down FID, where the Nyquist frequency is above the sampling rate - consequently, the oscillation of the FID is unresolved. On the right is a mixed-down FID, where the Nyquist frequency is below the sampling rate - consequently, the oscillation is resolved.

Within the range of operational frequencies, the mixer was considered to be a linear device, and so structural features in the RF FID were preserved in the mixed-down rendition. Consequently the analysis intended for the unaltered signal could be employed on the frequency-shifted one. This characteristic eased operation, as the collection of mixers could be considered essentially black boxes.

The shift from nuclear frequencies to audio frequencies was indirect, as per the superheterodyning feature, with the signal first being shifted to 10.015 MHz before being passed into a quadrature splitter referenced to 10 MHz. A quadrature splitter behaves like a pair of parallel mixers accepting a common NMR signal and reference signal, with the exception being that one reference signal is shifted from the other by 90 degrees of phase. The output from the splitter is a pair of mixed-down NMR signals, the second signal 90 degrees out of phase to first. The benefit to using such a device is a roughly 40% boost in signal to noise ratio during post-processing, owing to

the correlated signals of the two channels adding coherently while uncorrelated noise adds incoherently [60]. While the non phase-shifted (the "I" channel, for in-phase)

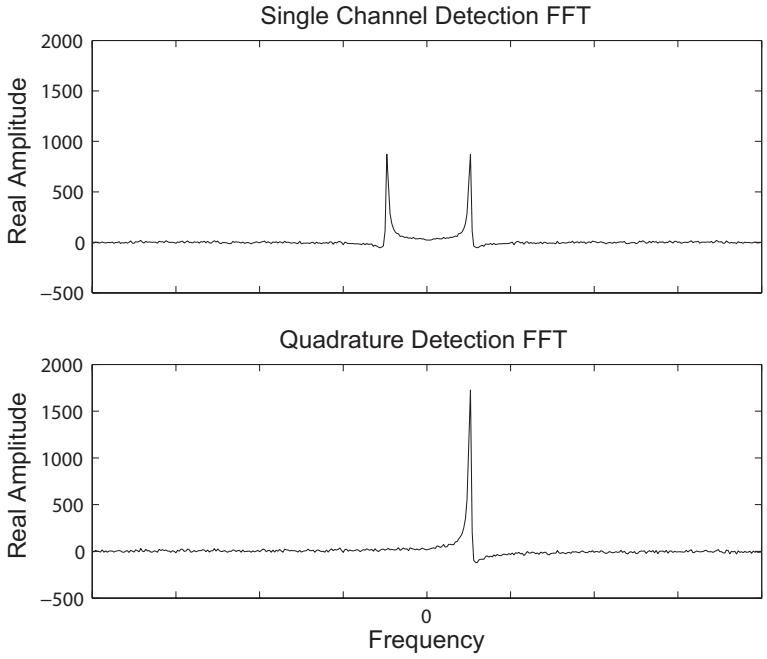

Figure 4.7: Quadrature Detection Enables Resolution of Frequency Polarity

channel corresponds to equation 4.13, the 90 degree phase shifted channel (the "Q" channel) represents its imaginary counterpart:

$$Q(t) = A_0 \cdot Im(e^{i\omega_0 t} e^{-t/T_2}). \tag{4.16}$$

4.7 Data and Error Analysis

FID data were stored as three-column data on the DAQ computer, with one column representing elapsed time in the acquisition, one representing the I channel data,

and the third representing the Q channel data. The first 20 to 50 microseconds of the acquisition were omitted from the analysis in a given tiptest/spindown test (the same time for each FID), in order to eliminate signal corruption by probe ringdown and suplexer switching electronics. A set of zeroes equivalent to the duration of the omitted section was then added to the trailing end of the data set in order to retain overall acquisition duration. A visual representation of this process is found in figure 4.8.

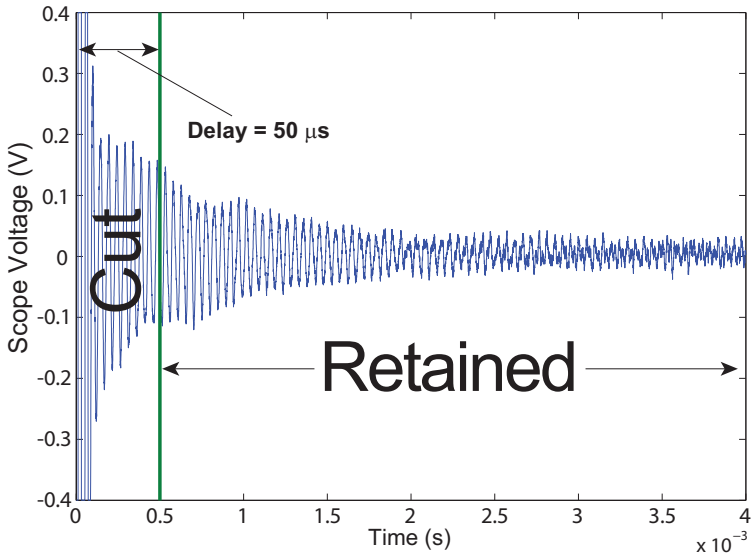

Figure 4.8: Trimming early data from the FID

4.7.1 Zero Padding

Following acquisition and early-signal trimming, the raw signal consisting of 10000 points was "zero padded" to a total point number of 2^{15}, or 32768 points. "Zero padding" involves increasing the number of points in a data set by appending a

number of zero-valued elements to the trailing end of the data set. This common technique was performed in order to compress the frequency interval in the discrete Fourier transform, resulting in greater coverage over the peak and permitting a less ambiguous fit [60] [61]. The frequency spacing Δf_{raw} in the Fourier transform is given by

$$\Delta f_{raw} = \frac{1}{\#\text{points}_{\text{raw}} * \Delta\text{t}}. \tag{4.17}$$

In eqn. 4.17, the number of points in the original, unpadded data set is given by $\#points_{raw}$. The time interval between points is given by Δt. Increasing the total number of data points from $\#points_{raw}$ to $\#\text{points}_{\text{pad}}$ results in a compressed frequency interval, given by

$$\Delta f_{pad} = \frac{\#\text{points}_{\text{sig}}}{\#\text{points}_{\text{pad}}} \Delta f. \tag{4.18}$$

An example of the Zero Padding of a FID acquisition is illustrated in Fig. 4.9. The number of points padded on the original signal was chosen in order to make the frequency interval much less than the Full-Width Half Maximum (FWHM) of the Fourier-transformed FID. This compression is illustrated in Fig. 4.10.

Curves representing the real and imaginary pieces of the functional form of the Fourier transform were then fit to the corresponding data:

$$FFT[FID(t)] = \int_{-\infty}^{\infty} A e^{i\omega_0 t + \phi} e^{-t/T_2} e^{-i\omega t} dt = A \frac{\cos(\phi)/T_2 + i\sin(\phi)(\omega - \omega_0)}{(1/T_2)^2 + (\omega - \omega_0)^2}. \tag{4.19}$$

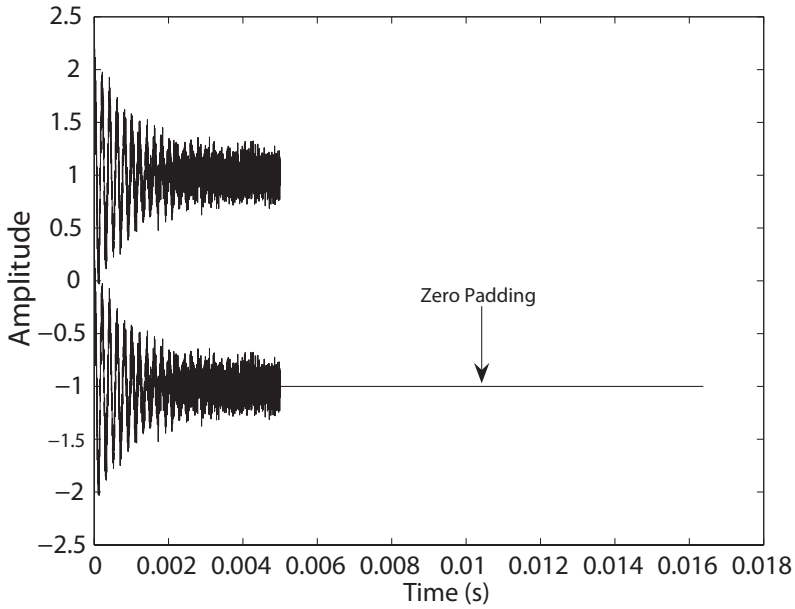

Figure 4.9: Padding the FID

Examples of these fits are illustrated in Fig. 4.11. Fitting to both the real and imaginary transforms allowed the amplitude, width, peak frequency and initial phase to be determined. While information on the initial phase was somewhat unimportant given the uncontrolled phase of the reference signals, the other fit parameters provided information relevant to the acquisition process: peak frequency provided information on field drift; width provided information regarding T_2 and consequently field homogeneity; and amplitude provided information regarding the polarization of the sample, the quantity of primary interest. Over the course of a typical acquisition, peak frequency rarely drifted by more than 100 Hz, and width rarely more than 10 Hz - on the occasion where the fit produced a fit parameter grossly inconsistent with the width parameters of the other FID acquisitions in the sequence, the FID was

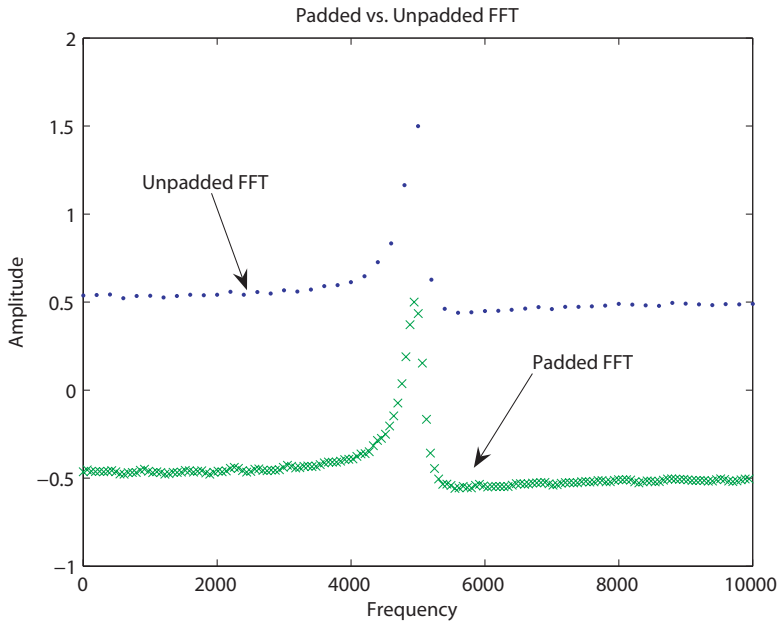

Figure 4.10: Δf compression can enable resolution of narrow peaks that would be invisible in the transform of an un-padded time signal.

considered corrupted and simply excluded. When fitting an FFT to determine an amplitude value, uncertainty information was generated by first assigning the error on each FFT data point to be equal to the RMS value of the FFT data in a 1000 point range several kilohertz away from the peak. The same fit was then performed again, with the error on each point set equal the the initial error value multiplied by the square root of the reduced chi-squared ($\chi^2_\nu = \frac{1}{N_{DOF}} \sum \frac{(y_{fit}-y_i)^2}{\sigma^2}$) of the first fit. The result was an error on the amplitude A that better described the statistical behavior of the data [62].

As addressed in section 4.2, the polarization amplitude was proportional to:

$$A = \sin(\theta_{tip}) \times P \times \text{constant factors.} \tag{4.20}$$

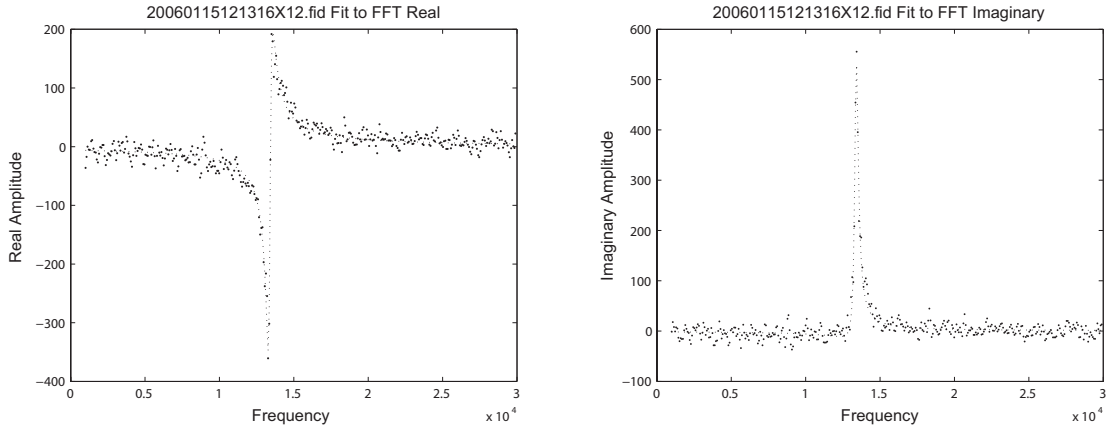

Figure 4.11: Real & Imaginary FFTs and Fits.

Also as discussed, each tip incurred a loss in polarization as determined by

$$P_{post-tip} = \cos(\theta) P_{pre-tip} \tag{4.21}$$

such that the signal A_n detected after the nth tip, disregarding T_1 decay, was

$$A_n = A_0 \sin(\theta_{tip}) \cos^{n-1}(\theta_{tip}). \tag{4.22}$$

If not accounted for, tip-induced loss would result in the measurement of an artificially shortened lifetime. This effect is illustrated in Fig. 4.13. Consequently, it was necessary to determine the magnitude of the loss effect in order to appropriately compensate for it - this resulted in the adoption of a major structural procedure in the lifetime measurement: the "tiptest", a series of 5 FID acquisitions in very close temporal proximity, typically 3 seconds or less (timing was restricted by the operational speed of the DAQ program and scope-to-computer data transfer). An example of the

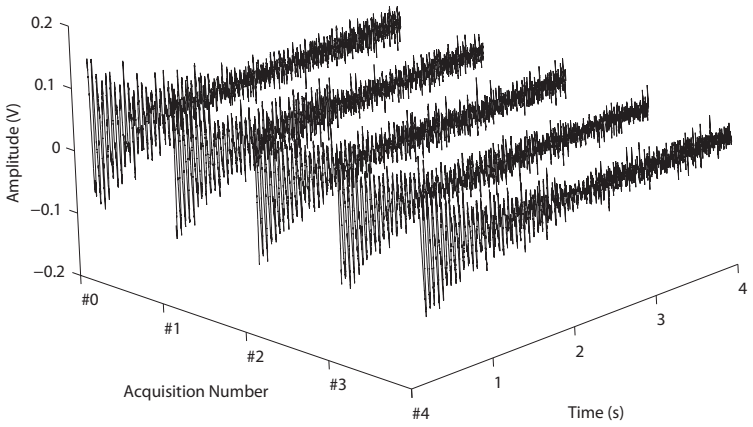

Figure 4.12: 5 Tiptest Acquisitions, Cell X12, Temperature = 298 K, f_{Larmor} = 970 KHz. Loss/pulse = 2.86%

5 tiptest acquisitions can bee seen in Fig. 4.12. Except in the case of extremely short T_1 values, the rapid pulsing allowed the natural T_1 decay to be considered irrelevant, with all the polarization loss attributed to tip loss. An exponential decay was fitted to the data (ordinate: amplitude; abscissa: pulse number), with the decay constant related to the tip angle as follows:

$$\theta_{\text{tip}} = \cos^{-1} e^{1*\alpha}, \tag{4.23}$$

where α is the tip decay constant given in units $(pulse^{-1})$.

Incorporating T_1 decay, this became:

$$A_n = A_0 \sin(\theta_{\text{tip}}) \cos^n(\theta_{\text{tip}}) e^{n\Delta t/T_1}, \tag{4.24}$$

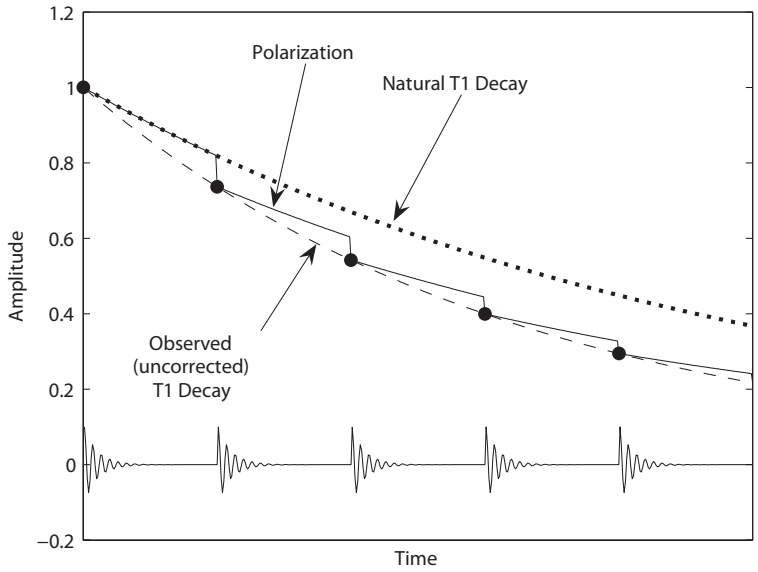

Figure 4.13: Artificial shortening of the sample lifetime by tip-induced polarization loss.

where n is the pulse number, Δt is the spindown pulse interval, and T_1 is the quantity we were trying to measure.

Pursuant to the tiptest, the "spindown" sequence was a set of four additional FID acquisitions separated in time by a value approximately equal to the anticipated value of $T_1/2$. Using the last tiptest point as the first spindown point, the nine total FIDs could be employed as two sets of 5 FIDs each. This scheme fell in line with the overarching desire to minimize the number of points taken (to minimize signal lost due to tipping) while still allowing sufficient statistics for meaningful analysis. An example of the signals acquired during a spindown test is given in Fig. 4.14, and a visual representation of the translation between frequency-space data and polarization decay is given in Fig. 4.15.

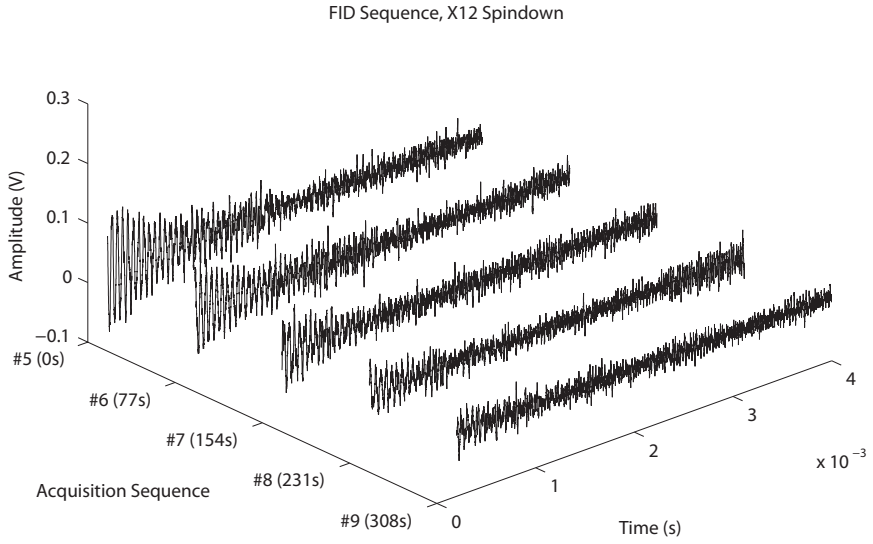

Figure 4.14: 5 Spindown Acquisitions, Cell X12, Temperature = 298 K, f_{Larmor} = 970 KHz. $T_1 = 475$ s

Following the tiptest-spindown sequence, two rates can be extracted from the data: α, the tip decay constant, and $1/T_{1u}$, the uncorrected longitudinal polarization decay constant. To compensate for tip loss, we make use of the following relationship between the raw decay and the tip-loss corrected decay:

$$e^{n\Delta t/T_{1u}} = e^{n\alpha} e^{n\Delta t/T_1}, \tag{4.25}$$

where T_{1u} is the uncorrected longitudinal decay rate and $e^{n\alpha} = \cos^n(\theta_{\text{tip}})$.

The correction is thus:

$$1/T_1 = 1/T_{1u} - \alpha/\Delta t. \tag{4.26}$$

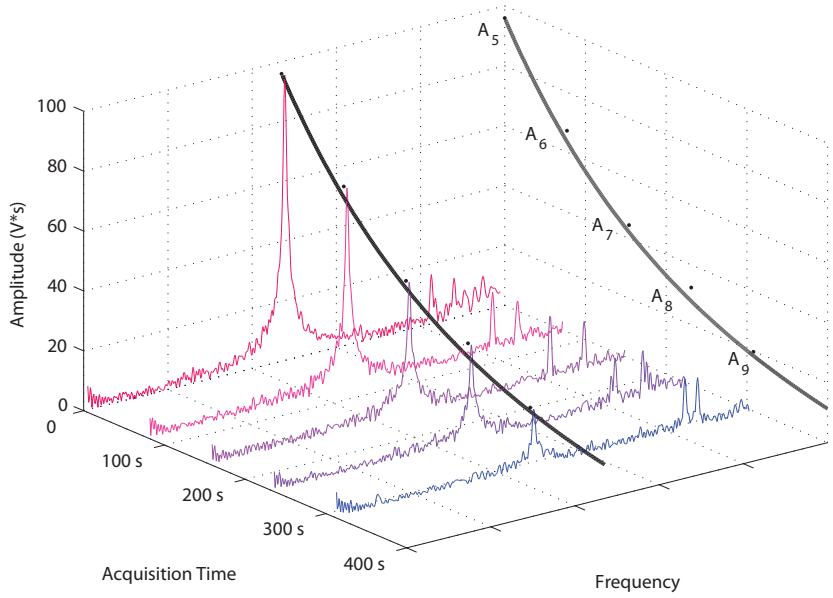

Figure 4.15: Decay rate can be extracted from a fit to FFT amplitude vs. time. For each FID in the spindown sequence (FIDs # 5 through # 9) the amplitude A was determined from the fit to eqn. 4.19. The resulting amplitudes A_5 through A_9 were rescaled by a common factor in order to make A_5 visually coincide with the maximum of the first transform. The FFTs shown are the $\phi = 0$ components of eqn. 4.19 for each acquisition. The dark line is an exponential fit to amplitudes A_5 through A_9.

It can clearly be seen that increasing the interval between spindown pulses reduces the necessary correction factor, as does minimizing α (or reducing tip angle). These advantages are offset by the practical concern of obtaining enough *SNR* to reliably extract amplitudes, necessitating sufficiently large tip angles and short enough spindown intervals that the final pulse retains *SNR*>1.

The uncertainty on each individual spindown value was expected to obey statistical behavior, owing to the statistical nature of the amplitude fits. Consequently, the error on individual $1/\mathrm{T}_1$ values was considered an accurate accounting of how well an individual spindown was understood. We saw evidence, however, that the measured value of $\frac{1}{T_1}$ for a given temperature and magnetic field value sometimes changed from run to run beyond what would be expected from statistics alone. This was not unexpected. Wu and collaborators, when studying quadrupole surface interactions of Xe-131 with RbH surfaces also saw changes when the cell was subjected to hear from a hand torch (which was used in part to move around Rb in the cell). We were quite careful to not subject our samples to harsh conditions, and found the variability of $\frac{1}{T_1}$ to be relatively small. Still, we added an error (typically on the order of 0.1 mHz) to each measurement of $\frac{1}{T_1}$ at a given set of conditions so that the χ^2_ν for an average of the points was equal to one. Typically three relaxation rate measurements made up a field/temperature point.

We note finally that the analysis of the dependence of $\frac{1}{T_1}$ on magnetic field and temperature will be presented in Chapter 5.

4.8 Sample Preparation

Samples consisted variously of 2 cm and 2.54 cm diameter cells, fashioned from Pyrex by UVA Chemistry Department glassblower Willie Shoup. They were filled on a laboratory gas handling system that provided the capability to evacuate and "bake out" a glass manifold with several cells attached, and subsequently fill them with measured quantites of various gases.

Following delivery from Willie, cells were attached to a hollow glass tube (the "string"). The string itself was connected to the gas system with a glass-metal seal, and had a hollow retort on the end opposite the seal for holding an alkali metal ampoule. After attaching the cells to the string and the string to the gas system, an ampoule of scientific-grade purity rubidium was placed in the retort. With the retort then sealed off from atmospheric air, the string and cells were evacuated to $\sim 10^{-7}$ torr. A conformal oven was placed around the string and cells, which were baked at 200C for several days in order to drive off surface contaminants above and beyond the cleaning ability of chemical scouring treatments.

Pursuant to surface cleaning, rubidium metal was chased with a flame and distilled into the cells. Filling of each cell took place individually. Scientific-grade purity xenon (natural abundance or enriched ^{129}Xe) was frozen into the cell by submerging the cell in liquid nitrogen and allowing xenon to freeze into it with sufficient quantity to result in the desired final pressure of xenon (given in table 4.3) at room temperature. Scientific-grade hydrogen and nitrogen were charged into intermediate volumes and

allowed to mix for an hour before being opened to the cell. Upon opening of the string valve, a large fraction (by atom number) of the mixed gases were chilled into the cell by the continuing presence of the liquid nitrogen bath around the cell. Once the gases had been given adequate time to chill into the cell, the connection between the cell and the string was melted by an applied flame, closed by the relative vacuum inside the string, and the cell pulled off the string. This procedure was repeated for each cell on the string, with final gas pressures given in table 4.3.

Table 4.3: High Pressure Xenon Cell Contents

Cell Name	Diam.	Xe Pressure	N_2 Pressure	H_2 Pressure
X9	1”	7.5atm	200 torr	0 torr
X12	1”	7.5atm	200 torr	20 torr
D1	1”	7.5atm (enriched)	200 torr	80 torr
D3	1”	7.5atm (enriched)	200 torr	20 torr
D5	1”	7.5atm (enriched)	200 torr	0 torr
X13	2cm	7.5atm (enriched)	200 torr	0 torr
X14	2cm	7.5atm (enriched)	200 torr	25.4 torr
X15	2cm	7.5atm (enriched)	200 torr	50.8 torr
X16	2cm	7.5atm (enriched)	200 torr	101.6 torr

After filling, the internal rubidium hydride surfaces were prepared following the procedure established by Mabuchi [33], placing the cells in an oven at 80 C and allowing them to bake for two weeks. Mabuchi confirmed the presence of RbH in his cells by the observation of a milky-white coating over the inside surface of those of his cells that were charged with a particularly high pressure of hydrogen.

Chapter 5

Results and Analysis

5.1 Magnetic Decoupling Data

In view of the predictions of the theory discussed in chapter two, we endeavored to study spin relaxation on pyrex glass partially covered in rubidium hydride and rubidium deuteride. To that end, we measured relaxation rates as a function of magnetic field from .044 T to approximately 1 T for each of four samples and between two to seven different temperatures. Spin relaxation was also measured at a large number of temperatures between 205 K and 323 K at a single magnetic field of 0.0824 T, where decoupling was largely absent. In total, over 1000 measurements of spin relaxation times were performed. The data are summarized in figs. 5.1 through 5.4, in which each plot shows the measured relaxation rate for a given sample as a function of both magnetic field and temperature. Relaxation rate as a function of temperature alone was also measured for a fifth sample (designated X16) and is shown in figure 5.16.

5.2 Initial Observations

5.2.1 Omnipresence of Magnetic Decoupling

As is visually apparent in figs. 5.1-5.4, the first and most striking conclusion that we reach is that for all cells except the control cell, magnetic decoupling of the relaxation rate was clearly present at all temperatures. In every measurement of relaxation rate vs. magnetic field in cells X12, D1 and D3, the relaxation rate at low field is markedly

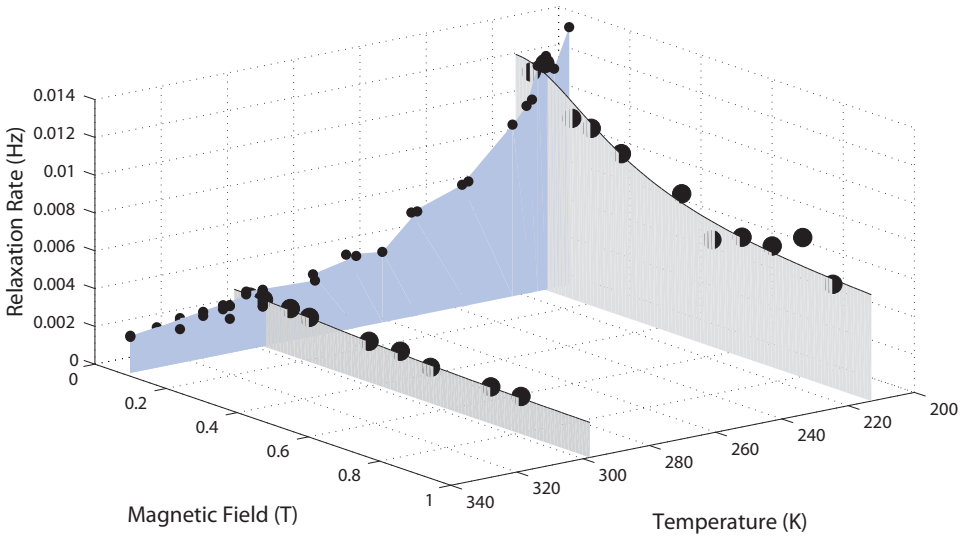

Figure 5.1: The measured spin relaxation rate as a function of both temperature and magnetic field is shown for the sample designated X9, which contained no hydrogen or deuterium and served as a control.

higher than the relaxation rates at the higher fields. Qualitatively, the shape of the magnetic decoupling curve is in excellent agreement with the expectation that the wall relaxation is being caused by randomly fluctuating magnetic fields that are well characterized by one or more correlation times. We note that even the magnetic decoupling shown in Fig. 5.2 above ∼250 K is visually quite pronounced, as illustrated for one of the temperatures by the inset. We also note that our fairly comprehensive study is consistent with the observations of apparent magnetic decoupling by Mabuchi [33].

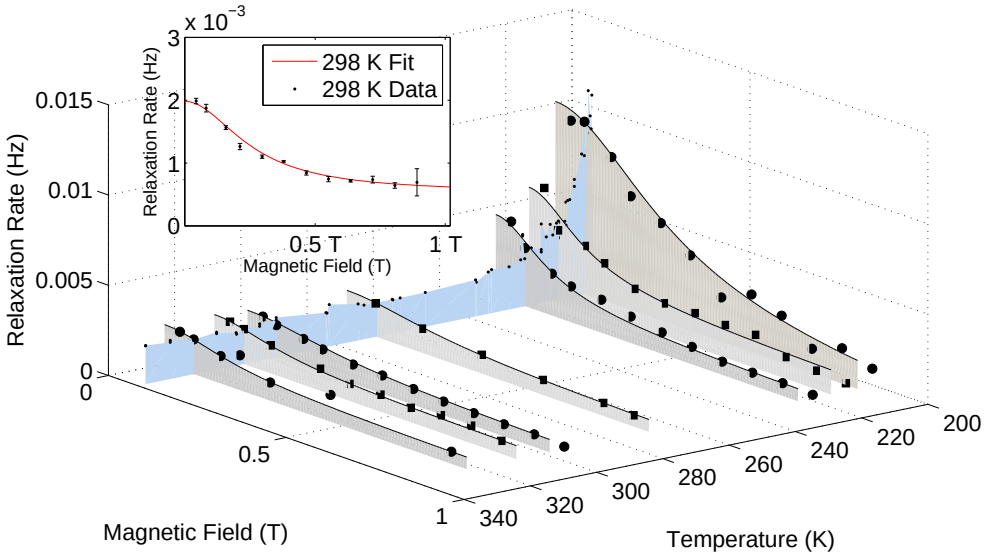

Figure 5.2: The measured spin relaxation rate as a function of both temperature and magnetic field is shown for the sample designated X12, which was 1" in diameter and contained 20 torr of hydrogen.

5.2.2 Isotopic Differences

Also made clear by the comparison of the X12 data (figs. 5.2 and 5.5) with the D1 and D3 data (figs. 5.3,5.6,5.4,5.7) is the qualitative difference between cells filled with different isotopes of hydrogen. X12, filled with a partial pressure of hydrogen, exhibits a significant rise in relaxation rate at low temperature and field. The relaxation rate of cell X16, also filled with hydrogen, similarly rises dramatically at low temperature. Cells D1 and D3, filled with partial pressures of deuterium, each exhibit low temperature (below 250 K) behavior that is reasonably similar to high temperature (above 250 K) behavior. The implication is that the qualitative differences observed between cells X12 and X16 and cells D1 and D3 stem from the substitution of hydrogen for deuterium.

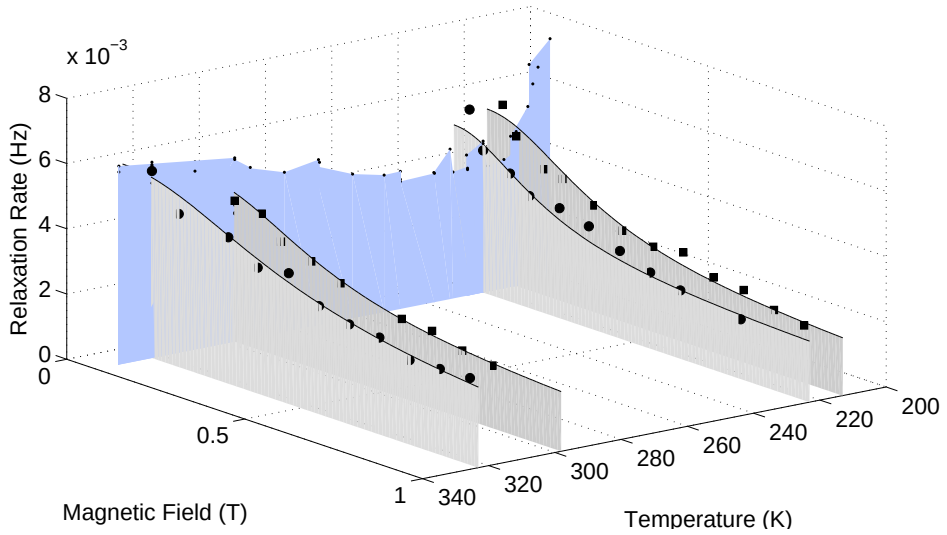

Figure 5.3: The measured spin relaxation rate as a function of both temperature and magnetic field is shown for the sample designated D1, which was 1" in diameter and contained 80 torr of deuterium.

If we are to attribute the low-temperature differences between the X- and D- cells to the isotopic differences in the cell composition, then it is significant that substantial relaxation can still be observed upon substitution of deuterium for hydrogen. Examining eqn. 2.51 [34](reproduced here for convenience)

$$\frac{1}{T_0} = \frac{4}{3}\frac{f(T)\gamma_K^2\gamma_S^2\hbar^2 S(S+1)\tau_c}{r^6}, \tag{5.1}$$

it can be seen that after normalization of eqn. 5.1 for $f(T)$, r^{-6} and τ_c, the relaxation rate of ^{129}Xe due to interaction with hydrogen should be approximately 16 times that

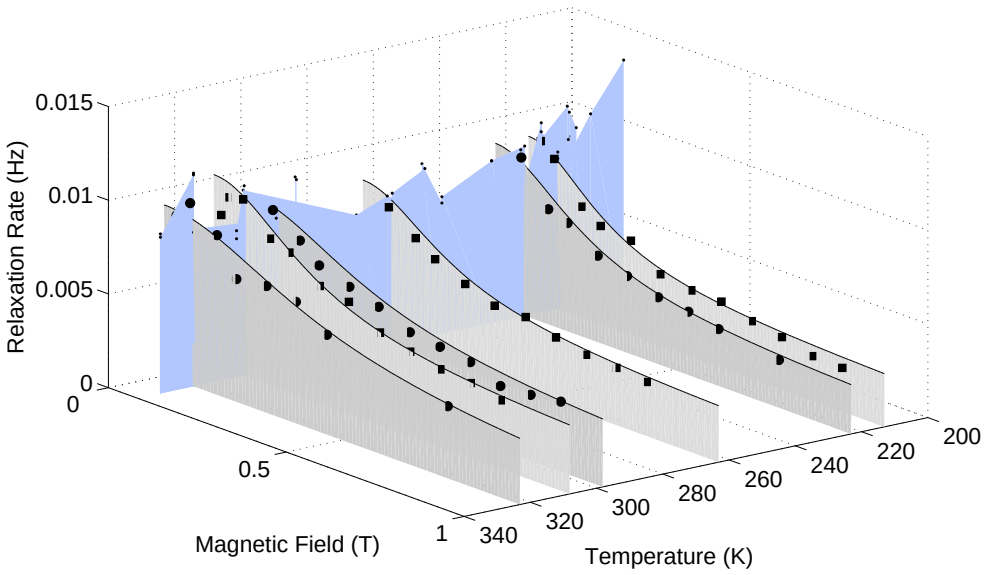

Figure 5.4: The measured spin relaxation rate as a function of both temperature and magnetic field is shown for the sample designated D3, which was 1" in diameter and contained 20 torr of deuterium.

due to interaction with deuterium:

$$\frac{1}{T_1}^{Xe-H} \propto S_H(S_H{+}1)(\gamma_{Xe}\gamma_H\hbar)^2 = \frac{S_H(S_H+1)}{S_D(S_D+1)}\left(\frac{\gamma_H}{\gamma_D}\right)^2 S_D(S_D{+}1)(\gamma_{Xe}\gamma_D\hbar)^2 \approx 16\frac{1}{T_1}^{Xe-D} \tag{5.2}$$

where γ_H and γ_D are the hydrogen and deuterium gyromagnetic ratios, and S_H and S_D are their spin quantum numbers (1/2 and 1, respectively). At temperatures above roughly 250 K, however, we see that the relaxation in deuterium cells is actually around four times greater than what was observed in the hydrogen cells. This is in sharp contrast to the expectation from eqn. 5.2 that relaxation should be roughly 16 times smaller in deuterium cells. The implication is that the nuclear spins are not the predominant source of relaxation at temperatures above 250 K. If we assume instead that above 250 K the source of relaxation is due to paramagnetic sites, there is no

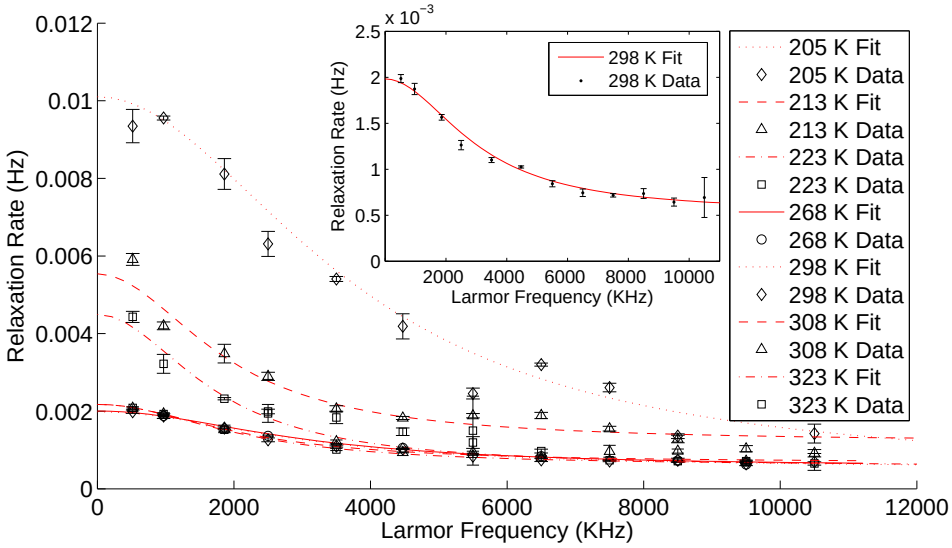

Figure 5.5: X12 Decoupling Curves, All Measured Temperatures

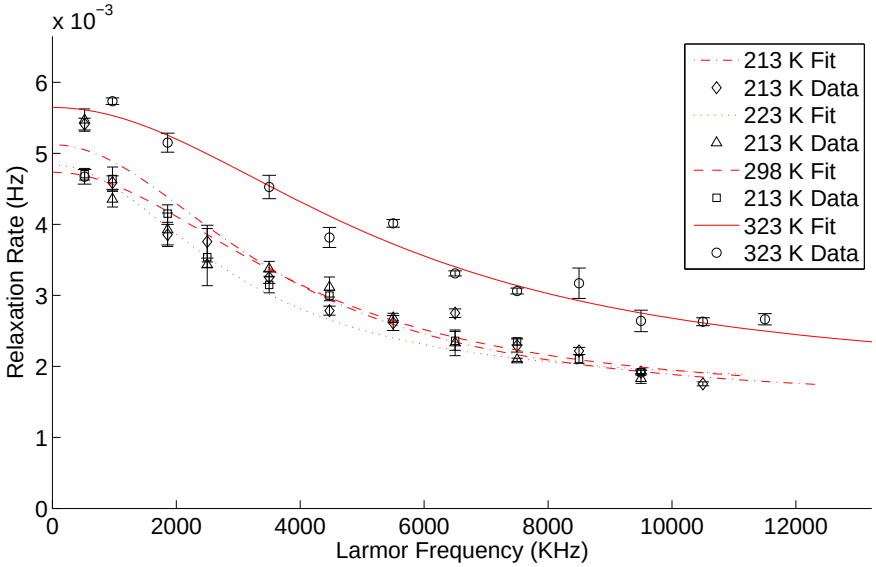

Figure 5.6: D1 Decoupling Curves, All Measured Temperatures

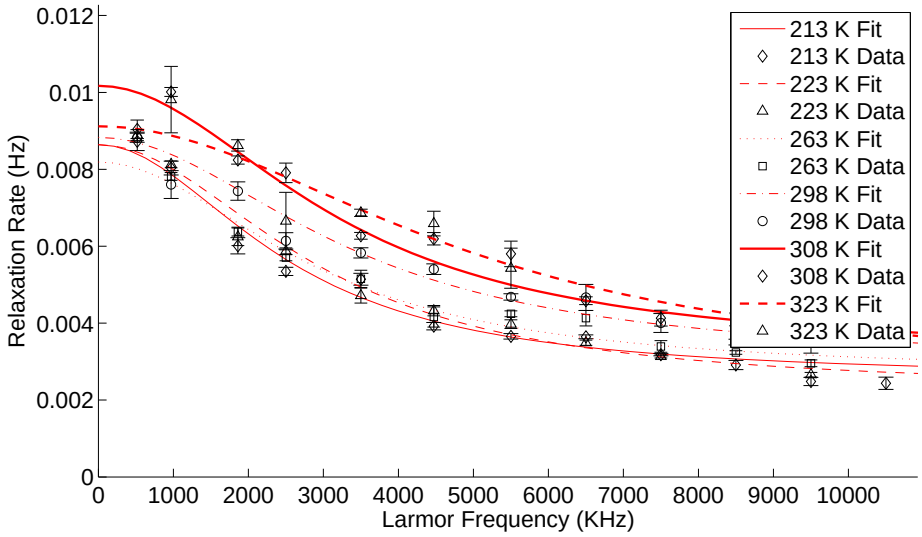

Figure 5.7: D3 Decoupling Curves, All Measured Temperatures

discrepancy. The fact that the deuterium cells exhibited faster relaxation that the hydrogen cells can be attributed to a somewhat higher concentration of paramagnetic sites.

5.2.3 Decoupling Widths Using a Simple Single Lorentzian Model

Initially, the analysis of decoupling data was based on fitting the data with a single Lorentzian plus a constant offset. In this way it was possible to get a quick quantitative snapshot of the overall trends we were observing. The fitting equation was thus:

$$\frac{1}{T_1} = \frac{\Gamma_0}{1 + B^2/\Delta B^2} + \Gamma_B, \tag{5.3}$$

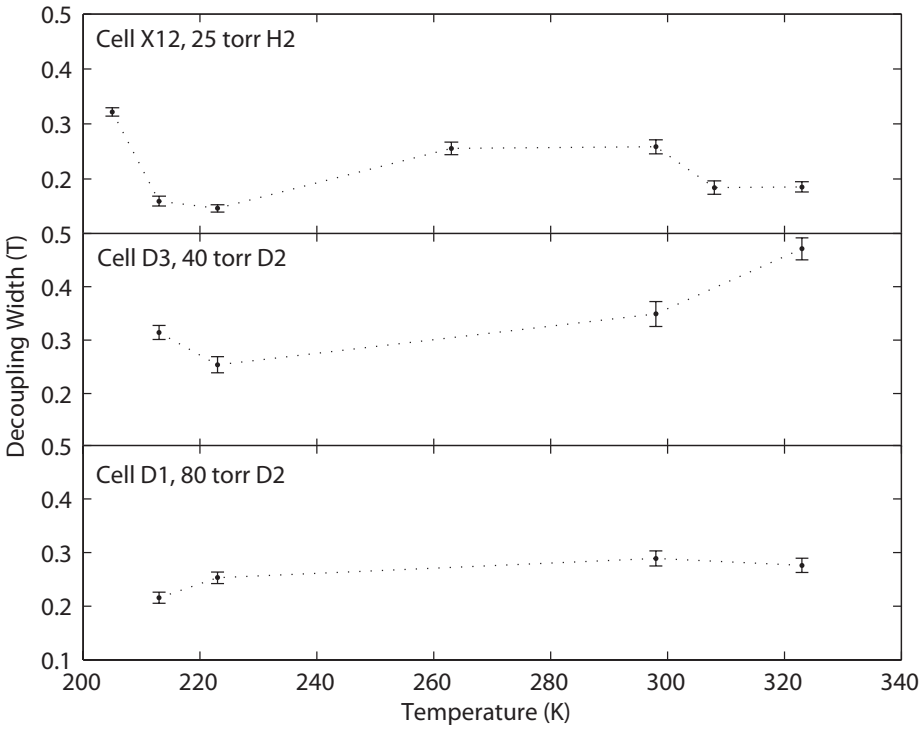

Figure 5.8: Temperature Variation of Decoupling Widths, Cells X12, D3, D1

where Γ_0 is the zero-field relaxation rate, ΔB is the decoupling width, and Γ_B is a constant, background rate. It is this function that is used for the decoupling fits shown in figures 1-7, and it was this curve that provided all the initial information on the decoupling widths. The fitted values of ΔB for cells X12, D1 and D3 are shown in Fig. 5.8 as a function of temperature. Following eqn. 2.22, the decoupling width is given by the frequency at which $(\omega^{(q)}\tau_c)^2 = 1$, providing:

$$\Delta B = \frac{1}{2\pi\gamma B\tau_c}, \tag{5.4}$$

where γ is the gyromagnetic ratio of the spin in question, and τ_c is the correlation time associated with the random motion of a spin. From eqn. 5.4, it is clear that assumptions regarding the identity of the relaxing spin, together with its gyromagnetic ratio, will strongly affect the interpreted value of the correlation time that will be deduced from an observed decouplind width ΔB. We found guidance on the appropriate choice of gyromagnetic ratio for interpreting high-temperature decoupling width data in the analysis of the other fit parameters of eqn. 5.3. By plotting the fitted values of Γ_B divided by $\Gamma_0 + \Gamma_B$ (Fig. 5.9), it could be seen that resulting values for all three cells approached 0.3 at high temperatures (table 5.4). Significantly, this value was seen to be roughly independent of decoupling width, as illustrated by Fig. 5.10. This is precisely the behavior we expect if the source of relaxation is pramagnetic sites.l In this case $\omega_S \gg \omega_K$, and for the fields at which we worked the quantity in eqn. 5.5 in brackets reduces to $\frac{7}{1+(\omega_S\tau_c)^2} + 3$. Furthermore, as is shown in Fig. 5.10, the ratio of $\frac{\Gamma_B}{\Gamma_B+\Gamma_0}$ is also independent of the fitted values of ΔB. Again, this is expected for relaxation due to paramagnetic sites but not necessarily of the relaxation is due, for instance, to dipolar coupling to surface nuclear spins.

$$\frac{1}{T_1} = \frac{1}{10T_0}[\frac{1}{1+(\omega_K-\omega_S)^2\tau_c^2} + \frac{3}{1+(\omega_K)^2\tau_c^2} + \frac{6}{1+(\omega_K+\omega_S)^2\tau_c^2}], \qquad (5.5)$$

If interaction with paramagnetic sites is indeed the mechanism responsible for high-temperature relaxation, the resulting correlation times for all cells and temperatures are those listed in table 5.3. Given a 22 ps correlation time, an illustration of

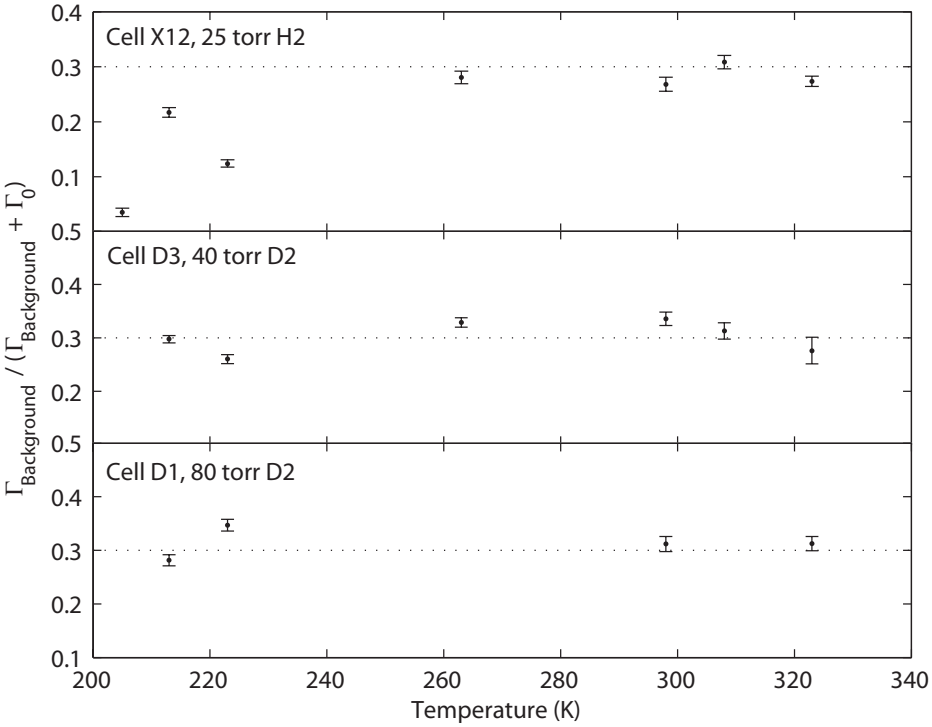

Figure 5.9: $\frac{\Gamma_{Wall}}{\Gamma_{Wall}+\Gamma_{Other}}$, All Cells and Temperatures

Table 5.4: X12 $\Gamma_B/(\Gamma_0 + \Gamma_B)$

$T(K)$	X12	D3	D1
205	0.0352 ± 0.0585	N/A	N/A
213	0.2169 ± 0.0364	0.2974 ± 0.0219	0.2814 ± 0.0322
223	0.1242 ± 0.0074	0.2578 ± 0.0232	0.2991 ± 0.0335
263	0.2889 ± 0.0343	0.3241 ± 0.0199	N/A
298	0.2650 ± 0.0254	0.3504 ± 0.0429	0.3194 ± 0.0532
308	0.3179 ± 0.0287	0.3067 ± 0.0572	N/A
323	0.2619 ± 0.0179	0.2991 ± 0.0374	0.3478 ± 0.1073

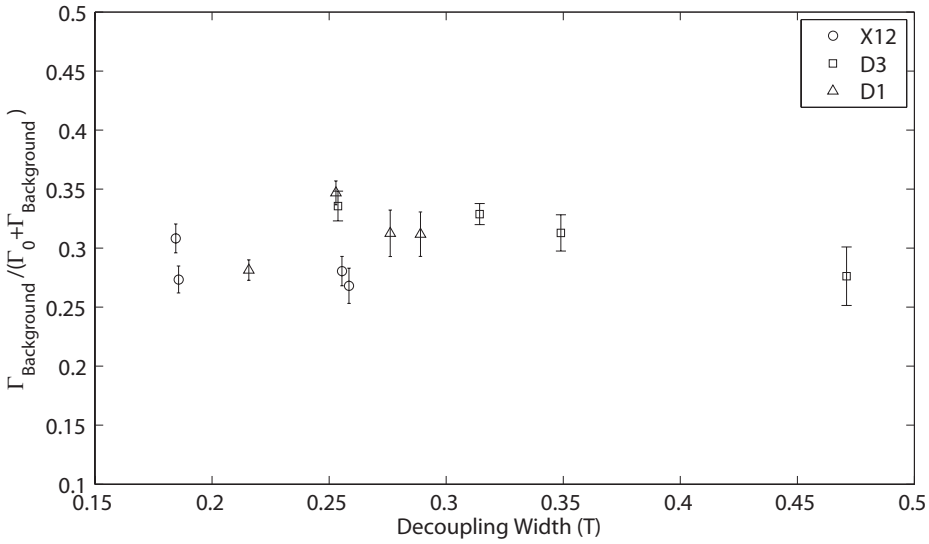

Figure 5.10: $\frac{\Gamma_{Wall}}{\Gamma_{Wall}+\Gamma_{Other}}$ vs. Decoupling Width, All Cells and Temperatures

the behavior expected from eqn. 5.5 can be seen in figure 5.11.

To summarize this first stage of the analysis, several important points should be made. First, the paramagnetic model is remarkably consistent with the data at temperatures above 250 K, as demonstrated by the ratios of background rate to low field rate. This ratio also does not vary substantially with ΔB, suggesting that the

Table 5.3: Correlation times from single Lorentzian + constant offset, paramagnetic interpretation

	X12		D3		D1	
	τ_c (ps)	$\sqrt{\chi^2_\nu}$	τ_c (ps)	$\sqrt{\chi^2_\nu}$	τ_c(ps)	$\sqrt{\chi^2_\nu}$
205 K	17.6 ± 2.3	5.49				
213 K	41.7 ± 10.5	4.19	26.3 ± 3.97	3.14	18.1 ± 2.78	3.71
223 K	38.7 ± 4.48	2.61	25.5 ± 1.73	2.7	22.3 ± 4.48	3.31
263 K	22.2 ± 2.61	2.75	22.2 ± 1.53	2.24		
298 K	22 ± 1.84	1.70	20.4 ± 1.52	3.41	15.5 ± 1.73	2.83
308 K	30.8 ± 4.38	2.34	17.5 ± 2.10	3.72		
323 K	30.6 ± 2.41	1.57	13.4 ± 1.32	1.51	12.0 ± 2.66	5.45

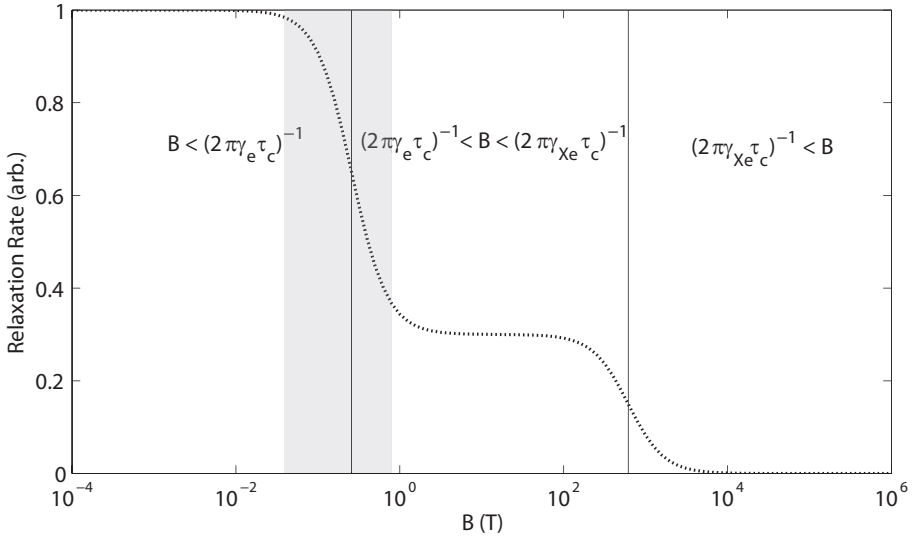

Figure 5.11: Modeled field dependency of relaxation rate for xenon-paramagnetic relaxation, demonstrating the separation of the second Lorentzian component of eqn. 5.1 from the first and third components.

ratio is not correlated with decoupling width value. Secondly, there is no obvious trend of ΔB that would suggest isotopic differences. Thirdly, while either paramagnetic or nuclear interaction would result in magnetic decoupling (as will be discussed more later), the assumption that decoupling arises due to interaction with nuclear spins leads to correlation times that are significantly longer than one would expect. With all of this said, the strongest evidence presented so far that paramagnetic sites are responsible for relaxation is not the magnetic decoupling widths, but rather the fact that relaxation persists (and is even stronger!) in our cells containing deuterium instead of hydrogen.

5.2.4 Correlation Time Analysis

While the consistency of $\frac{\Gamma_B}{\Gamma_0+\Gamma_B}$ with 0.3 is compelling evidence that relaxation at high temperatures is paramagnetic in nature, it is by no means unassailable. The choice of γ_e in eqn. 5.4 points to correlation times on the order of tens of picoseconds for all three cells. This timescale is a reasonable estimate in view of the documented adsorption energy of xenon on rubidium and rubidium hydride surfaces (0.03 eV and 0.10 eV, respectively [64]). Frenkel's law gives an estimate of the amount of time an atom spends adsorbed onto a surface, referred to as the *dwell time*, τ_d:

$$\tau_d = \tau_0 e^{E_a/KT} \tag{5.6}$$

where $\tau_0 = 10^{-12}$ s, E_a is the adsorption energy, K is Boltzmann's constant, and T is the temperature. For temperatures from 250 K to 323 K, Frenkel's law implies correlation times on the order of 10-100 ps. In light of the predictions of Frenkel's law and the approximate nature of our estimate for τ_0, relaxation involving paramagnetic sites appears to be quite consistent with out observations. For interaction timescales to directly follow Frenkel's law, however, would be to imply that simple adsorption is the dominant mechanism governing the motion of the atom relative to the surface. Driehuys' studies of xenon relaxation on surfasil coatings [34] showed that surface interaction can be more complex than simple adsorption. In the case of surfasil relaxation, surface interaction timescales were found to be as long as microseconds. While the polymeric structure of the siliconized inner surfaces of Driehuys' cells were

almost certainly more intricate than the rubidium-hydride surfaces studied here, it raises the possibility that surface trapping could hold xenon atoms far longer than simple adsorption would permit. If this trapping resulted in timescales as long as nanoseconds, a possibility that would be surprising but perhaps not impossible, it would enable xenon relaxation due to interaction with hydrogen or deuterium atoms in the surface coating.

5.2.5 Decoupling Fits Using the Full Three-Lorentzian Fitting Function

Given the possibility that relaxation is due to nuclear interactions, it made sense to modify the fit function to more properly account for the different shape eqn. 5.1 would acquire if relaxation were due to xenon-nuclear interaction. An illustration of this shape, with a correlation time of 15 ns and clearly contrasting with the plot shown in Fig. 5.11, can be seen in Fig. 5.12. The single Lorentzian plus constant background fit performed earlier, interpreted in the context of paramagnetic interaction, will be referred to henceforth as the 1LPC fit. The more complex paramagnetic fit function, with three coupled Lorentzians, is displayed as eqn. 5.7 below, and will henceforth be referred to as 3LP:

$$\frac{1}{T_1} = A[\frac{1}{1+(2\pi B)^2(\gamma_e+\gamma_{Xe})^2\tau^2} + \frac{3}{1+(2\pi B)^2\gamma_{Xe}^2\tau^2} + \frac{6}{1+(2\pi B)^2(\gamma_e-\gamma_{Xe})^2\tau^2}]. \tag{5.7}$$

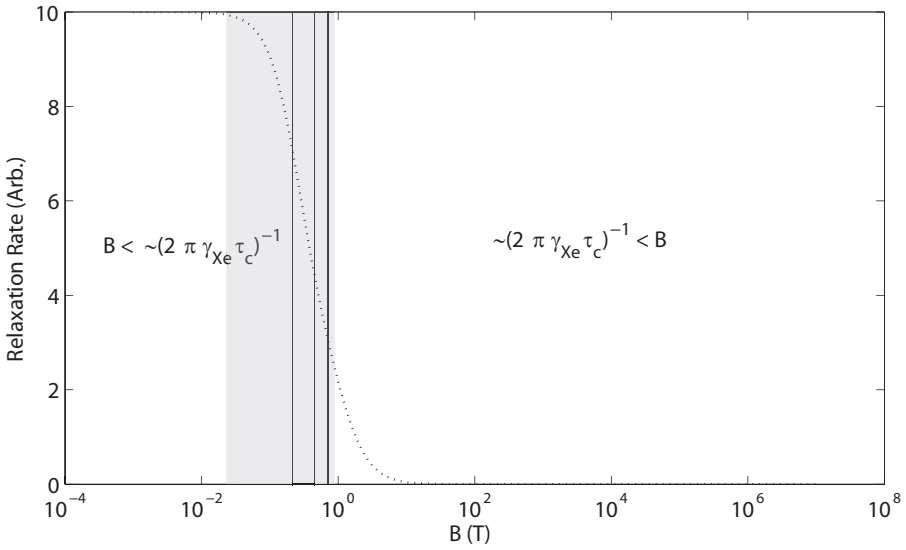

Figure 5.12: Modeled field dependency of relaxation rate for xenon-proton relaxation, demonstrating the near-indistinguishable overlap of the three Lorentzian components of eqn. 5.1.

Eqn. 5.7 has only two fit parameters: amplitude, A, and correlation time, τ_c. The fitted correlation times are listed in table 5.4. The correlation time errors shown in table 5.4 are rescaled errors - that is, the listed values are the product of the error output from the fit and $\sqrt{\chi^2_\nu}$. Rescaling the error in this fashion gives an indication of the uncertainty on fitted correlation times when the reduced-chi-squared of the fit is equal to one. The strong agreement with the correlation times listed in table 5.3, especially at high temperature, is significant in that it supports the initial choice of fit model as a single Lorentzian plus constant offset. The three coupled Lorentzian fit assuming relaxation due to nuclear spins is given by eqn. 5.8, and is referred to as

Table 5.4: Correlation times from three coupled Lorentzians, paramagnetic interpretation

	X12		D3		D1	
	τ_c (ps)	$\sqrt{\chi^2_\nu}$	τ_c (ps)	$\sqrt{\chi^2_\nu}$	τ_c(ps)	$\sqrt{\chi^2_\nu}$
205 K	33.7 ± 19.9	13.7				
213 K	40.3 ± 14.0	4.63	24.2 ± 3.51	3.03	18.4 ± 2.31	3.62
223 K	24.4 ± 2.71	9.60	23 ± 3.51	6.75	21 ± 4	3.64
263 K	23.2 ± 2.06	2.52	24.1 ± 1.19	1.21		
298 K	23.7 ± 1.77	1.77	18.3 ± 0.763	4.22	15.0 ± 0.856	2.94
308 K	29.7 ± 2.31	2.20	17.6 ± 0.954	2.27		
323 K	31.9 ± 2.78	1.78	13.5 ± 0.872	1.53	11.0 ± 0.955	5.22

Table 5.5: Correlation times from three coupled Lorentzians, nuclear interpretation

	X12		D3		D1	
	τ_c (ns)	$\sqrt{\chi^2_\nu}$	τ_c (ns)	$\sqrt{\chi^2_\nu}$	τ_c(ns)	$\sqrt{\chi^2_\nu}$
205 K	21.2 ± 1.2	5.07				
213 K	18.3 ± 3.42	6.07	39.4 ± 3.44	4.58	34.0 ± 2.34	4.48
223 K	20.0 ± 1.54	4.29	48.7 ± 3.41	8.03	33.9 ± 2.63	3.64
263 K	12.9 ± 1.23	5.69	36.8 ± 3.13	5.73		
298 K	14.7 ± 1.03	2.80	39.8 ± 2.28	8.27	32.0 ± 1.57	3.85
308 K	17.2 ± 1.46	5.35	37.1 ± 2.17	3.98		
323 K	15.9 ± 2.9	6.2	31.4 ± 1.59	1.83	27 ± 2.08	5.63

the 3LN fit:

$$\frac{1}{T_1} = A[\frac{1}{1+(2\pi B)^2(\gamma_N+\gamma_{Xe})^2\tau^2} + \frac{3}{1+(2\pi B)^2\gamma_{Xe}^2\tau^2} + \frac{6}{1+(2\pi B)^2(\gamma_N-\gamma_{Xe})^2\tau^2}]. \tag{5.8}$$

Again, the only fit parameters are A and τ_c. Here, γ_N specifies the gyromagnetic ratio of the nuclear species in question, being hydrogen in the case of cell X12 and deuterium in the case of cells D1 and D3.

Predictably, the correlation times resulting from nuclear fits (using xenon & hydrogen gyromagnetic ratios for RbH cell fits and xenon & deuterium gyromagnetic

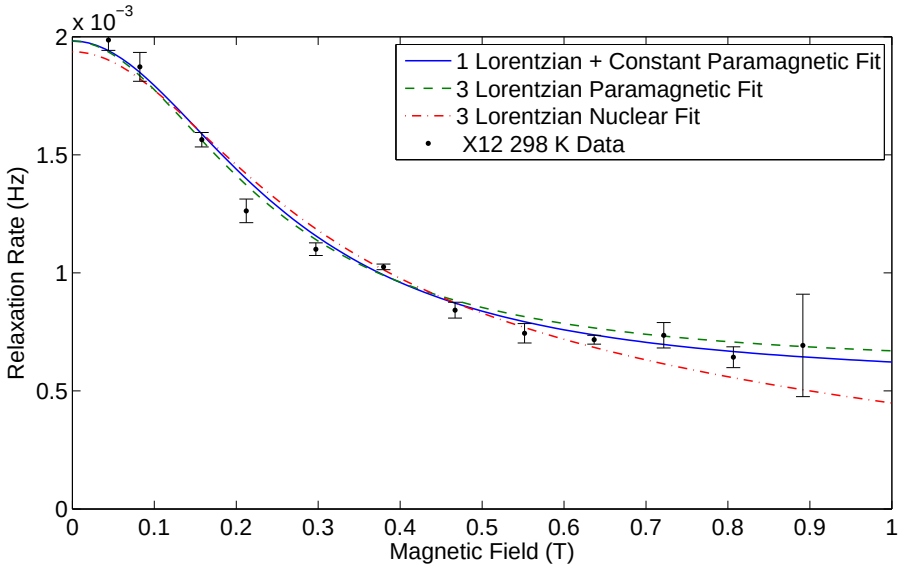

Figure 5.13: X12 RT data fit using 1LPC, 3LP, 3LN models

ratios for Rb-D cell fits) were found to be in the ten to twenty nanosecond range. The qualities of the fits when using the 3LN model at temperatures above 250 K were significantly poorer than the qualities of the fits when using the 3LP model, with the average reduced chi-squared value for the 3LN model 242% higher (at 27.42) than for the 3LP model (at 8.02) and 209% higher than the 1LPC model (at 8.89).

Despite differences in fit quality, it is apparent in Fig. 5.13 that over the bulk of the field range, the three different models behave fairly similarly. The distinction between the models becomes apparent at magnetic fields around 1.5 T, however, with the 3LP model asymptotically approaching a nonzero, "constant" rate while the 3LN model predicts a fast descent to zero high-field rate (this divergence is illustrated in Fig. 5.14). In figure 5.13 the χ^2_ν results discussed above are apparent, with the 3LN model diverging from the observed data as field is increased. It seems reasonable to

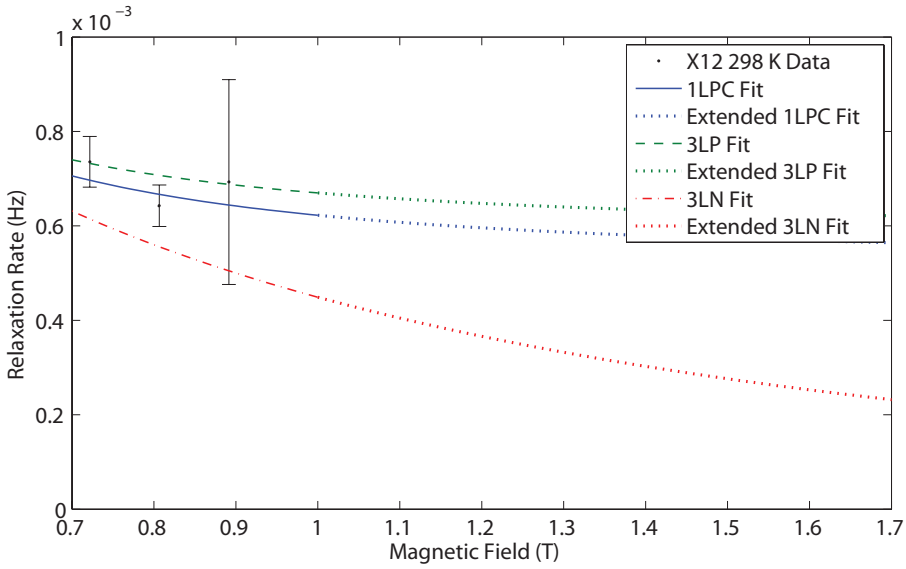

Figure 5.14: Extended fits for X12 RT data, displaying separation of modeled behavior with increased field value.

suspect that if data could have been taken at much higher field values, the discrepancies between the paramagnetic and nuclear models would have been sufficient to conclude the applicability of one model at the exclusion of the other from these fits alone. Unfortunately, the fact remains that the combination of high relaxation rate variability at a given field/temperature point and limited available field range place very real limits on the certainty with which either model can be asserted without considering additional results. The conclusion that can be drawn from the χ^2_ν information is that at high temperatures, the paramagnetic relaxation model is more likely to be an accurate interpretation than the nuclear relaxation model.

5.2.6 Relaxation Rate Temperature Dependence

A great deal can be learned by considering the temperature dependence of the spin relaxation. In eqn. 5.2, there are two quantites which can be expected to vary with temperature, $f(T)$ and τ_c. The fraction of atoms undergoing surface relaxation at any given time, $f(T)$, is almost certainly affected by adsorption onto cell walls. If the correlation time of the adsorbed atom's motion, τ_c, were determined by the amount of time the adsorbed atom spends on the surface, then the resulting temperature dependence of the relaxation rate including both the $f(T)$ dependence and the τ_d dependence would have the following form:

$$\frac{1}{T_1} \propto (e^{E_a/k_BT})^2 \propto e^{2E_a/k_BT}. \tag{5.9}$$

In Fig. 5.15, the temperature dependence of X9 can be seen to fit reasonably well to a function of the form of eqn. 5.9. The adsorption energy output from this fit can be seen to be $E_a = 0.044$ eV, a value close to previously reported measurements of the adsorption energy of xenon on Rb-saturated glass of 0.03 eV [64]. Using $E_a = 0.044$ eV, eqn. 5.9 indicates dwell times between 12 ps and 4 ps for temperatures between 200 K and 323 K, which in turn would result in decoupling widths of 0.4 T and 1.2 T, respectively. These values are roughly consistent with the decoupling curves presented in Fig. 5.1.

In the case of X12,X16, D1 and D3, the temperature dependence is quite different from what was seen in X9. For X12 and X16 (Fig. 5.16), the magnitude of the

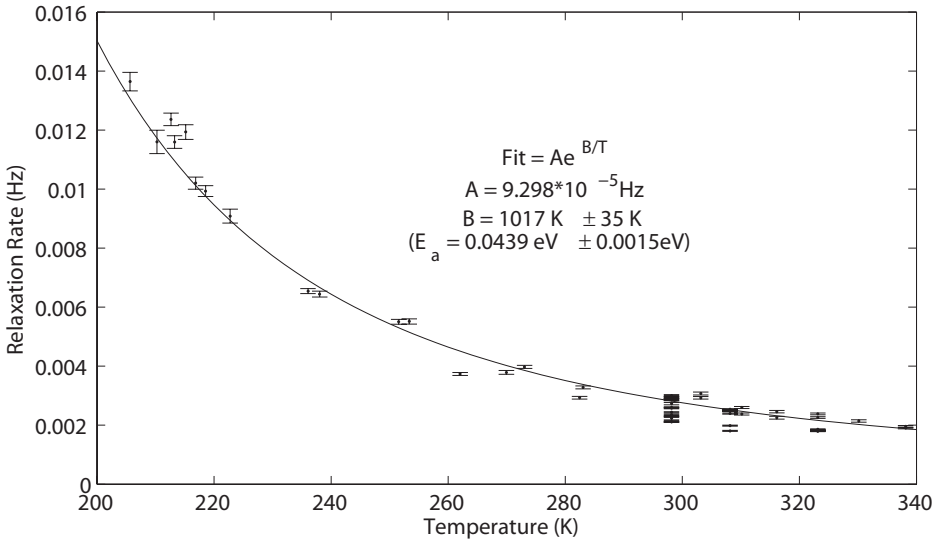

Figure 5.15: Cell X9, Relaxation Rate vs. Temperature at $F_{Larmor} = 970KHz$

spin relaxation is remarkably constant from around 250 K all the way up to 340 K. Furthermore, the magnetic decoupling width is also quite constant over this range. Assuming paramagnetic interaction, the correlation time calculated from decoupling widths is around 23 ps in this regime. As temperature is decreased below 250 K, the magnitude of the relaxation in cells X12 and X16 starts to increase sharply while the decoupling width continues to remain essentially constant. The implication seems to be that at temperatures above 250 K, τ_c has origins that are quite different from those contributing to $f(T)$. This interpretation is bolstered by the temperature variation behavior exhibited by cells D1 (Fig. 5.17) and D3 (Fig. 5.18), despite the absence in these cells of the large low-temperature rise observed in X12 and X16. The low temperature rise in cells X12 and X16 appears to exponentially increase with decreasing temperature, implying an adsorption energy E_a. Fits to the exponential increase

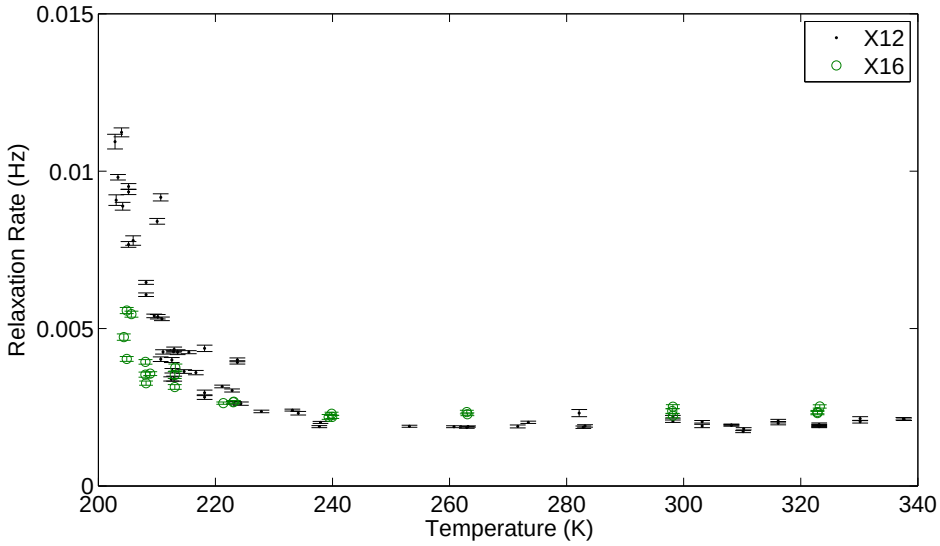

Figure 5.16: Cells X12 and X16, Relaxation Rate vs. Temperature at $F_{Larmor} = 970KHz$

above the constant baseline are displayed in figures 5.19 and 5.20. Data for cell D3 is too noisy to be effectively fitted, but cell D1 demonstrates behavior (Fig. 5.21) similar to X12 and X16 at temperatures below 250 K while exhibiting what could be interpreted as a different structure above 250 K. The adsorption energy values calculated from the exponential increase parameters for cells X9, X12, X16 and D1 shown in table 5.6.

Table 5.6: Adsorption energy

Cell	Fit Parameter B= $\frac{2E_a}{K}$	E_A(quad.)
X9	1017	0.0439 eV
X12	4769	0.2057 eV
X16	4600	0.1984 eV
D1	7675	0.3310 eV

It is possible that as temperature decreases, the relaxation rate increase visible

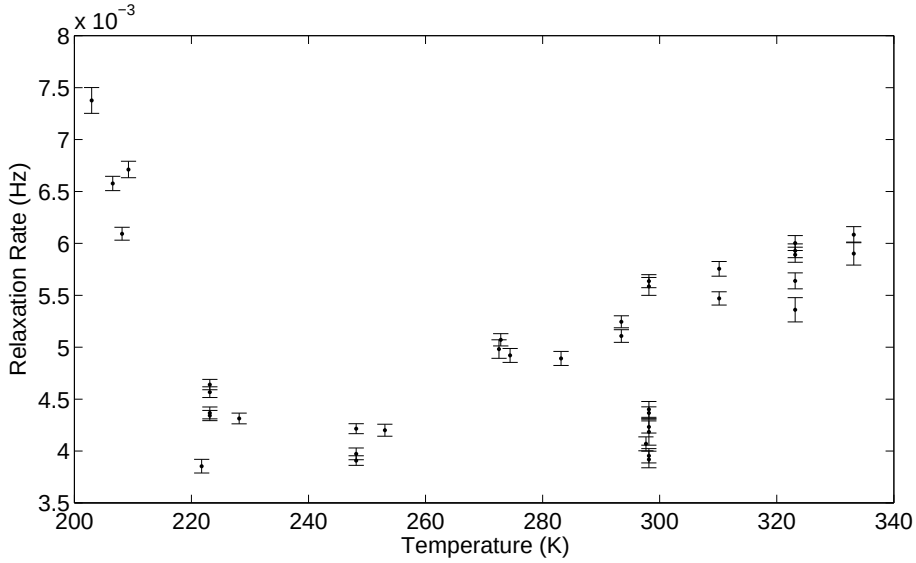

Figure 5.17: Cell D1, Relaxation Rate vs. Temperature at $F_{Larmor} = 970KHz$

in cells X12, X16 and D1 stems from the combination of an increasing nuclear interaction with the baseline paramagnetic interaction visible at high temperatures. This interpretation was suggested in section 5.2.2, but discrepancies arise when comparing the relative increases in relaxation rate at low temperature between hydrogen and deuterium cells. Eqn. 5.2 would suggest that the increase in relaxation rate over the baseline value for a hydrogen cell should be roughly 16 times the equivalent increase in a deuterium cell, while the measured increase is only a factor of roughly 4.5. A more nuanced interpretation might suggest that the paramagnetic contribution to the overall relaxation rate increases at low temperature similarly to the nuclear contribution, and in the case of a deuterium cell the paramagnetic component would be responsible for the bulk of the rate increase at low temperature.

An alternate interpretation for the low-temperature rise in relaxation rate in ru-

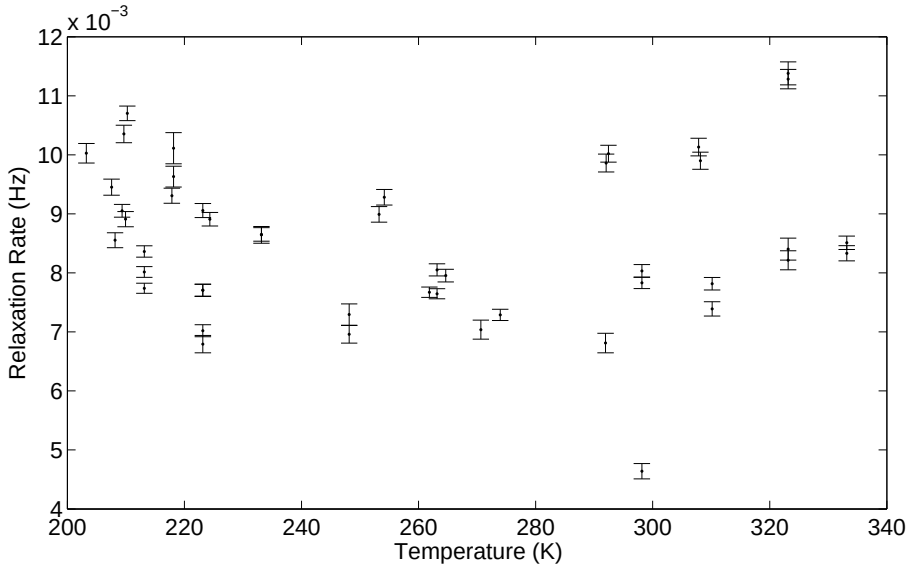

Figure 5.18: Cell D3, Relaxation Rate vs. Temperature at $F_{Larmor} = 970KHz$

bidium hydride cells is found in the very real possibility of incomplete involvement of the hydrogen charge in rubidium hydride formation. If a substantial fraction of the available hydrogen remained in the gas form, it could enable relaxation mechanisms that could rabidly depolarize the xenon gas. A more detailed discussion of proton-associated relaxation will be postponed until Appendix A, where it is more relevant to the cross-polarization work discussed there. There is, however, one intriguing potential relaxation mechanism stemming from the presence of molecular hydrogen that warrants mentioning here: Feldman and Sukhov [66] have investigated the formation of XeH_2 at temperatures below 70 K. These temperatures are far below the temperatures discussed in this work, and far below the freezing point of xenon. Theoretical work by Runeberg et al. [67] has predicted an activation energy of 0.03 eV for the formation of XeH_2 from neutral atoms, and activation energies at this

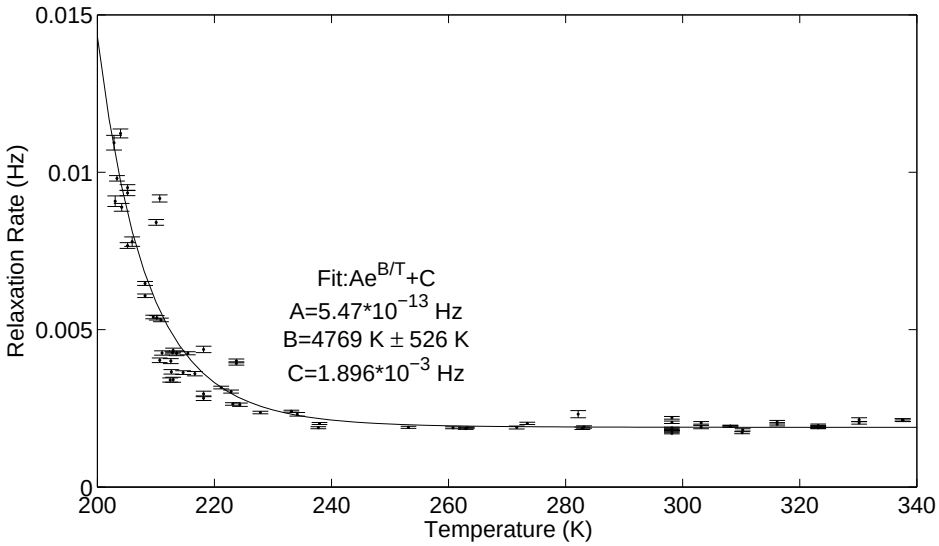

Figure 5.19: Cell X12, fit to all 970 KHz relaxation rate data.

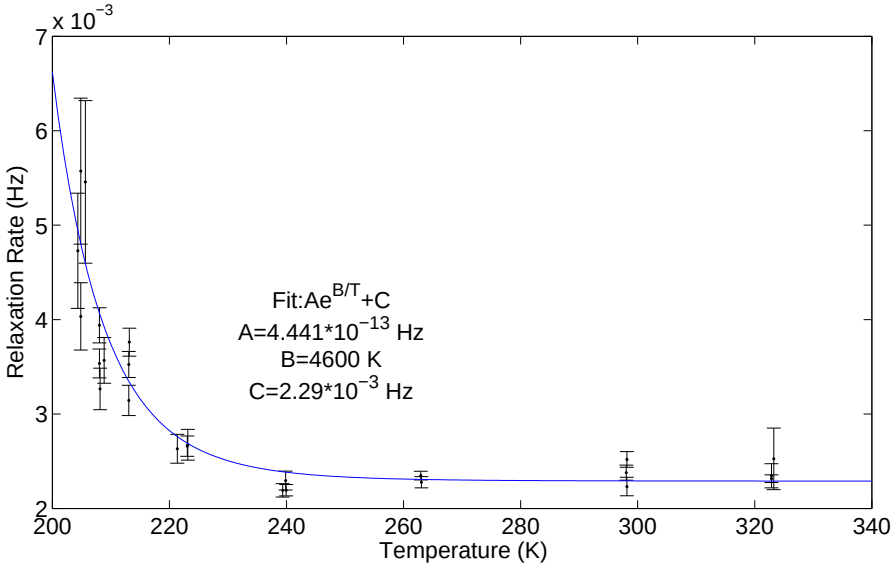

Figure 5.20: Cell X16, fit to all 970 KHz relaxation rate data.

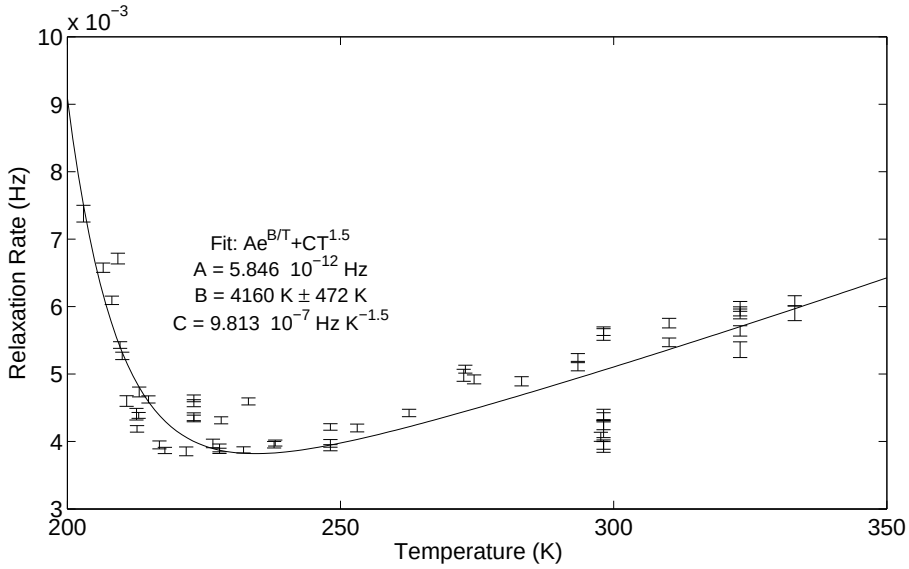

Figure 5.21: Cell D1, fit to relaxation rate data below 250 K

level have already been shown to be relevant at the temperatures involved in this work. Such an activation energy, however, would very nearly rule out dipolar relaxation on account of the correspondingly very short molecular lifetimes (on the order of 5 ps) that would result. Such an activation energy would not, however, rule out the spin-rotation and translation relaxation mechanisms available to the water-like molecule or even ^{129}Xe-Xe complexes [29]. Given the number of degrees of freedom available to such a molecule, it would not be surprising to find it to be a strongly relaxing compound. Nevertheless, the absence of comprehensive information regarding the formation and behavior of XeH_2 a the temperatures of this study would suggest that further discussion may be more speculative than illustrative, and the remaining conclusions to be drawn will stem from the analysis performed in the sections above.

A further modification, not exclusive to the isotopic distinction made between

RbH cell and RbD cell performance, is the postulation that at low temperatures the assumption of simple atom-surface adsorption breaks down. This could result in a modification to the autocorrelation function G_t describing the motion (eqn. 2.21), leading to a different density of states and frequency dependence as given by the Wiener-Khintchine theorem. In their work with entangled polymeric liquids, Ball et al. [68] address relaxation due to non-adsorptive molecular motion and evaluate the applicability of a non-exponential correlation function to the description of FID and solid echo amplitude behavior. In light of the relaxation behavior observed here at low-temperature, it would be imprudent to neglect the possibility that low-temperature xenon-surface dynamics are also non-adsorptive and would result in a different applicable autocorrelation function. It remains unclear what that alternate autocorrelation function might be, however, and so its discussion will be forestalled in favor of acknowledging additional uncertainty on the assumptions underpinning the previous low-temperature analysis.

Chapter 6

Conclusions and Future Directions

6.0.7 Conclusions

The notion that science is a process of precedent-driven curiosity is almost indisputable, and thin that sense this work bears little difference from any other scientific work. In terms of this study, the most obvious precedent lay in the senior thesis research of an undergraduate student, Hideo Mabuchi [33], at Princeton University in 1992. Mabuchi's work was one of the few investigations to that date into a microscopic mechanism responsible for the relaxation of a noble gas. Despite the limited number of observations in his work, it gave a strong indication of the utility of magnetic field and temperature variation towards the clarification of ^{129}Xe wall relaxation.By incorporating experimental methods employed by Mabuchi and other authors, our work expended the envelope (to borrow a phrase from the aerospace community) of xenon surface-relaxation measurements to a substantial degree. It is felt that the data within this envelope are sufficient to make several conclusions regarding the nature of the surface relaxation mechanisms, and those conclusions are threefold:

The first is that nuclear spin relaxation of ^{129}Xe on rubidium, rubidium hydride and rubidium deuteride surfaces is due to randomly fluctuating magnetic fields that are characterized by one or more correlation times. This conclusion is well supported by the universal observation in our samples of magnetic decoupling of the xenon relaxation rate.

The second conclusion to be drawn is that at high temperatures (temperatures above roughly 250 K), relaxation of xenon is chiefly due to interaction with paramagnetic sites. This conclusion is supported by the similarity of RbH and RbD cell

decoupling characteristics. It is also supported by the factor of approximately 3/10 observed in the ratio of Γ_B to $\Gamma_0 + \Gamma_B$ measured in all cells at high temperatures. Further support for the paramagnetic interpretation at high temperatures is found by the magnitude of relaxation in deuterium cells vs. that in hydrogen cells. If relaxation were due to surface protons, eqn. 5.2 implies that the deuterium cell relaxation rate should then be roughly 16 times smaller than the hydrogen cell relaxation rate. To the contrary, measurements show that it is roughly 4 times larger. This discrepancy suggests that high temperature relaxation is not nuclear in nature, consistent with the postulation of high-temperature paramagnetic relaxation. The high temperature paramagnetic interpretation is also supported by the quality of the decoupling curve fits under the two hypotheses, although we note that studies at higher field would be necessary for the fits by themselves to be more conclusive. Finally, we note that interpreting our decoupling data under the assumption of relaxation due to paramagnetic sites results in correlation times of 10-100 ps, quite reasonable if not a bit on the long side. In contrast, interpreting the data under the assumption of relaxation due to nuclear interaction results in correlation time values of 10-100 ns.

The third conclusion is that in the temperature range below 250 K, it is highly probable that the increase in relaxation rate with decreasing temperature in RbH cells is due largely to interaction between xenon and hydrogen. This conclusion is supported by presence of a sharp relaxation rate increase for cells X12 and X16 as temperature is decreased below $\approx$ 220 K, because the presence of that increase correlates with the presence of hydrogen in those cells. Additionally, the higher

quality of the decoupling curve fits under the nuclear interpretation for X12 data at low temperature would suggest that nuclear interactions better model the data. It is conversely supported by the absence of the large low temperature rate increase in cells containing deuterium, a less highly-relaxing nuclear species. With the ratio of Γ_B to $\Gamma_0 + \Gamma_B$ approximately equal to 3/10 in cells D1 and D3 at temperatures below 250 K, the notion that relaxation in deuterium-filled cells is dominantly paramagnetic in nature would seem well supported throughout the entire temperature range.

6.1 Future Directions and Applications

Returning to the more esoteric discussion of scientific inquiry begun above, an additional aspect of science that is encountered often enough to be considered almost intrinsic is its tendency to provide the basis for solutions to practical problems, both inside and outside the field. While the question of "who cares?" and its derivatives are sometimes considered banal, their answers, if available, very nearly provide the definition of scientific relevance. In the case of the work on display here, the value added to the scientific community and society in general is abundant.

The microscopic mechanism responsible for surface relaxation has been determined in precious few cases, and this work has added to that count. The techniques discussed here provide a probe with which to characterize the field and temperature dependencies of surface relaxation for myriad pairings of polarized gas and surface type. Further development, increasing the race of accessible magnetic fields and

temperatures, could only be beneficial. It could be compelling to use this probe to investigate the effect of various additives on cell performance, in hopes of discovering compounds that could "passivate" the wall surface with regard to wall relaxation. A. T. Nicol's work [31] demonstrated one method of surface passivation through substitution of hydrogen by deuterium in rubidium hydride surfaces. It would be interesting to see if other compounds - perhaps a halogen such as flourine (instilled in the form of solid XeF_6) - could be employed to further suppress or even deactivate relaxation at the cell wall.

The polarization performance of ^{3}He samples has benefited from research into "hybrid" SEOP, wherein an additional alkali metal (such as cesium or potassium) is present in the SEOP process and serves as a spin-exchange intermediary between helium and optically pumped rubidium [25, 69]. Spin-exchange between xenon and cesium has been demonstrated (and intriguingly, like binary exchange with rubidium, has been calculated to decouple at high magnetic fields [70, 71]). But while hybrid SEOP has been speculated to provide smaller relative gains for ^{129}Xe polarization than for ^{3}He polarization [72], the presence of an additional alkali metal in hybrid pumping suggests the possibility that wall-relaxation characteristics in hybrid SEOP ^{129}Xe cells might be quantitatively different. It would be very instructive to observe the differences between the magnetic field and temperature dependencies in such a cell as compared to a standard SEOP ^{129}Xe cell, and doubly interesting to observe the differences between a non-hydrided hybrid cell and a hybrid one. Such an investigation would require only the fabrication of new xenon samples, as the laser and polarimetry

equipment used for both standard and hybrid xenon cells are identical. This work has demonstrated that, in conjunction with characterizing and understanding relaxation processes, it is also possible to influence and control those processes to a substantial degree. From an applications standpoint, this second aspect is of great importance: the knowledge of how to substantially and repeatably inhibit surface relaxation of polarized ^{129}Xe can be put to use in the next generation of xenon polarizer. Practically speaking, this could make medical and scientific investigations involving polarized gas less expensive, which would be of clear benefit to patients, doctors, scientists, and insurance companies alike.

6.2 Final Thoughts

The field of polarized noble gas research is one of fervent activity and correspondingly great promise. Its scientific and practical relevance suggest that well into the future, myriad researchers will continue to find themselves occupied with one interesting question or another regarding the behavior or employ of polarized noble gases. Consequently, it is gratifying to know that this work has added, albeit in a modest fashion, to our understanding of noble gas relaxation. Much as the work of Mabuchi [33], Happer [5], Driehuys [34], Bloembergen [39] and many others influenced the direction and execution of this experimental work, it is similarly hoped that one day in the future another graduate student will find the work presented here to be of some inspiration, or that it at least provide them with some useful advice.

Appendices

Appendix A

The ^{129}Xe-Proton Cross Relaxation Experiment

As discussed in chapter 5, we saw strong evidence that at temperature below 250 K, the spin relaxation of ^{129}Xe in cells containing hydrogen was dominated by dipolar coupling between the ^{129}Xe nuclei and surface protons. If we further assume that the longitudinal spin relaxation times of the surface protons is comparable to or longer than the spin relaxation times of the ^{129}Xe nuclei, we would expect a significant non-thermal polarization of the surface protons to develop. The spin relaxation times of protons in RbH crystals in sample cells not very different than ours have been measured to be 4200 s at room temperature in a 1.4 T field. With such a long T_1 for the protons, there was the very real possibility that, under the right conditions, a cross relaxation signal from protons could be detected.

Such a possibility is by no means farfetched - Karen Sauer [36] and Bastiaan Driehuys [34] demonstrated xenon-proton spin exchange in one investigation of a xenon surface relaxation mechanism. In his doctoral dissertation, Driehuys conclusively observed the exchange of angular momentum from polarized ^{129}Xe to surface protons contained in silicone-based SurfaSil^{TM} coatings through the use of a novel double resonance scheme. Gatzke et al. [73] exhibited evidence of cross-relaxation between ^{129}Xe and ^{131}Xe, demonstrating the possibility of spin transfer between species of similar gyromagnetic ratio. Gatzke's study took place at extremely low temperature (4.3 K) and fields below 100 G, however, in contrast to the conditions of these experiments.

In experiments here, the attempt to detect a proton signal was made by employing the spectrometer that was discussed in Chapter 4, taking advantage of its ready

applicability to any resonance that fell within its operational frequencies. If polarization were to be exchanged between two species whose frequencies at a given field fell within the operational range of the spectrometer, that exchange could, in principle, be confirmed by the observation of a greater-than-thermal polarization signal in the non-optically pumped species.

A.1 Xe-Proton Polarization Transfer

Relaxation of xenon through dipolar interactions with surface protons is qualitatively similar to relaxation of xenon through dipolar interaction with surface electrons. Consequently, the analysis framework for the paramagnetic relaxation of xenon can be applied to xenon-proton cross-relaxation. Assuming a collection of xenon atoms and surface protons interacting through mutual dipolar relaxation characterized by spin-lattice relaxation rates ($\frac{1}{T_1^{Xe-Xe}}$ and $\frac{1}{T_1^{P-P}}$) and the cross-relaxation rate ($\frac{1}{T_1^{Xe-P}}$), cross-relaxation rates can be written as

$$\frac{dP_{Xe}}{dt} = -\frac{1}{T_1^{Xe-Xe}}(P_{Xe} - P_{Xe0}) - \frac{1}{T_1^{Xe-P}}(P_P - P_{P0}), \tag{A.1}$$

and

$$\frac{dP_P}{dt} = -\frac{1}{T_1^{P-P}}(P_P - P_{P0}) - \frac{1}{T_1^{Xe-P}}(P_{Xe} - P_{Xe0}). \tag{A.2}$$

Here, $\frac{1}{T_1^{Xe-Xe}}$, $\frac{1}{T_1^{Xe-P}}$ and $\frac{1}{T_1^{P-P}}$ correspond to xenon-xenon, xenon-proton, and proton-proton exchange rates respectively and are a function of magnetic field and temper-

ature. A limiting condition for the observation of ^{129}Xe-Proton spin transfer is the relaxation rate of the protons involved: in Surfasil coatings, the lattice relaxation rate of protons was found to be approximately 2 s at 9.4 T [34]. For protons bound in RbH coatings, however, the lattice relaxation rate is documented by Brian Saam to be on the order of 2.4×10^{-4} Hz (T_1 = 70 min.) [57]. With such a long relaxation time, it would seem likely that measurable polarization could accumulate in surface protons because of cross-relaxation interactions, and be retained for a long enough time scale to permit its measurement.

A.2 ^{129}Xe-Proton Cross-Relaxation Experiment

In order to further confirm the source of the additional relaxation as nuclear in nature, we undertook efforts to observe the presence of above-thermal polarization in surface protons. A detectable above-thermal proton signal would indicate polarization exchange with polarized ^{129}Xe. The exchange of polarization to the involved protons could, in principle, be observed by simply acquiring a NMR signal keyed to the proton Larmor frequency when experimental conditions favored relaxation via that mechanism. Pursuant to that goal, NMR signals keyed to a proton resonance were acquired from an RbH cell at a field and temperature combination that was observed to exhibit suspected nuclear relaxation.

In initial attempts using cell X12, no signal was seen, although this is not too surprising.The cell X12 possessed relatively few hydrogen atoms (approximately 10^{18}),

and a low proton polarization upper limit of $\approx 0.1\%$ (this was equal to the ^{129}Xe polarization).

In an attempt to resolve these limitations, a new set of samples was fabricated using enriched ^{129}Xe. Cells were also constructed with 2 cm diameters, in hopes that the smaller diameter would encompass smaller absolute field inhomogeneities, and would consequently result in greater sensitivity to nuclear signals through longer T_2 values. Xenon pressures were approximately 7 atm, and hydrogen charges were instilled in the cells at various pressures, at 0 Torr (control), 20 Torr, 40 Torr, and 80 Torr for cells X13-X16, respectively. The filling process was the same as that described in Chapter 4 for cells X9-X12 and D1-D5.

A.2.1 Line Narrowed Laser Pumping

In an attempt to resolve the limitation of low xenon polarization, a line-narrowed laser source was constructed in place of the FAP system previously employed for optical pumping. With a linewidth of approximately 0.3 nm, it was possible to couple the bulk of the line-narrowed laser power into the polarization process. In contrast, the FAP system wasted most of its power through output in wavelengths which lay outside of the usable absorption spectrum of the rubidium, given the SEOP oven temperature and the physical dimensions of the cell.

Following the pioneering work of Zerger, Chupp et al. [74], Nelson et al. [75], and more recently James Wang [24], a laser diode array was arranged to send its output through a beam expanding telescope that imaged the diode array onto a holographic

reflection grating. By placing the beam at sufficiently high angle of incidence to the grating, it was possible to send the first order diffraction maximum back along the path of the incident beam, forming the feedback signal necessary for narrowing the spectrum of the diode. The rough arrangement of the setup is shown in figure A.1, and the relation between diffraction order, diffraction angle and wavelength is given by

$$n\lambda = \mathrm{d}\left(\sin(\theta) \pm \sin(\theta')\right), \tag{A.3}$$

where n is the diffraction order, λ is the wavelength of the incident light, d is the distance between lines on the diffraction grating, and θ and θ' are the angles of incidence of the incoming and outgoing light, respectively. The use of cylindrical lenses to appropriately image the rectangular beam emitter onto the spherical cell, and usein ghe first order diffraction maximum for optical feedback very closely follows the arrangement used by Nelson et al.

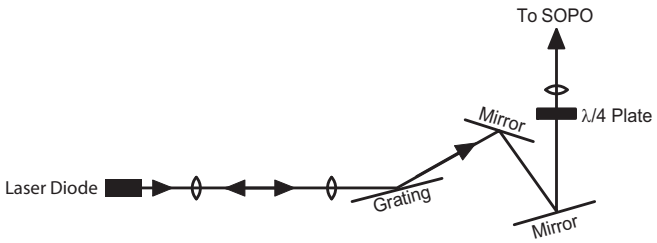

Figure A.1: Line Narrowed Optics Arrangement

Following the prescription set out in the various listed resources and in Wang's work, a 30 W laser diode array was assembled such that its output was directed into a holographic reflection grating etched with 2400 lines/mm, with the first order

maximum corresponding the the desired wavelength (794.7 nm, as is appropriate for Rb D1 resonance optical pumping) directed coincident and antiparallel back into the laser diode. The output of the arrangement is taken from the 0th order maximum.

A high power Laser Diode Array (LDA) typically exhibits beam divergence of roughly 40° in the dimension perpendicular to the array (fast axis), and a divergence of roughly 10° in the dimension parallel to the array (slow axis). In order to use the laser for pumping, it was necessary to collimate the beam. In this pursuit, a cylindrical microlens was installed by the manufacturer at the LDA output, parallel to the slow axis, bringing the fast axis divergence angle to within 1°-2° of being collimated. Following the microlens, a telescope imaged the beam onto the grating with magnification M. The grating, arranged with grooves parallel to the diode slow axis, provided optical feedback to the LDA elements.

The emission spectrum of the diode laser array with and without narrowing is shown in Fig. A.2. As is clearly demonstrated, the amount of usable power at the rubidium absorption wavelength was vastly increased for equivalent overall laser power when employing line narrowing. Crucial to this enhancement was the proper placement of the output wavelength, but as eqn. A.3 demonstrates, wavelength was easily tunable by variation of the orientation of the diffraction grating. Output wavelength was selected for 794.7 nm, and the beam was carried and conditioned by a series of mirrors and cylindrical lenses so as to be delivered in parallel to the pre-existing optical line.

The optimized pumping oven temperature of 90° C was considerably lower than

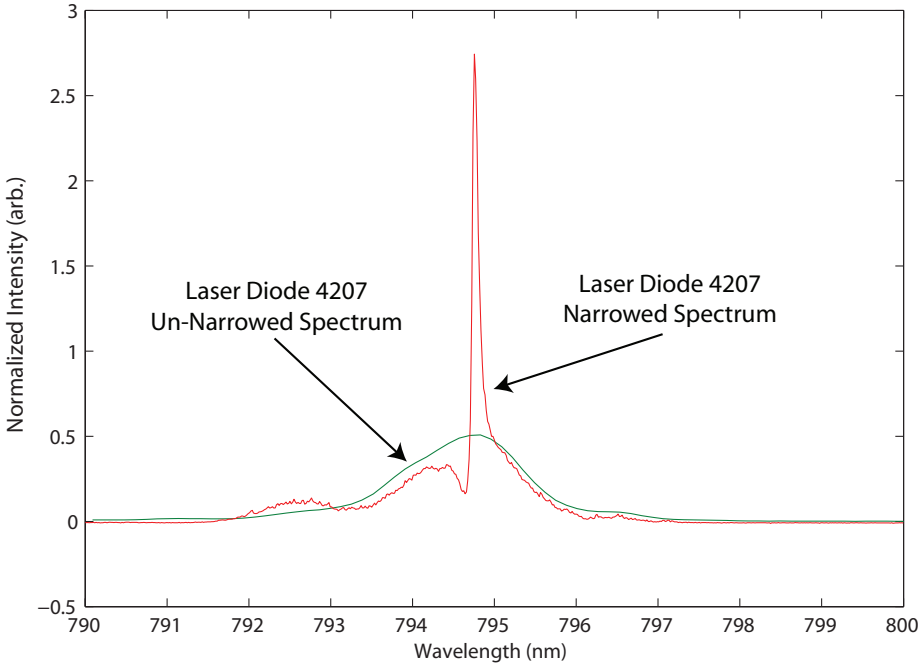

Figure A.2: A comparison of the narrowed & un-narrowed laser diode array emission spectra. The spectra were acquired with a Jobin-Yvon monochromater, and are displayed normalized for total intensity. This figure demonstrates the greatly increased amount of power available in the narrow range around the emission peak for the narrowed laser relative to the un-narrowed laser.

that using the FAP lines exclusively, roughly 105° C. It was suspected that this was largely due to the fact that increased light absorption resulted in greater power delivery to the cell - consequently, for the same oven temperature, the actual cell temperature was suspected to be far higher than when using the FAP system. This effect was also reflected in the fact that use of two line-narrowed beams forced a temperature optimum point at an even lower temperature than using a single line-narrowed line. (Quite dramatically, enriched cells could be observably polarized at oven temperatures as low as 30° C.)

A.3 ^{129}Xe-Proton Spin Transfer Tests with High Xenon Pressure Cells X14 Through X16

Following destructive testing of X14 and X16[1], pumping parameters (such as the temperature and central wavelength of the laser) were determined to enable non-destructive pumping of cell X15 to a xenon polarization of 0.14%. Equations A.1 and A.2 imply a proportionality between the initial polarization of the xenon ensemble and the peak polarization of the proton ensemble, such that

$$P_P = C_{Xe-P} * P_{Xe} \tag{A.4}$$

where P_P is the proton polarization, P_{Xe} is the xenon polarization, and C_{Xe-P} is the constant of proportionality between the two polarizations:

$$C_{Xe-P} \approx \frac{\Gamma_{Xe-P}}{\Gamma_{Xe-P} + \Gamma_{P-Loss}}. \tag{A.5}$$

Here, Γ_{Xe-P} is the xenon-proton cross-relaxation rate, and Γ_{P-Loss} is taken to be equal to the proton lattice relaxation rate.

The xenon-proton exchange rate was assumed to be the difference between the observed relaxation rate in the proposed nuclear interaction regime and the assumed

[1]Cells X14 and X16 were destroyed through testing the line-narrowed polarization process - the high power absorbed through the use of the line narrowed laser resulted prompted un-characterized chemical reactions that spoiled the interior of the cell, displaying a marked contrast between the behavior of the FAP system and the line-narrowed system.

baseline paramagnetic rate, and was on the order of 10 mHz. The proton lattice relaxation lifetime was documented by Saam [57] to be approximately 4200 s at a field of 1.4 T. Consequently, it was expected that C_{Xe-P} would be ≈ 1 in the range of $210K \rightarrow 200K$.

In the 2 cm water cell, the proton signal-to-noise ratio (SNR) was measured to be roughly 100 to 1. Assuming that all the hydrogen nuclei were cross-polarized to a value roughly equal to that of the xenon polarization (recalling that the ratio of these polarizations is given by C_{Xe-P}), it was expected that a proton polarization of .14%, roughly 7000 times the thermal polarization, would still be observable with a SNR of roughly 5. In view of this expectation, it was all the more unexpected that no proton signal was observed in X15 following xenon polarization. Investigation of this discrepancy forced the reconsideration of some of the assumptions underlying the expectation of an observable proton signal.

With a RbH radius of ~ 3Å, approximately 10^{16} RbH sites could be distributed across the inside surface of the 1 cm radius cell in a single layer. The inside surface of the cell is certainly not perfectly smooth, and so it is assumed that there are closer to 10^{17} sites per layer. The charge of $\approx 10^{18}$ hydrogen atoms would suggest around 10 rubidium hydride layers, given the complete involvement of the hydrogen charge in RbH formation. Considering spin-diffusion, it can also be assumed that up to ten surface layers are involved in surface cross-relaxation, meaning a roughly complete involvement of the instilled hydrogen atoms in cross-relaxation. The assumption of complete involvement could be invalidated if the number of sites per layer were

smaller, as well as if the spin-diffusion depth were smaller than ten layers.

Given the sub-millihertz spin-lattice relaxation rate of surface hydrogen atoms documented by Saam, it seems all the more curious that a substantial hydrogen-associated relaxation rate was observed in cells X12 and X16. If the ^{129}Xe-hydrogen cross-relaxation rate were indeed much larger than the hydrogen spin-lattice relaxation rate, polarization could be expected to be transferred from surface hydrogens back to xenon atoms faster than it leaked out through cell walls via spin-lattice relaxation. The fact that a large relaxation rate value is so strongly correlated with xenon-hydrogen cross-relaxation suggests that either spin-lattice relaxation is much higher in our cells or that a hydrogen-associated mechanism other than spin-lattice relaxation is present. Saam's measurement of a 70 minute spin-lattice relaxation lifetime was made at higher fields and temperatures than the measurements of the suspected xenon-hydrogen cross-relaxation presented here, and it is certainly plausible that at reduced field and temperature, the spin-lattice rate is higher. It is also possible that some hydrogen atoms remained in the gas form in our cells, opening the possibility of cross-relaxation between surface and gaseous hydrogen atoms. The spin-rotation interaction is a more likely relaxation mechanism for gaseous hydrogen molecules than it is for surface hydrogen atoms, presenting an additional polarization loss route that might not have been present in Saam's cells. The overarching point motivated by these discrepancies is that C_{Xe-P} could, in fact, be much smaller than 1 due to an unexpectedly high value of Γ_{P-Loss}.

A.4 ^{129}Xe-Proton Spin Transfer Tests with Low Xenon Pressure Cells X17 Through X20

Equipped with a suspicion of why successful proton signal acquisition was unlikely in cells X13 through X16, a fourth set of cells[2] was constructed with an eye to greatly increasing the xenon polarization in order to compensate for a possibly smaller value of C_{Xe-P} and a smaller quantity of hydrogen. In cells X17 through X20, the expected xenon polarization was increased by filling the cells with a reduced quantity of xenon. The expectation of increased polarization can be understood through analysis of the equilibrium polarization equation:

$$P_{Xe} = P_{Rb}\frac{\Gamma_{SE}}{\Gamma_{SE} + \Gamma_{SR_{Xe}}}, \tag{A.6}$$

where Γ_{SE} is the Rb-^{129}Xe spin-exchange rate, $\Gamma_{SD_{Xe}}$ is the ^{129}Xe relaxation rate, and P_{Rb} is the rubidium polarization. The rubidium equilibrium polarization is given by

$$P_{Rb} = \frac{\Gamma_{op}}{\Gamma_{op} + \Gamma_{SD_{Rb}}}. \tag{A.7}$$

The spin-destruction rate, $\Gamma_{SD_{Rb}}$, is assumed to be proportional to the xenon number density:

$$\Gamma_{SD_{Rb}} = \phi[Xe] \tag{A.8}$$

[2]The X17-X20 series was created fourth in sequence after the X9-X12 series, D1-D5 series, and X13-X16 series.

and is also assumed to be much larger than the optical pumping rate, γ_{op}, resulting in

$$P_{Rb} \approx \frac{\Gamma_{op}}{\phi[Xe]}, \tag{A.9}$$

where ϕ represents constants of proportionality. Combining eqn.s A.6 through A.9, we find

$$P_{Xe} = P_{Rb}\frac{\Gamma_{SE}}{\Gamma_{SE}+\Gamma_{SR_{Xe}}} \approx \frac{\Gamma_{OP}}{\phi[Xe]}\frac{\Gamma_{SE}}{\Gamma_{SE}+\Gamma_{SD_{Xe}}}. \tag{A.10}$$

Below saturation, xenon polarization can be expected to increase with decreasing xenon number density, resulting in a roughly constant induced xenon signal. Through its interaction with C_{Xe-H}, however, the higher xenon polarization resulting from lower xenon density can be expected to proportionally increase the hydrogen polarization.

$$P_H = C_{Xe-H}P_{Xe} \propto \frac{C_{Xe-H}}{[Xe]} \tag{A.11}$$

In accordance with the implication of eqn. A.11 for hydrogen polarization, cells X17 through X20 were filled with the following pressures:

Table A.1: X17-X20 Cell Contents

Cell	^{129}Xe Pressure	N_2 Presure	^{4}He Pressure	H_2 Pressure
X17	64 Torr (enr.)	199 Torr	2.78 atm	15 Torr
X18	63 Torr (enr.)	201 Torr	2.78 atm	25 Torr
X19	71 Torr (enr.)	200 Torr	2.79 atm	25 Torr
X20	71 Torr (enr.)	199 Torr	2.79 atm	40 Torr

Polarization performance of cells X17 through X20 turned out to be less impressive than expected: the maximum polarization achieved, observed at a temperature point

just below that where the cell interior spoiled (90° C), was at the percent level, in comparison to the roughly ten percent level expected. Actual cell polarization values for cells X17 through X20 are given in table A.2:

Table A.2: X17-X20 observed xenon polarizations

Cell	Polarization
X17	1.1%
X18	1.2%
X19	2.8%
X20	1.7%

While these polarization values were approximately an order of magnitude lower than expected, they are not grossly inconsistent with predictions; a ten-fold increase in polarization with a hundred-fold decrease in xenon number density is possible if the sum of rubidium optical pumping and non xenon-related rubidium spin-destruction rates are only an order of magnitude greater than the low xenon pressure spin-destruction rate. Furthermore, relaxation rates for these cells were greatly in excess of the rates measured for cells X9-X16:

Table A.3: X17-X20 T_1 Values, $B = 823.5G$, $T \approx 290K$

Cell	T_1
X17	70 s
X18	50 s
X19	120 s
X20	220 s

In light of the values listed in table A.3, the values in table A.2 are entirely reasonable. While this evidence is encouraging in its explanatory value, it does nothing to

alter the value of the xenon polarizations observed, which in turn provide an upper limit to the polarization available to be transferred to surface protons. Nevertheless, this upper polarization limit enables an estimate on the amplitude of the proton signal.

Applying the 2.5% polarization value to the aforementioned $\approx 1.6 * 10^{17}$ involved surface protons:

$$Signal_{surface} = P * N_{surface} = C_{Xe-H} * 0.025 * 1.6 \times 10^{17} = 4 * 10^{15} \tag{A.12}$$

$$Signal_{water} = P * N_{water} = 2.875 \times 10^{-7} * 1.877 \times 10^{23} = 5.4 * 10^{16}. \tag{A.13}$$

With typical water sample SNRs of approximately 100, C_{Xe-H} exchange constants greater than roughly 0.14 could be expected to result in observable proton signals, while again operating under the assumption of 10^{17} interacting hydrogen centers.

Attempts to acquire a proton signal from cells X17 through X20 followed the earlier-established procedure, polarizing cells via line-narrowed SEOP at 90^o C and rapidly chilling cells to 203K, with a delay between chill and NMR signal acquisition so as to enable spin transfer. No proton NMR signal was observed in any sample. As before, absence of a proton signal can be explained by three alternative conditions: high proton spin-destruction rate; low xenon-proton spin-exchange rate; breakdown of the assumptions regarding surface RbH number and/or C_{Xe-P} value. The first scenario is excluded by the 42 minute proton lattice T_1 determined by Saam [57]; the second is suggested as unlikely due to the observation of the 0.011 mHz xenon

relaxation rate at low temperature and frequency; the third option is compelling, owing to the tenuous nature of the assumptions involving surface proton number and exchange coefficient.

Bibliography

[1] W. G. Proctor, F. C. Yu, Phys. Rev. 78, 471 - 471 (1950)

[2] R. L. Streever, H. Y. Carr, Phys. Rev. 121, 20 (1961)

[3] E. R. Hunt, H. Y. Carr, Phys. Rev. 130, 2302 (1963)

[4] P. Bachert, L. R. Schad, M. Bock, M. V. Knopp, M. Ebert, T. GroDmann, W. Heil, D. Hofmann, R. Surkau, E. W. Otten, Mag. Res. Med., 36, 2, 192-196 (1996)

[5] W. Happer, Rev. Mod. Phys., 44, 169 (1972)

[6] T. G. Walker, W. Happer, Rev. Mod. Phys., 69, 2 (1997)

[7] "In vivo He-3 MR images of Guinea Pig Lungs," R. D. Black, H. L. Middleton, G. D. Cates, G. P. Cofer, B. Driehuys,W. Happer, L. W. Hedlund, G. A. Johnson, M. D. Shattuck, J. C. Swartz; Radiology 199, 867 (1996).

[8] M. V. Romalis, Doctoral Dissertation, "Laser Polarized ^{3}He Target Used for a Precision Measurement of the Neutron Spin Structure.", Princeton University (1996)

[9] H. Middleton, R. D. Black, B. Saam, G. D. Cates, G. P. Cofer, R. Guenther, W. Happer, L. W. Hedlund, G. A. Johnson, K. Juvan, J. Swartz, "MR Imaging With Hyperpolarized ^{3}He gas," Magnetic Resonance in Medicine 33, 271 (1995)

[10] A. Bifone, Y. Q. Song, R. Seydoux, R. E. Taylor, B. M. Goodson, T. Pietrass, T. F. Budinger, G. Navon, A. Pines, Proc. Natl. Acad. Sci. USA, Vol. 93, 12932-12936, (1996)

[11] M. S. Albert, D. F. Kacher, D. Balamore, A. Venkatesh, F. A. Jolesz. "T1 of 129Xe in Blood and the Role of Oxygenation" J. Mag. Res., 140, 264-273 (1999)

[12] A.K. Venkatesh, K.S. Hong, L. Kubatina, Y. Sun, R. Mulkern, F.A. Jolesz, and M.S. Albert, *Using dynamic hyperpolarized xenon MR to measure brain perfusion.* Proceedings of the Ninth Annual Meeting of the International Society of Magnetic Resonance in Medicine, 2001: p. 951.

[13] J. Wolber, D. J.O. McIntyre, L. M. Rodrigues, P. Carnochan, J. R. Griffiths, M. O. Leach, and A. Bifone, Mag. Res. in Med. 46:586591 (2001)

[14] Improved NMR Based Bio-Sensing with Optimized Delivery of Polarized 129Xe to Solutions, S. Han, S. Garcia, T. J. Lowery, E. J. Ruiz, J.A. Seeley, L. Chavez, D. S. King, D. E. Wemmer, A. Pines Anal. Chem. 77 (2005)

[15] F. J. Adrian, Chem. Phys. Lett., 7, 201-204 (1970)

[16] A. Bifone, Phys. Rev. Lett. 74, 3277 (1995)

[17] S. Han, H. Kuhn, F. W. Hasing, K. Munnemann, B. Blumich and S. Appelt, Time resolved spectroscopic NMR imaging using hyperpolarized 129Xe, Journal of Magnetic Resonance, Volume 167, Issue 2, P. 298-305 (2004)

[18] C. Kittel, H. Kroemer, *Thermal Physics* 2nd ed., W. H. Freeman & Co., New York, NY (1980)

[19] "Biological Magnetic Resonance Imaging Using Laser-Polarized ^{129}Xe," Albert, M S; Cates, G D; Driehuys, B; Happer, W; Saam, B; Springer, C S , Jr; Wishnia, A; Nature 370, 199 (1994)

[20] J. P. Mugler et al, Mag. Res. Med., 37, 6, 809-815 (1997)

[21] K. Ruppert, J. F. Mata, J. R. Brookeman, K. D. Hagspiel, J. P. Mugler III, Mag. Res. Med., 51, 4, 676 (2004)

[22] "The Estimation of Helium-3 Probable Reserves in Lunar Regolith" E. N. Slyuta and A. M. Abdrakhimov, and E. M. Galimov, Lunar and Planetary Science XXXVIII (2007)

[23] R. C. Weast, M. J. Astle, W. H. Beyer, CRC Handbook of Chemistry and Physics, 69th ed. CRC Press, Inc., Boca Raton, FL (1989)

[24] James Wang, Doctoral Dissertation, "New Xenon Gas Polarizer with application to Magnetic Resonance Imaging"" (2006)

[25] E. Babcock, I. Nelson, S. Kadlecek, B. Driehuys, L. W. Anderson, F. W. Hersman, T. G. Walker, Phys. Rev. Lett. 91, 123003 (2003)

[26] G. D. Cates S. R. Schaefer, W. Happer, Phys. Rev A 37 p.2877, (1988)

[27] G. D. Cates, D. J. White, Ting-Ray Chien, S. R. Schaefer, W. Happer, Phys. Rev. A 38, 5092 (1988)

[28] N. R. Newbury, A. S. Barton, G. D. Cates, W. Happer, and H. Middleton, Phys. Rev. A 48, 6, 4411-4420 (1993)

[29] B. Chann, I. A. Nelson, L. W. Anderson, B. Driehuys, and T. G. Walker, Phys. Rev. Lett. 88, 113201 (2002)

[30] B. Driehuys, G. D. Cates, W. Happer, Phys. Rev. Lett. 74, 4943 (1995)

[31] A. T. Nicol, Phys. Rev. B 29, 2397 (1984)

[32] V. V. Yashchuk, J. Granwehr, D. F. Kimball, S. M. Rochester, A. H. Trabesinger, J. T. Urban, D. Budker, and A. Pines, Phys. Rev. Lett. 93, 160801 (2004)

[33] H. Mabuchi, Senior Thesis, "Wall-Relaxation Mechanisms for Polarized Noble Gases," Princeton University, 1992

[34] B. Driehuys, Doctoral Dissertation, "Surface Physics And New Applications Using Laser-Polarized ^{129}Xe", Princeton University (1995)

[35] C. P. Slichter, "Principles of Magnetic Resonance" 3 ed., Springer Publishing (1996)

[36] K Sauer, Doctoral Dissertation, "Laser Polarized Liquid Xenon," Princeton University (1995)

[37] A. Abragam, "Principles of Magnetic Resonance", Oxford University Press (1961)

[38] U. Fano, Rev. Mod. Phys. 29, 1 (1957)

[39] N. Bloemburgen, E. M. Purcell, R. V. Pound, Phys. Rev. 73, 679 (1948)

[40] L. D. Schearer, G. K. Walters, Phys. Rev. A 139, A1398 (1965)

[41] R. L. Gamblin, T. R. Carver, Phys. Rev. A 138, 946 (1965)

[42] R. Shankar, Principles of Quantum Mechanics, 2nd ed., Plenum Press, New York (1994)

[43] I. Solomon, Phys. Rev. 99, 559 (1955).

[44] W. Franzen and A. G. Emslie, Phys. Rev. 108, 1453(1957)

[45] M. A. Bouchiat, T. R. Carver and C. M. Barnum, Phys. Rev. Lett. 5, 8, 373 (1960)

[46] Jaideep Singh and Al Tobias, Private Communication (2006)

[47] B. C. Grover, Phys. Rev. Lett. 40, 391 (1978)

[48] C. H. Volk, T. M. Kwon, and J. G. Mark, Phys. Rev. A 21, 1549 (1980)

[49] M. V. Romalis, E. Miron, G. D. Cates, Phys. Rev. A 56, 4569 - 4578 (1997)

[50] B. Driehuys, G. D. Cates, E. Miron, K. Sauer, D. K. Walter, and W. Happer, Appl. Phys. Lett. 69, 12 (1996)

[51] G. D. Cates, R. J. Fitzgerald, A. S. Barton, P. Bogorad, M.Gatzke, N. R. Newbury, and B. Saam, Phys. Rev. A 45, 4631 (1992)

[52] Y. Jau, N. Kuzma, W. Happer, Phys. Rev. A 69, 061401 (2004)

[53] E. Babcock, B. Chann, T. G. Walker, W. C. Chen, T. R. Gentile, Phys. Rev. Lett. 96, 083003 (2006)

[54] Jaime Mata, Private Communication, 2007

[55] E. Hecht, Optics 3 ed., Addison Wesley Longman, Inc. (1998)

[56] J. Singh, "Using Gaussian Optics to Manipulate Laser Beam Spot Size", unpublished notes

[57] Brian Saam, Doctoral Dissertation, "Pulse-NMR Studies Of Spin Relaxation Relevant To Laser-Polarized Noble Gases," Princeton University (1995)

[58] F. Bloch, Phys. Rev 105 p.1206 (1957)

[59] F. E. Terman, Radio Engineer's Handbook, McGraw-Hill Book Company, inc. (1943)

[60] E. Fukushima, Pulse NMR: A Nuts and Bolts Approach, Addison-Wesley Pub. Co. (1957)

[61] Paul T. Callaghan, Principles of Nuclear Magnetic Resonance Microscopy, Oxford University Press, Oxford, U.K. (1993)

[62] "On the error analysis of FID's" G. D. Cates, Unpublished Notes (2004)

[63] J. Schmiedeskamp, W. Heil, E. W. Otten, R. K. Kremer, A. Simon, J. Zimmer, Eur. Phys. Jour. D 38, 427 (2006)

[64] M. K. J. D. Z. Wu, W. Happer, Phys. Rev. A 42, 2774 (1990)

[65] A. Deninger, W. Heil, E. W. Otten, M. Wolf, R. K. Kremer, A. Simon, Eur. Phys. Jour. D 38,439 (2006)

[66] V. I. Feldman, F. F. Sukhov, Chem. Phys. Lett. 255, 425 (1996)

[67] N. Runeberg, M. Seth, P. Pyykk, Chem. Phys. Lett. 246, 239 (1995)

[68] R. C. Ball, P. T. Callaghan, E. T. Samulski, J. Chem. Phys., 106, 17 (1997)

[69] W. C. Chen, T. R. Gentile, T. G. Walker, E. Babcock, Phys. Rev. A 75, 013416 (2007)

[70] Y. Jau, N. Kuzma, W. Happer, Phys. Rev. A 66, 052710 (2002)

[71] Y. Jau, N. Kuzma, W. Happer, Phys. Rev. A 67, 022720 (2003)

[72] Personal Communication, Jaideep Singh and Gordon Cates (2007)

[73] M. Gatzke, G. D. Cates, B. Driehuys, D. Fox, W. Happer, B. Saam, Phys. Rev. Lett. 70, 690 (1993)

[74] J. N. Serger, M. J. Lim, K. P. Coulter, T.E. Chupp, Appl. Phys. Lett. 76, 14, 1798-1800 (2000)

[75] I. A. Nelson, B. Chann and T. G. Walker, Appl. Phys. Lett. 76, 11, 1356-1358 (2000)